SEMI-ANNUAL REPORT

(for January – July 1995)

Contract Number NAS5-31363

OCEAN OBSERVATIONS WITH EOS/MODIS:

Algorithm Development and Post Launch Studies

Howard R. Gordon

University of Miami

Department of Physics

Coral Gables, FL 33124

(Submitted July 15, 1995)

Abstract

Several significant accomplishments were made during the present reporting period.

- An investigation of the influence of stratospheric aerosol on the performance of the atmospheric correction algorithm was carried out. The results indicate how the performance of the algorithm is degraded if the stratospheric aerosol is ignored. Use of the MODIS 1380 nm band to effect a correction for stratospheric aerosols was also studied. Simple algorithms such a subtracting the reflectance at 1380 nm from the visible and near infrared bands do not significantly reduce the error. The only way found to significantly reduce their effects requires full knowledge of the stratospheric aerosol optical properties, and extensive radiative transfer computations for implementation.

- The development of a multi-layer Monte Carlo radiative transfer code that includes polarization by molecular and aerosol scattering and wind-induced sea surface roughness has been completed. Comparison tests with an existing two-layer successive order of scattering code suggests that both codes are capable of producing top-of-atmosphere radiances with errors usually $< 0.1\%$. This code will be used to generate realistic pseudo data with which to test the atmospheric correction algorithm.

- An initial set of simulations to study the effects of ignoring the polarization of the ocean-atmosphere light field, in both the development of the atmospheric correction algorithm and the generation of the lookup tables used for operation of the algorithm, have been completed. The results suggest two important conclusions: (1) that most of the error due to the neglect of polarization can be removed by computing the Rayleigh contribution to the total reflectance using vector radiative transfer theory; and (2) the residual error in the water-leaving reflectance due to the neglect of polarization in constructing the lookup tables is usually ~ 0.001, and appears to vary in a systematic manner with viewing geometry.

- An algorithm was developed that can be used to invert the radiance exiting the top and bottom of the atmosphere to yield the columnar optical properties of the atmospheric aerosol under clear sky conditions over the oceans, for aerosol optical thicknesses as large as 2. The algorithm is capable of retrievals with such large optical thicknesses because all significant orders of multiple scattering are included. Combining an algorithm of this type with surface-based and high altitude aircraft-based radiance measurements could be useful for studying aerosol columnar optical properties over oceans and large lakes.

1. Atmospheric Correction Algorithm Development

a. Task Objectives:

During CY 1995 there are five objectives under this task:

(i) Investigate the effects of stratospheric aerosol and/or cirrus clouds on the performance of the proposed atmospheric correction algorithm.

(ii) Complete a multilayer Monte Carlo simulation code that includes the effects of aerosol and molecular scattering polarization (a vector radiative transfer code) and sea surface roughness.

(iii) Investigate the effects of ignoring the polarization of the atmospheric light field on the performance of the proposed atmospheric correction algorithm.

(iv) Investigate the effects of vertical structure in the aerosol concentration and type on the behavior of the proposed atmospheric correction algorithm.

(v) Begin a detailed investigation of the performance of the correction algorithm in atmospheres with strongly absorbing aerosols.

b. Work Accomplished:

(i) We have completed the computations regarding the influence of stratospheric aerosols on atmospheric correction, and the possibility of using the 1380 nm MODIS band for removing their effects. A report covering the present status of this work is attached as Appendix 1

(ii) We have completed development and validation of a multilayer Monte Carlo code radiative transfer code to provide test pseudo data for examination of the performance of the proposed atmospheric correction algorithm in more realistic situations. The code solves the vector radiative transfer equation (i.e., it includes the effects of polarization) for the Stokes vector of the radiance exiting the top of the atmosphere. It also includes a wind-roughened sea surface at the lower boundary of the atmosphere. The atmosphere is divided into four broad regions: (1) the marine

boundary layer from the surface to 2 km, where the aerosol concentration is independent of altitude; (2) the free troposphere, where the aerosol concentrations varies in proportion to $\exp[-z/h]$, where z is the altitude (2-12 km) and h (the scale height) is 2 km; (3) the background stratosphere (12-30 km), where the aerosol concentration is also exponential with a scale height of 5 km; and (4) a volcanic region (20-25 km) within the stratosphere which can contain a uniformly mixed volcanic aerosol. The optical properties of each of the four regions can be characterized by individual aerosol models, and any of the regions can be free of aerosols if desired. Alternatively, the user can supply any vertical structure desired for the aerosol; however, no more than four different aerosol models can be used in a single simulation.

The final code was validated by comparison with an existing two-layer code[1] which employs the successive order of scattering method.[2] The aerosol model used in the code validation was that originally used by Gordon and Wang[3] and is similar to that used by Quenzel and Kastner[4]to represent a marine aerosol at 70% relative humidity. The size distribution was

$$\begin{aligned} \frac{dN}{dD} &= K, & D_0 < D \le D_1, \\ &= K\left(\frac{D_1}{D}\right)^{\nu+1}, & D_1 < D \le D_2, \\ &= 0, & D > D_2, \end{aligned}$$

with $\nu = 2.95$, $D_0 = 0.2$ μm, $D_1 = 0.4$ μm, and $D_2 = 17.5$ μm, and the refractive index was $1.45 - 0.02i$. The resulting, nonzero, elements of the scattering phase matrix are provided in Figure

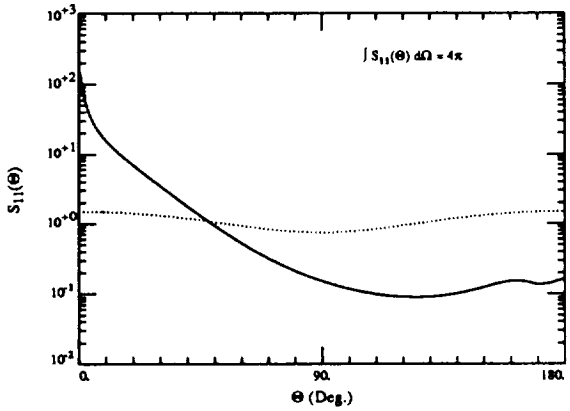

Figure 1a. S_{11} element of the scattering matrix for aerosols (solid line) and molecules (dotted line) as a function of the scattering angle. Note, $S_{22} = S_{11}$.

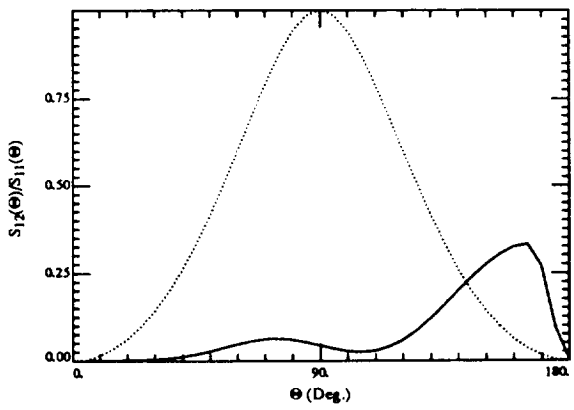

Figure 1b. S_{12} element of the scattering matrix for aerosols (solid line) and $-S_{12}$ for molecules (dotted line) as a function of the scattering angle. Note, $S_{21} = S_{12}$.

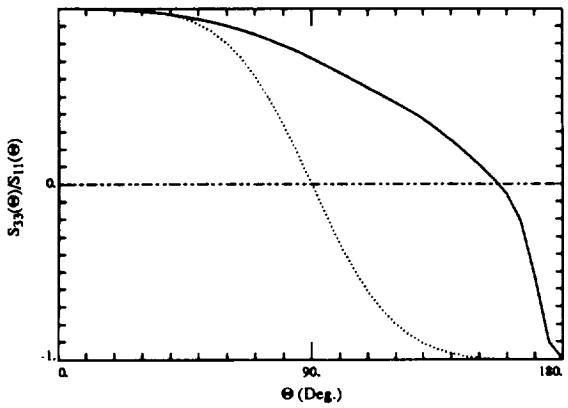

Figure 1c. S_{33} element of the scattering matrix for aerosols (solid line) and molecules (dotted line) as a function of the scattering angle. Note, $S_{44} = S_{33}$.

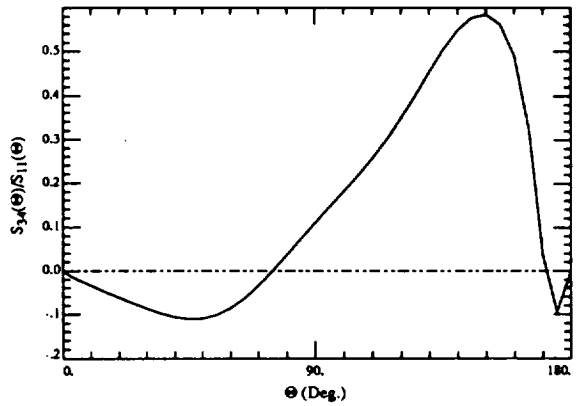

Figure 1d. S_{34} element of the scattering matrix for aerosols (solid line) and molecules ($S_{34} = 0$) as a function of the scattering angle. Note, $S_{43} = -S_{34}$.

1 along with those for Rayleigh scattering.

Samples of the differences between the two codes are provided in Tables 1 and 2. In the tables, "FMC" stands for Forward Monte Carlo, "SOM" for Successive Order Method, and "10^7 Diff" is the % difference between the two [100*(FMC-SOM)/SOM] when 10 million photon histories are followed, while for "10^8 Diff" 100 million are followed. The Rayleigh and aerosol optical thickness are $\tau_r = 0.1$ and $\tau_a = 0.2$, respectively. The aerosol and molecules are uniformly mixed in a single layer. The single scattering albedo is 1 (no absorption). The solar zenith angle θ_0 is 60°, and three viewing directions (specified by the polar and azimuth angles θ and ϕ) are examined:

View 1: $\theta = 2.28°$, $\phi = 180°$

View 2: $\theta = 39.88°$, $\phi = 90°$

View 3: $\theta = 60.15°$, $\phi = 0°$

For the rough ocean surface cases, the Cox-Munk surface slope standard deviation[5] $\sigma = 0.2$, which corresponds to a wind speed of approximately 7.5 m/s. Unidirectional wave shadowing[1,3] of one wave by another is utilized in the *incident* direction only.

In Table 1 we present the results for the case of a flat sea surface. They indicate that for view 1 and view 2 the difference in the two codes for the computed Stokes vector is $\lesssim 0.1\%$. The result for view 3 is very poor; however, this is due entirely to the fact that an insufficient number of Fourier orders (16) in the azimuthal decomposition of the radiance was used in the SOM computation. This leads to a significant error in the computed radiance when $\theta = \theta_0$ because the radiance distribution exiting the top of the atmosphere has a sharp maximum near the specular image of the sun. This results from small-angle forward scattering by the aerosol followed or preceeded by reflection from the sea surface. A significantly larger number of Fourier orders would be required to accurately predict the radiance in this geometry using the SOM. If the aerosol is removed and a pure molecular-scattering atmosphere is considered, this large difference disappears and the error is comparable to that at for the other two views. We believe that in this geometry the radiance predicted by the Monte Carlo is far more accurate, as it does not suffer the need for Fourier decomposition. For $\phi = 0$ (views 1 and 3) a rough estimate of the Monte Carlo statistical fluctuation can be ascertained by the magnitude of the component U which must be identically zero in this geometry. For view 1, this is $\sim 10^{-4}$ of I, which is consistent with an error of the order of 0.01% in I.

Table 2 provides the differences between the two codes in the case of a wind roughened sea surface. The differences for 10^7 photon histories are now larger than in Table 1; however, increasing to 10^8 photon histories significantly improves the agreement between the two codes. Note that in this case the anomalous error seen in Table 1 for view 3 is absent. The radiance is now a smoother function of direction near the specular image of the sun than for a flat ocean, and thus, fewer Fourier orders are required to accurately compute the radiation field. The computations provided *do not* contain the contribution due to direct sun glitter, i.e., the contribution from photons that reflect off the sea surface *without* interacting with the atmosphere. This component is absent in the Monte Carlo because the first collision is forced in the medium to reduce the statistical fluctuations. In the SOM, this component is removed from the computation because it would require using an enormous number of Fourier orders.[1] This is no blemish, however, since the direct sun glitter can be computed *exactly* in a very simple manner given the surface slope statistics. Thus, for the results in the tables, *sky glitter is included*, but if direct sun glitter is desired it must be computed separately

and added to the radiances provided by the code. Finally, it is important to note that to provide the best possible simulation of the rough surface effects, the Monte Carlo code treats multiple scattering by the sea surface, while the SOM code does not. Because of this, perfect agreement for the rough sea surface case is not possible.

We believe the results provided in the test above validates that both codes are capable of computing vector radiances with errors less than $\sim 0.1\%$ in the I component (unless θ is close to θ_0 for the SOM code). The Monte Carlo code will be used to study the performance of the atmospheric correction algorithm under more realistic conditions - a vertically stratified aerosol (type and concentration), a rough sea surface, and test pseudo data generated with full consideration of polarization of the light field.

(iii) Using the Monte Carlo simulation code described above, we have started a study of the error in the atmospheric correction algorithm caused by ignoring polarization. That is, as described in our ATBD for Normalized Water-leaving Radiance, the atmospheric correction algorithm uses a set of lookup tables relating the radiance produced by all photons interacting with the aerosol and those interacting with *both* aerosols and air molecules (Rayleigh scattering) to the radiance that would be observed from the aerosol alone were the radiative transfer process governed by single scattering. These lookup tables were generated for a set of candidate aerosol models and are based on $\sim 33,000$ separate radiative transfer simulations (including all orders of multiple scattering). Their generation, therefore involved a considerable investment in computational resources. To keep the table-generation time to a minimum, the approximation of scalar radiative transfer theory (polarization ignored) was employed. Thus, we need to understand the influence of this approximation on the correction algorithm. To effect this, we simply use our newly-developed Monte Carlo code to simulate the radiance under exact vector radiative transfer theory (effects of polarization on the transfer process are considered). Here, we report the results of the initial studies to assess the error in the algorithm caused by generating the lookup tables using scalar transfer theory.

In the initial studies, two comparisons are carried out. The Monte Carlo code is set to operate in a two-layer mode, with aerosols in the lower layer and all of the Rayleigh scattering confined to the upper layer. The sea surface is assumed to be flat (no wind). Thus the aerosol structure of

Table 1a: Comparison of Stokes Vector Calculations

Flat Ocean Surface; View 1

	I	Q	U	V
FMC	0.11569E-01	−0.46231E-02	0.91547E-06	0.19360E-06
SOM	0.11580E-01	−0.46257E-02	0.82666E-09	−.16649E-12
10^7 Diff (%)	0.02	−0.06	− − −	− − −

Table 1b: Comparison of Stokes Vector Calculations

Flat Ocean Surface ; View 2

	I	Q	U	V
FMC	0.14445E-01	0.50866E-02	−0.40972E-02	0.86810E-05
SOM	0.14446E-01	0.50905E-02	−0.41022E-02	0.36941E-04
10^7 Diff (%)	−0.01	−0.08	−0.12	− − −

Table 1c: Comparison of Stokes Vector Calculations

Flat Ocean Surface; View 3

	I	Q	U	V
FMC	0.23151E+00	−0.18589E+00	-0.46336E-05	0.89707E-07
SOM	0.23519E+00	−0.18908E+00	0.0	0.0
10^7 Diff (%)	−1.56	−1.69	− − −	− − −

Table 2a: Comparison of Stokes Vector Calculations

Rough Ocean Surface; No Direct Sun Glitter; View 1

	I	Q	U	V
FMC	0.11631E-01	−0.46800E-02	−0.13808E-05	0.29246E-06
SOM	0.11654E-01	−0.46907E-02	−0.83606E-09	0.67416E-12
10^7 Diff (%)	−0.20	−0.23	− − −	− − −
10^8 Diff (%)	−0.10	−0.19	− − −	− − −

Table 2b: Comparison of Stokes Vector Calculations

Rough Ocean Surface; No Direct Sun Glitter; View 2

	I	Q	U	V
FMC	0.14439E-01	0.50779E-02	−0.41288E-02	−.85647E-05
SOM	0.14461E-01	0.50948E-02	−0.41417E-02	−.53699E-05
10^7 Diff (%)	−0.15	−0.33	−0.31	− − −
10^8 Diff (%)	−0.04	−0.15	−0.12	− − −

Table 2c: Comparison of Stokes Vector Calculations

Rough Ocean Surface; No Direct Sun Glitter; View 3

	I	Q	U	V
FMC	0.64462E-01	−0.29315E-01	−0.29313E-05	−.22861E-06
SOM	0.64610E-01	−0.29438E-01	−0.99255E-09	0.46572E-10
10^7 Diff (%)	−0.23	−0.42	− − −	− − −
10^8 Diff (%)	−0.16	−0.33	− − −	− − −

the atmosphere and the sea surface is identical to that used in preparation of the lookup tables; however, the computed test radiances will include the influence of the polarization induced by scattering from the atmosphere and reflection from the surface. We start be examining a situation in which the test model of the aerosol is one of the candidate aerosol models. In this case, were scalar radiative transfer theory the correct physics, and were the implementation of the algorithm

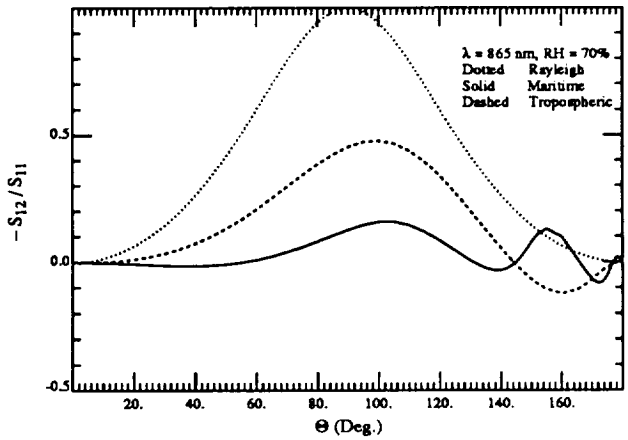

Figure 2a.

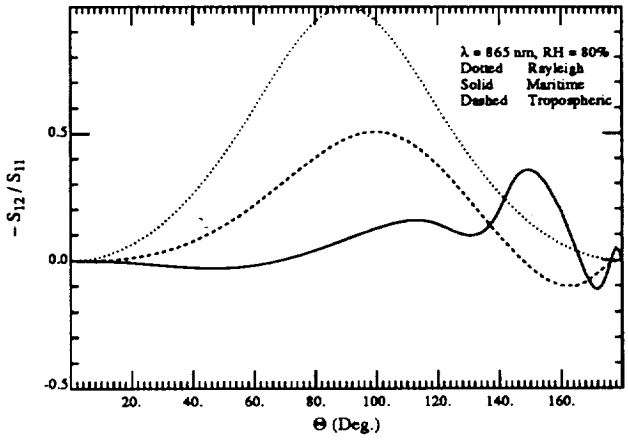

Figure 2b.

Figure 2. Degree of polarization of Rayleigh scattering and scattering by aerosols modeled as Maritime and Tropospheric: (a) RH = 70%; and (b) RH = 90%.

(see ATBD) exact, application of the correction algorithm to the test pseudo data generated by the Monte Carlo code operating in the scalar mode should yield a perfect atmospheric correction. The difference between application of the algorithm to test pseudo data generated by the Monte Carlo code operating in the scalar mode and operating in the full vector mode provides the polarization error in the algorithm under the most ideal conditions.

The degree of polarization of scattering for the test models used in this analysis is compared with that for molecular scattering (Rayleigh) at 865 nm in Figure 2. Figure 2a is for the Shettle and Fenn[6] Maritime and Tropospheric test models with a relative humidity (RH) of 70%. These

are actually members of the set of candidate aerosol models used in the algorithm. In contrast, Figure 2b is for models with with RH = 80%. These models are not members of the candidate set, therefore, they provide a more realistic test of the performance of the algorithm, and they were used for this purpose by Gordon and Wang.[7] Note that both the Tropospheric and Maritime models display considerably different polarization properties, and are both significantly different from Rayleigh scattering. Note also, that the degree of polarization of the Maritime model at RH = 80% is considerably different from that at RH = 70% in the important backscattering directions, 120°–180°.

The computations of the radiance leaving the top of the atmosphere are carried out for seven sun–viewing geometries: $\theta \approx 0$ with $\theta_0 = 20°$, 40°, and 60°, corresponding to viewing near the center of the MODIS scan; and $\theta \approx 45°$ and $\phi = 90°$ with $\theta_0 = 0, 20°, 40°$, and 60°, corresponding to viewing near the edge of the MODIS scan. Figure 3 provides $\Delta\rho$, the error in the water-leaving radiance at 443 nm after application of the correction algorithm to the simulations, as a function of the solar zenith angle, using the Maritime aerosol model at 70% RH for aerosol optical thicknesses of 0.2 and 0.4 at 865 nm. Recall that the first step in atmospheric correction is computation and removal of the radiance produced by Rayleigh scattering. In testing the algorithm throughout its development, the Rayleigh contribution was computed using scalar theory as was the ocean-atmosphere radiance. However, it is well known that ignoring polarization can cause significant errors in the Rayleigh contribution,[8] and in CZCS processing this contribution was determined using vector radiative transfer theory.[9] Thus, we expect that when using test pseudo data generated by a code using vector theory (or when applying the algorithm to actual MODIS imagery) it will be necessary to compute the Rayleigh contribution using vector theory. In contrast, when test pseudo data is generated using scalar theory, scalar theory must also be used to compute the Rayleigh contribution. Because of this, on each panel of the figure there are the results of three different applications of the algorithm. The first is the "S–S" case in which the results of a scalar computation of the total radiance are used as test pseudo data, and the Rayleigh contribution is also computed using scalar theory. This corresponds to the situation under which the algorithm was developed, and in the absence of statistical fluctuations in the Monte Carlo simulations and inaccuracies in the implementation of the correction algorithm, $\Delta\rho$ should be negligible. The second is the "V–S"

case in which the top-of-atmosphere radiance is computed using vector theory but the Rayleigh contribution is computed using scalar theory. This would represent what on would expect if the algorithm were applied to MODIS imagery using a scalar computation of the Rayleigh contribution. In the final application of the algorithm, "V–$\tilde{V}$", the test pseudo data is computed using vector theory, as is the Rayleigh contribution. This simulates using the algorithm with MODIS imagery and correctly computing the Rayleigh contribution with vector theory.

The results presented in Figure 3 suggest that the implementation of the correction algorithm is excellent (S–S errors are $\lesssim 0.0008$ and often much less even for $\tau_a(865) = 0.4$). Furthermore, they show that when applying the algorithm to MODIS imagery the Rayleigh contribution must be computed using vector theory (V–S error is very large). Finally, the difference between the S–S and V–V results suggest that the errors caused by generating the atmospheric correction lookup tables using scalar theory are not excessive, although they are seen to increase with increasing $\tau_a(865)$, i.e., as aerosol scattering (and therefore polarization) becomes increasingly more important compared to Rayleigh scattering.

Similarly Figures 4 and 5 provide the comparison of the error in the water leaving radiance for the Maritime and Tropospheric aerosol models with RH = 80%. Recall that these models are *not* members of the candidate aerosol models and therefore one would expect larger errors than seen in Figure 3. For the Maritime case (Figure 4) the overall accuracy is similar to that in Figure 3; however, for the Tropospheric case (Figure 5) the error becomes excessive for $\tau_a(865) = 0.4$ for both the S–S and V–V algorithms. This breakdown of the algorithm is caused by the large aerosol optical depth a 443 nm (~ 1) which is actually outside the range of the computations used to prepare the lookup tables (i.e., requires extrapolation as opposed to interpolation in the lookup tables). However, the difference between the S–S and V–V algorithms is approximately independent of the optical depth which implies that the polarization effects are only a weak function of τ_a. The differences between the S–S and V–V algorithms for the results provided in Figures 3–5 show some consistent similarities. For example, in all of the cases at the scan edge the V–V results are lower than the S–S for $\theta_0 < 40°$ and higher for $\theta_0 > 40°$, with essentially no difference at $\theta_0 = 40°$. In contrast, for viewing near the scan center the V–V results are consistently lower than the S–S.

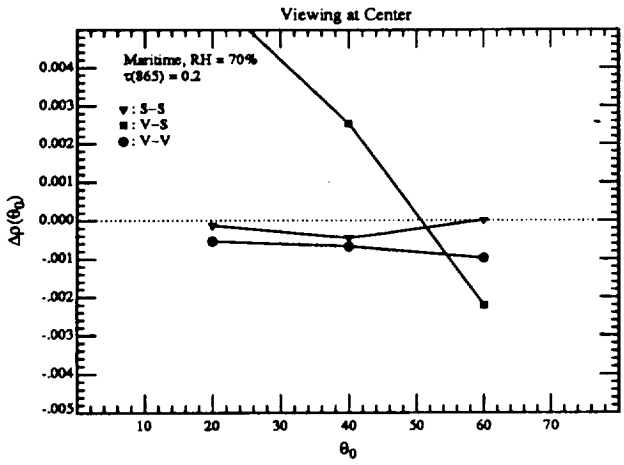

Figure 3a.

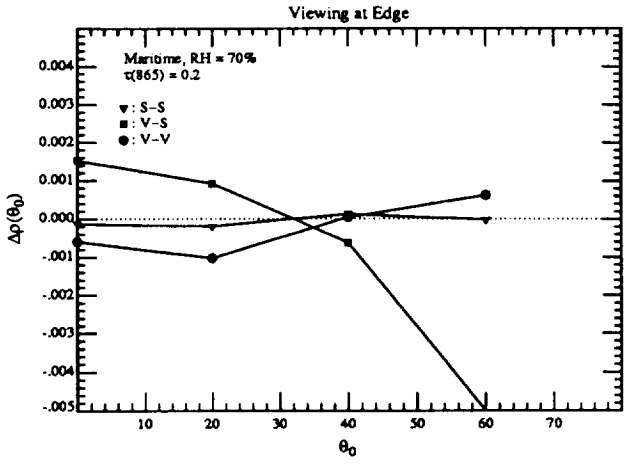

Figure 3b.

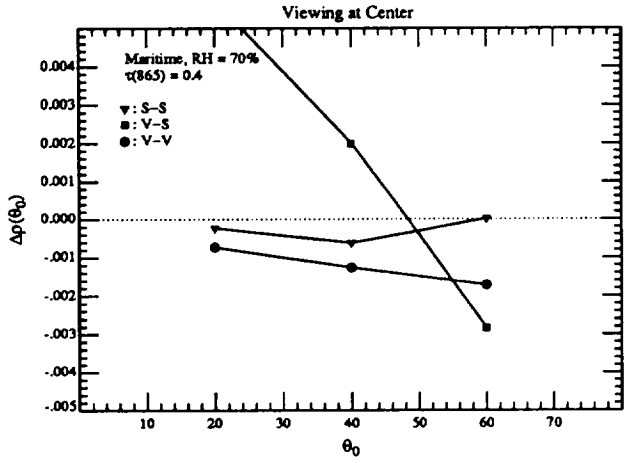

Figure 3c.

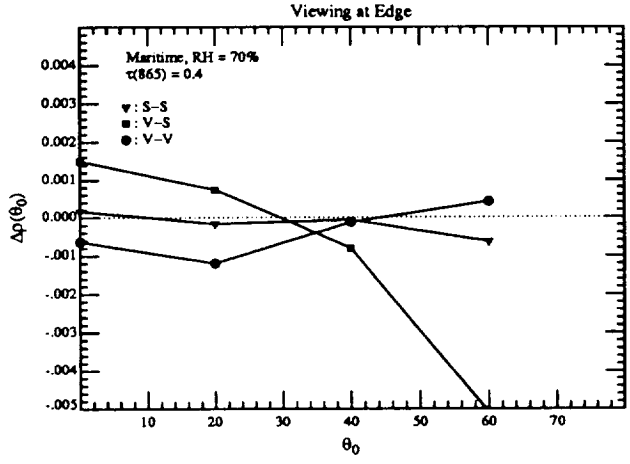

Figure 3d.

Figure 3. Error in the the water-leaving reflectance at 443 nm for the Maritime aerosol model with RH = 70%: (a) scan center with $\tau_a(865) = 0.2$ and $\tau_a(443) = 0.2614$; (b) scan edge with $\tau_a(865) = 0.2$ and $\tau_a(443) = 0.2614$; (c) scan center with $\tau_a(865) = 0.4$ and $\tau_a(443) = 0.5228$; and (d) scan edge with $\tau_a(865) = 0.4$ and $\tau_a(443) = 0.5228$.

It is noteworthy that the differences between V–V and S–S for the Maritime model with RH = 70% and $\tau_a(865) = 0.4$ (Figures 3c and 3d) and the Tropospheric model with RH = 80% and $\tau_a(865) = 0.2$ (Figures 5a and 5b) are practically identical. Both of these cases have $\tau_a(443) \approx 0.5$ but the polarization properties of the aerosol models are completely different: the Tropospheric model being much closer to Rayleigh scattering than the Maritime model (Figure 2).

Thus far this study yields two important conclusions: (1) that most of the error due to the neglect of polarization can be removed by computing the Rayleigh contribution to the total reflectance using vector theory; and (2) the residual error due to the neglect of polarization in constructing the lookup tables is usually ~ 0.001 and appears to vary in a systematic manner with viewing geometry.

(iv) No work was performed on this task during this reporting period.

(v) No work was performed on this task during this reporting period.

c. Data/Analysis/Interpretation: See item **b** above.

d. Anticipated Future Actions:

(i) We will continue our analysis of the existing simulations from the three-layer code to try to understand why the thin cirrus cloud simulations appear to yield anomalous results (See Appendix 1).

(ii) None. This task is now complete.

(iii) We will continue work on the effect of polarization on atmospheric correction.

(iv) We will begin this study using the Monte Carlo code developed under task **(ii)**.

(iv) We will begin this study using the Monte Carlo code developed under task **(ii)**.

e. Problems/Corrective Actions:

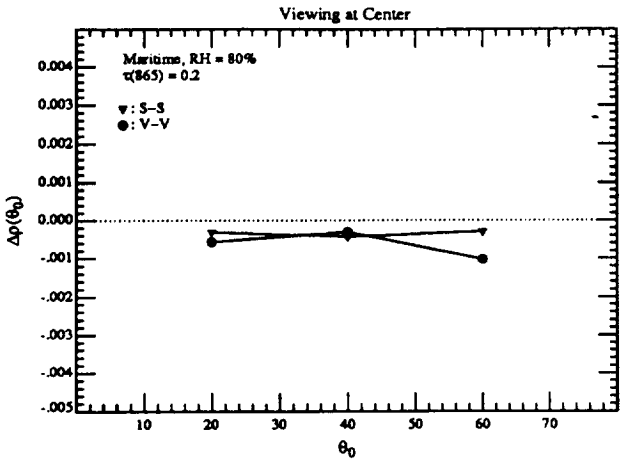

Figure 4a.

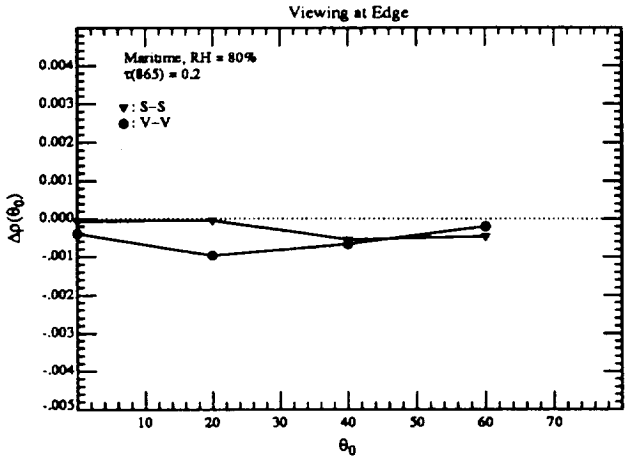

Figure 4b.

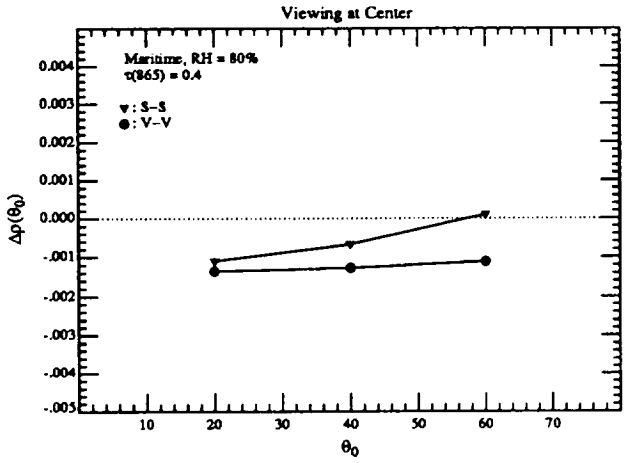

Figure 4c.

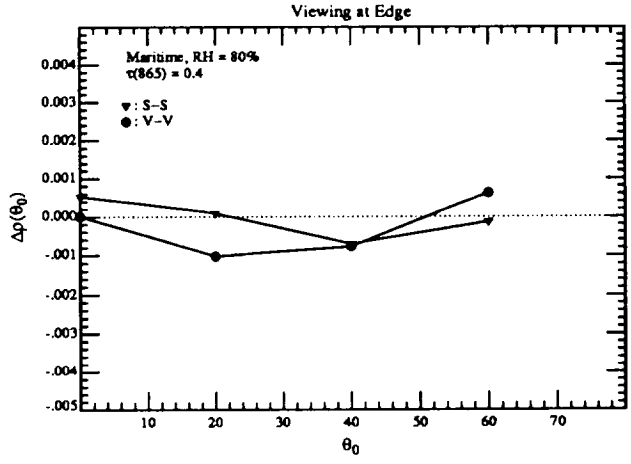

Figure 4d.

Figure 4. Error in the the water-leaving reflectance at 443 nm for the Maritime aerosol model with RH = 80%: (a) scan center with $\tau_a(865) = 0.2$ and $\tau_a(443) = 0.2311$; (b) scan edge with $\tau_a(865) = 0.2$ and $\tau_a(443) = 0.2311$; (c) scan center with $\tau_a(865) = 0.4$ and $\tau_a(443) = 0.4621$; and (d) scan edge with $\tau_a(865) = 0.4$ and $\tau_a(443) = 0.4621$.

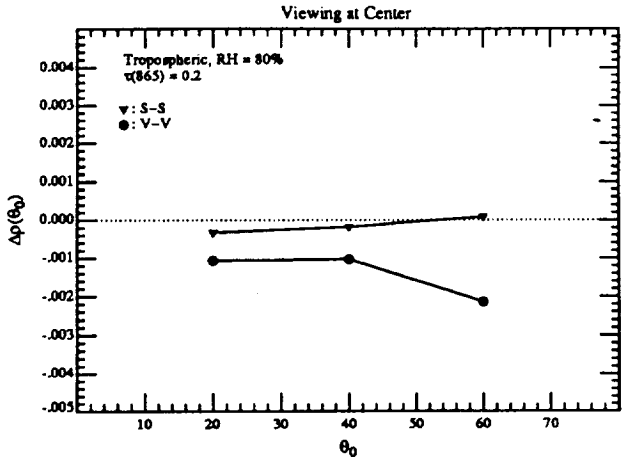

Figure 5a.

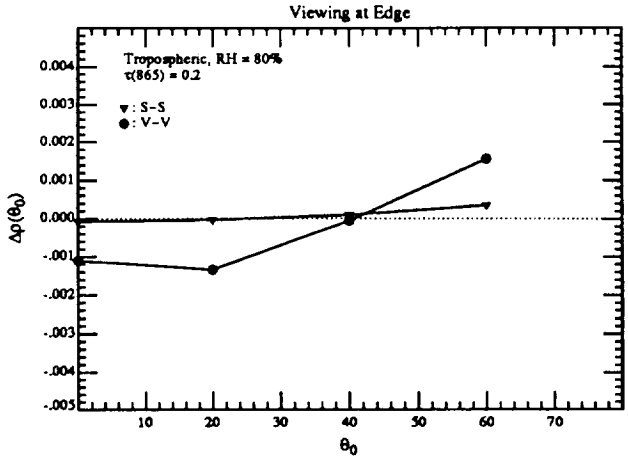

Figure 5b.

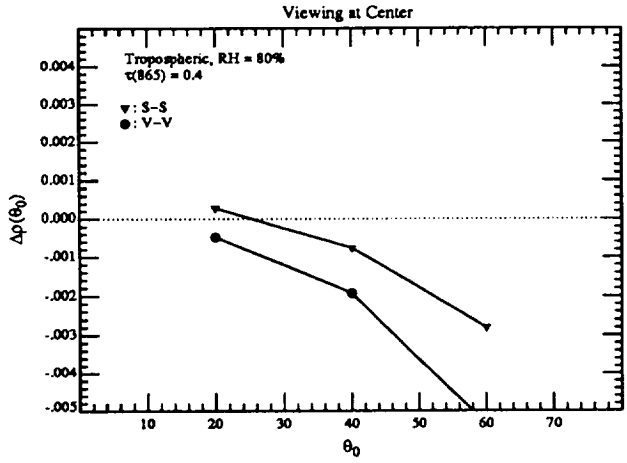

Figure 5c.

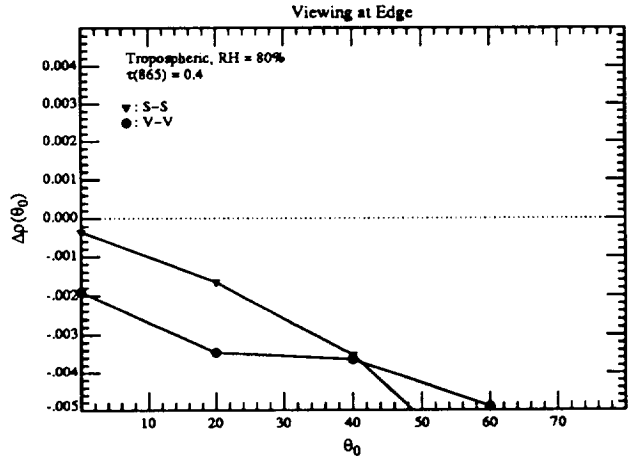

Figure 5d.

Figure 5. Error in the the water-leaving reflectance at 443 nm for the Tropospheric aerosol model with RH = 80%: (a) scan center with $\tau_a(865) = 0.2$ and $\tau_a(443) = 0.4966$; (b) scan edge with $\tau_a(865) = 0.2$ and $\tau_a(443) = 0.4966$; (c) scan center with $\tau_a(865) = 0.4$ and $\tau_a(443) = 0.9933$; and (d) scan edge with $\tau_a(865) = 0.4$ and $\tau_a(443) = 0.9933$.

(i) None.

(ii) None.

(iii) None.

(iv) None.

(v) None.

f. Publications:

K. Ding and H.R. Gordon, Analysis of the influence of O_2 "A"-band absorption on atmospheric correction of ocean color imagery, *Applied Optics* **34**, 2068–2080 (1995).

2. Whitecap Correction Algorithm

a. Task Objectives:

As we have described earlier, we have constructed and tested a whitecap radiometer for development and validation of the whitecap correction algorithm. It was first deployed during the last quarter of 1994. During the deployment we noted several aspects which needed improvement, thus our near term objectives were:

(i) adding a video system to the whitecap radiometer to allow us to understand the radiometer signal and pick out artifacts more accurately,

(ii) rebuilding the 5 channel deck cell (which measures the downwelling irradiance) to increase stability and reliability (also, we would increase the number of channels to 6 to match the upwelling radiance channels of the whitecap radiometers),

(iii) integrating a meteorology package into the whitecap radiometer system,

(iv) reducing and investigating the data obtained during October and November during the Hawaii MOCE-3 cruise, and

(v) participating in a cruise with Dennis Clark during June-July off the coast of Hawaii.

b. Work Accomplished:

We have selected the video system and procured it. We are using a Sony color security camera (SSC-C350), with a HI-8 video recorder (Sony EVC100), and an in-line time/date generator. This will allow us to obtain camera images, with a time date stamp which will allow us to match the data and video images. A housing for this camera is being built, and we expect to have this completed by mid-July.

We have all of the supplies needed for rebuilding the deck cell and we have the meteorology package in house. Both of these items will be finished by mid-July.

The cruise off of Hawaii during June-July was canceled so we could not participate.

c. Data/Analysis/Interpretation:

We have performed some preliminary data reduction of the cruise data, but do not have any conclusions from this work at this point. The basic result thus far has been the requirement for simultaneous video imagery to enable the removal of artifacts. We are continuing analysis of the small quantity of data obtained during the few instances we were able to borrow a video camera from Dennis Clark, in order to develop a procedure for data analysis.

d. Anticipated Future Actions:

We are planning to participate in a short cruise at the end of July out of Ft. Pierce, FL. This will give us a chance to try out our latest modifications locally, and to obtain data in a different locale. We are also planning on participating on field tests with Dennis Clark in Hawaii, when these are scheduled. Presently we anticipate a field test in September in Hawaii during which we

will deploy the complete system. Due to the problems with the SeaWiFS launch, many of the other cruises we anticipated have been delayed, but we will try to find cruises-of-opportunity on which to field this instrument. Because this instrument does not make specific requirements on the ship operations, we believe we will be able to find many opportunities to "piggy-back"on other expeditions.

e. Problems/Corrective Actions: None.

f. Publications: None.

3. In-water Radiance Distribution.

a. Task Objectives:

Acquire radiance data at sea.

b. Work Accomplished: None

c. Data/Analysis/Interpretation: None.

d. Anticipated Future Actions:

Acquire data at sea at the earliest opportunity. This will most likely be a cruise scheduled by Dennis Clark in the Fall.

e. Problems/Corrective Actions: None.

f. Publications: None.

4. Residual Instrument Polarization.

a. Task Objectives: None.

5. Direct Sun Glint Correction.

a. Task Objectives: None.

6. Prelaunch Atmospheric Correction Validation.

a. Task Objectives:

The long-term objectives of this task are two-fold. First, we need to study the aerosol phase function and its spectral variation in order to verify the applicability of the aerosol models used in the atmospheric correction algorithm. Effecting this requires obtaining long-term time series of the aerosol optical properties in typical maritime environments. This will be achieved using a CIMEL sun/sky radiometer that can be operated in a remote environment and send data back to the laboratory via a satellite link. These are similar to the radiometers used by B. Holben and Y. Kaufman. Second, we must be able to measure the aerosol optical properties from a ship during initialization/calibration/validation cruises. The CIMEL-type instrumentation cannot be used (due to the motion of the ship) for this purpose. The required instrumentation consists of an all-sky camera (which can measure the entire sky radiance, with the exception of the solar aureole region, from a moving ship), an aureole camera (specifically designed for ship use), and a hand-held sun photometer. We have a suitable sky camera and sun photometer and must construct an aureole camera. Our objective for this calendar year is (1) to assemble, characterize and calibrate the solar aureole camera system, (2) to develop data acquisition software, and (3) to test the system. A second objective is to acquire a CIMEL Automatic Sun Tracking Photometer, calibrate it, and deploy it in a suitable location for studying the optical properties of aerosols over the oceans.

b. Work Accomplished:

We have the solar aureole camera system assembled along with a trial version of the data acquisition software. We have taken some test images, and are working to optimize the system performance. We had hoped to field this instrument during the cruise this summer; however as

mentioned in Section **2.b**, it was canceled. We will deploy the instrument in some manner during the fall to obtain aureole data.

We have received the CIMEL instrument, and Dr. Brent Holben (NASA/GFSC) has performed a comparison calibration with his instruments, which have been calibrated at Mauna Loa, HI. We are presently installing the instrument at RSMAS, on Virginia Key in Miami for a short field test. During May we visited a site in the Dry Tortugas, a small set of islands in the Gulf of Mexico off of Key West. The main island is Fort Jefferson, part of the National Park Service. We found two sites at Ft. Jefferson which would be ideal for installation of the CIMEL instrument. This location has little ground reflectance problems, particularly in the infra-red, should provide a maritime atmosphere, and is conveniently close to Miami. As well as providing an excellent location for studying the properties of aerosols over the oceans, we believe it could also serve as an ideal site for MODIS vicarious calibration exercises. After visiting the site, a proposal to locate the CIMEL there was written and forwarded to the park service at Everglades National Park. We are now waiting for a response to this proposal, and given a positive response from the park service and a successful trial at RSMAS, we hope to install the instrument during the next reporting period.

c. Data/Analysis/Interpretation: None

d. Anticipated Future Actions:

We will be acquiring data with the aureole camera system, in conjunction with the sky radiance distribution camera system sometime during this next reporting period. We will finish testing the CIMEL locally and by the end of the next period we will have the CIMEL instrument in place in a suitable location such as the Dry Tortugas.

e. Problems/Corrective Actions: None.

f. Publications: None.

7. Detached Coccolith Algorithm and Post Launch Studies.

a. Task Objectives:

The algorithm for retrieval of the detached coccolith concentration from the coccolithophorid, E. huxleyi is described in detail in our ATBD. The key is quantification of the backscattering coefficient of the detached coccoliths. Our earlier studies showed that calcite-specific backscatter coefficient was less variable than coccolith-specific backscatter coefficient, and this would be more scientifically meaningful for future science that will be performed with this algorithm. The variance of the calcite-specific backscatter has been analyzed for only a few species, thus, we need to examine this in other laboratory cultures and field samples. There is also a relationship between the rate of growth of the calcifying algae and the rate of production and detachment of the coccoliths which needs to be further quantified. With this in mind, the objectives of our coccolith studies are, under conditions of controlled growth of coccolithophores (using chemostats), to define the effect of growth rate on:

- the rate that coccoliths detach from cells (which also is a function of turbulence and physical shear);
- the rates of coccolith production;
- the morphology of coccoliths; and
- the volume scattering and backscatter of coccoliths.

The last aspect of these studies will be to perform shipboard measurements of suspended calcite and estimate its optical backscatter as validation of the laboratory measurements. A thorough understanding of these growth-related properties will provide the basis for a generic suspended calcite algorithm. As with algorithms for chlorophyll, and primary productivity, the natural variance between growth related parameters and optical properties needs to be understood before the accuracy of the algorithm can be determined.

b. Work Accomplished:

Our controlled growth experiments with Emiliania huxleyi terminated during the first week of May. Four growth rates were sampled at steady state, with replication.

c. Data/Analysis/Interpretation: Nothing additional since the last report.

d. Anticipated Future Actions:

All of the data obtained for volume scatter needs to be converted to backscatter values. Moreover, suspended calcite samples that were taken during the experiment need to be analyzed. We are currently switching our atomic absorption measurements to a new Perkin Elmer instrument at the University of Maine. This instrument has a graphite furnace attachment and will give us orders of magnitude more sensitivity. We are currently being trained on its use, and will begin running samples shortly. After the backscatter and calcite samples have been processed, we will proceed to calculate the calcite-specific backscatter coefficients as a function of growth rate (which is the ultimate goal of this experiment). Scanning electron micrographs will also be processed during the next two quarters to examine changes in coccolith morphology as a function of growth rate.

e. Problems/Corrective Actions: None

f. Publications:

Two papers were presented at the "Emiliania huxleyi and the Oceanic Carbon Cycle"meeting in London in April. the abstracts are provided below.

Calcification and Photosynthetic Rates of Coccolithophores Under Steady State Growth

W.M. Balch and J.J. Fritz

Rosenstiel School for Marine and Atmospheric Science

University of Miami

4600 Rickenbacker Causeway

Miami, FL 33155

Carbon fixation of Emiliania huxleyi was studied in light limited, steady state, continuous cultures. Six growth rates were examined ranging from $0.24d^{-1}$ to $1.0d^{-1}$ although the lowest may have been carbon limited and the highest approached washout. Both photosynthesis and calcification increased as a function of growth rate, but the ratio of calcification to photosynthesis (C/P) was not constant; that is, C/P increased from about 0.2 to 0.7 as the growth rate increased from $0.24d^{-1}$ and $0.75d^{-1}$, then the ratio decreased slightly at higher growth rates. Extrapolation of the regression data suggested that there should be zero calcification at a growth rate of about $0.15d^{-1}$. Cells were also given a 30s acidification/neutralization treatment to dissolve their coccoliths, and then carbon fixation was measured. Photosynthesis and calcification increased by about 0.1 pg C $cell^{-1}$ h^{-1} following this treatment. Total carbon fixation rate was predicted by multiplying the total carbon per unit chlorophyll by the respective culture dilution rate. These predictions were almost identical to total carbon incorporation measured using 14C bicarbonate. Nevertheless, to accurately predict only photosynthesis or calcification using this approach also will require the function relating the C/P ratio to growth rate.

A coccolith detachment rate determined from chemostat cultures of the coccolithophore Emiliania huxleyi

J.J. Fritz and W.M. Balch
Rosenstiel School for Marine and Atmospheric Science
University of Miami
4600 Rickenbacker Causeway
Miami, FL 33155

The coccolithophore Emiliania huxleyi (Lohm.) Hay and Mohler is one of the most abundant calcite producing organisms on earth and consequently, the coccoliths represent a major carbon sink in the ocean. This study addresses the rate of detachment of coccoliths from the coccolithophores under controlled growth conditions using light-limited chemostats. Cultures were grown at six different growth rates between 0.24 day^{-1} and 1.00 day^{-1}. Other cell properties including chlorophyll, particulate inorganic carbon, and total particulate carbon, were also investigated with

regard to the growth rate of the cells. The coccolith detachment rate increased linearly with cellular growth rate at almost a 1:1 ratio. Such a change in detachment with growth could affect several processes such as sinking rates of cells and bloom formation. The discussion ends with a section on the importance of sinking to coccolithophores.

8. Other Developments.

The PI participated the MOCEAN Team meeting and the Multisensor Calibration and Validation Workshop in Miami in February 1995. Also, the PI prepared a first draft of a validation plan for normalized water-leaving radiance and forwarded it to Frank Hoge and Wayne Esaias for incorporation into the MODIS Ocean Products Validation Plan. This draft is included here as an appendix. A shortened version was prepared for the report of the Multisensor Calibration and Validation Workshop to be submitted to NASA Headquarters.

In May, the PI attended the CEOS/IVOS Calibration and Validation Workshop and presented a review, *Theoretical Basis of the SeaWiFS/MODIS Normalized Water-leaving Radiance Algorithm (Atmospheric Correction) and its relationship to Vicarious Calibration.*

A method for combining high-altitude aircraft radiance (upwelling) and surface radiance (downwelling) for determination of the columnar aerosol optical properties has been developed. A paper on the subject,

H.R. Gordon and T. Zhang, Columnar Aerosol Properties Over Oceans
by Combining Surface and Aircraft Measurements: Simulations.

was accepted for publication and is now in press in *Applied Optics*. This work could provide a powerful method of studying aerosol properties over the ocean. This paper is attached as Appendix 2. A second study concerning the perturbation of the sky radiance measurements made from islands, caused by the presence of the island itself, has been carried out and a paper

H. Yang, H.R. Gordon and T. Zhang, Island perturbation to the sky radiance over the ocean: Simulations,

was submitted to *Applied Optics*. The paper completed the first review and is now under revision. It is attached as Appendix 3. Both of these have relevance to the "Prelaunch Atmospheric Correction Validation" (Topic 6 above) portion of our research, as well as to the validation of retrieved aerosol properties over the oceans from EOS sensors.

A method for dealing with out-of-band response of ocean color sensors was developed by the PI. A paper

H.R. Gordon, Remote sensing of ocean color: a methodology for dealing with broad spectral bands and significant out-of-band response,

was prepared and submitted to *Applied Optics*. This work is applicable to any ocean color sensor, and the same methodology will be employed for MODIS. It is attached here as Appendix 4.

9. References.

[1] H. R. Gordon and M. Wang, "Surface Roughness Considerations for Atmospheric Correction of Ocean Color Sensors. 1: The Rayleigh Scattering Component," Applied Optics **31**, 4247-4260 (1992).

[2] H. C. van de Hulst, *Multiple Light Scattering* (Academic Press, New York, 1980), 739 pp.

[3] H. R. Gordon and M. Wang, "Surface Roughness Considerations for Atmospheric Correction of Ocean Color Sensors. 2: Error in the Retrieved Water-leaving Radiance," Applied Optics **31**, 4261-4267 (1992).

[4] H. Quenzel and M. Kastner, "Optical properties of the atmosphere: calculated variability and application to satellite remote sensing of phytoplankton," Applied Optics **19**, 1338–1344 (1980).

[5] C. Cox and W. Munk, "Measurements of the Roughness of the Sea Surface from Photographs of the Sun's Glitter," Jour. Opt. Soc. of Am. **44**, 838–850 (1954).

[6] E. P. Shettle and R. W. Fenn, *Models for the Aerosols of the Lower Atmosphere and the Effects of Humidity Variations on Their Optical Properties* (Air Force Geophysics Laboratory, Hanscomb AFB, MA 01731, AFGL–TR–79-0214, 1979).

[7] H. R. Gordon and M. Wang, "Retrieval of water-leaving radiance and aerosol optical thickness over the oceans with SeaWiFS: A preliminary algorithm," Applied Optics **33**, 443–452 (1994).

[8] G. W. Kattawar, G. N. Plass and S. J. Hitzfelder, "Multiple scattered radiation emerging from Rayleigh and continental haze layers. 1: Radiance, polarization, and neutral points," Applied Optics **15**, 632–647 (1976).

[9] H. R. Gordon, J. W. Brown and R. H. Evans, "Exact Rayleigh Scattering Calculations for use with the Nimbus-7 Coastal Zone Color Scanner," Applied Optics **27**, 862–871 (1988).

Appendix 1

Atmospheric correction of ocean color imagery for effects of stratospheric aerosols and cirrus clouds: Simulations

1. Introduction

The radiance exiting the ocean-atmosphere system carries information on the concentration of marine phytoplankton — the first link in the marine food chain — through the variations they produce in the color of the water.[1] The flight of the Coastal Zone Color Scanner (CZCS)[2,3] was a the proof-of-concept mission to demonstrate the feasibility of quantitatively estimating the concentration of chlorophyll a, a photosynthetic pigment contained in phytoplankton and used as a surrogate for their concentration. Based on the success of the CZCS, a number of instruments for ocean color measurements will be launched in the 1990's, e.g., the sea-viewing wide field-of-view sensor (SeaWiFS)[4] and the Moderate resolution Spectroradiometer (MODIS).[5]

The contribution from beneath the sea surface to the radiance exiting the ocean-atmosphere system in the visible is very small, i.e., at most 10-20% of the total in the blue and less at longer wavelengths. The remainder of the radiance is due to scattering from the atmosphere and reflection from the sea surface. Thus, it is of the utmost importance to remove these interfering effects in order to isolate the water-leaving radiance that carries the information regarding phytoplankton. This process is termed atmospheric correction. The CZCS atmospheric correction algorithm,[6] which was based on the single scattering approximation, was not sufficiently accurate to be applied to SeaWiFS and MODIS because they have far better radiometric sensitivity. Gordon and Wang[7] developed a multiple scattering correction algorithm suitable for use with these sensors. This algorithm assumes that all of the aerosol in the atmosphere is in the marine boundary layer and uses aerosol models to deal with the multiple scattering. In some situations, e.g., following volcanic eruptions or when there are thin cirrus clouds present, there can be significant quantities of aerosol in the stratosphere. This degrades the performance of the algorithm. In the case of SeaWiFS, there is no direct way of detecting the presence of such aerosols; however, MODIS is equipped with a spectral band at 1.38 μm that can be used for this purpose. This spectral band is centered on a strong water vapor absorption band and photons penetrating through the stratosphere will usually be absorbed by water vapor in the free troposphere.[8] Thus, any radiance measured at 1.38 μm can, in the first approximation, be assumed to be scattered by the stratospheric aerosol alone. This provides a mechanism for estimating the stratospheric contribution. In this paper we assess

the degradation in atmospheric correction in the presence of stratospheric aerosols. In the case of MODIS, we assume that the radiance measured at 1.38 μm is totally due to the stratosphere and examine several possibilities for using this information in the proposed atmospheric correction algorithm[7] to correct ocean color imagery.

2. The proposed SeaWiFS-MODIS atmospheric correction algorithm

In the absence of stratospheric aerosol, the total reflectance of the ocean-atmosphere system, $\rho_t(\lambda)$, measured at a wavelength λ, can be decomposed as follows:

$$\rho_t(\lambda) = \rho_r(\lambda) + \rho_a(\lambda) + \rho_{ra}(\lambda) + t(\theta_v, \lambda)\rho_w(\lambda), \quad (1)$$

where $\rho_r(\lambda)$ is the radiance resulting from multiple scattering by air molecules (Rayleigh scattering) in the absence of aerosols, $\rho_a(\lambda)$ is the radiance resulting from multiple scattering by aerosols in the absence of the air, and $\rho_{ra}(\lambda)$ is the interaction term between molecular and aerosol scattering.[9] In this equation, t is the diffuse transmittance of the atmosphere along the viewing direction specified by θ_v, the angle between the normal to the sea surface and the sensor.[10] Radiance arising from specular reflection of direct sunlight from the sea surface (sun glitter) has been ignored. This means that the correction cannot be valid near the glitter pattern. The influence of whitecaps has also been ignored under the assumption that their contribution can be removed from an estimate of the surface wind speed.[11] The goal of the atmospheric correction is the retrieval of ρ_w from ρ_t. This is effected by measuring ρ_t in the near infrared (NIR) near 765 and 865 nm for SeaWiFS and 750 and 865 nm for MODIS. In this spectral region, the ρ_w can be taken to be zero because of the strong absorption by the water itself. ρ_r can be computed given an estimate of the atmospheric pressure, so $\rho_a + \rho_{ra}$ can be determined directly in the NIR. Utilizing aerosol models to account for multiple scattering and for the spectral dependence of $\rho_a + \rho_{ra}$, this quantity is extrapolated into the visible, providing ρ_w there.[7] In the absence of stratospheric aerosol, simulations suggest that this algorithm will meet the goal of retrieval of ρ_w at 443 nm with an error $\lesssim$ 0.001–0.002, i.e., an error of $\lesssim$ 5% in ρ_w in the blue in very clear ocean water.

Incorporation of multiple scattering is effected through the use of lookup tables based on a large number (~33,000) radiative transfer simulations using various aerosol models[12] thought to be representative of aerosols occurring over the oceans. In the simulations it was assumed that all of the aerosol is resident in the marine boundary layer, i.e., the simulations are carried out using an accurate (error $\lesssim 0.1\%$) two-layer radiative transfer code with aerosols occupying the lower layer and molecular (Rayleigh) scattering occupying the upper layer.

3. Simulation of the effects of stratospheric aerosol

In situations where there is significant stratospheric aerosol present, the aerosol vertical profile described in Section 2 is very unrealistic. A more realistic profile would be a three-layer atmosphere with aerosol in both the lower and upper layers and molecular scattering in the central layer. This is the profile that we adopt for simulating ρ_t in the presence of stratospheric aerosol.

We examine three different stratospheric aerosol models. The first is the background stratospheric aerosol[13] consisting of a 75% solution of H_2SO_4 with a size distribution given by

$$\frac{dn}{dD} = 81 D \exp(-9\, D),$$

where dn is the number of particles per unit volume with diameters (D) in μm between D and $D + dD$. The second is the El Chichon aerosol,[14] also a 75% solution of H_2SO_4, with a size distribution:

$$\frac{dn}{dD} = 1.79386 \times 10^8\, D^{12.65} \exp(-19.65\, D).$$

The third represents aged volcanic ash. It consists of an absorbing mineral distributed in size according to

$$\frac{dn}{dD} = 1365.33\, D \exp(-11.3137\sqrt{D})$$

with a wavelength-independent index of refraction $m = 1.50 - 0.008i$. For the background and the El Chichon aerosol, the index of refraction is taken from Palmer and Williams.[15] The final aerosol model is that for thin cirrus clouds taken from Takano and Liou.[16] In this case we assume that the scattering properties of the thin cirrus are independent of wavelength. The scattering phase functions for these four models are presented in Figures 1a through 1d, and their spectral variation

in extinction (or stratospheric optical thickness, τ_a) is presented in Figure 2. The first three were calculated from the size distributions and the refractive indices using Mie theory. The fourth was taken from the tabulated values of Ref. 16. Note the significant spectral variation of the shape of some of the aerosol phase functions. In particular, for the background stratospheric aerosol, the phase function at 1380 nm is very uncharacteristic of the phase function in the visible and near infrared.

As suggested above, we simulated the reflectance in the presence of stratospheric aerosol using a three-layer radiative transfer code. The lower layer contained the Shettle and Fenn[12] Maritime aerosol at 80% relative humidity. This was used as the boundary layer aerosol because, in the absence of stratospheric aerosol, the atmospheric correction algorithm is essentially perfect (error in ρ_w found by Gordon and Wang[7] was less than about 0.0005 for this aerosol) and, thus, provides an excellent choice for examination of the interfering effects of the stratospheric aerosol. The upper layer contains the stratospheric aerosol and the middle layer exhibits only molecular scattering. A Fresnel-reflecting flat sea surface constitutes the lower boundary. There is no radiance exiting the ocean, i.e., all photons penetrating the surface are absorbed. In the case of MODIS, to simulate the reflectance at 1380 nm a one-layer model with a totally absorbing lower boundary (no Fresnel reflection) was employed. The rational for this is the assumption that all radiation penetrating through the stratosphere at this wavelength is absorbed by water vapor in the troposphere, so no radiance is reflected to the top of the atmosphere from below the stratospheric layer. Note that for the purpose of utilizing the 1380 nm MODIS band to correct for the stratospheric aerosol, this is the ideal scenario, i.e., all of the reflected radiance at 1380 nm is due to the stratosphere, there is no contamination from Rayleigh scattering in the free troposphere (middle layer), aerosol scattering in the marine boundary layer (lower layer), or reflection from the sea surface.

4. Schemes for correcting for stratospheric aerosol

The stratospheric aerosol contributes to the reflectance at all wavelengths. Thus, in the presence of the stratospheric aerosol layer the reflectance will be changed by an amount $\delta\rho_t^{(a)}$, i.e.,

$$\rho_t^{(a)}(\lambda) = \rho_t(\lambda) + \delta\rho_t^{(a)}(\lambda),$$

where $\rho_t^{(s)}$ is the reflectance of the entire ocean-atmosphere system in the presence of stratospheric aerosol. As much of this contribution as possible should be removed from the visible and NIR bands before applying the atmospheric correction. Thus, the goal is to be able to remove $\delta\rho_t^{(s)}(\lambda)$ from $\rho_t^{(s)}(\lambda)$. This will enable direct application of the atmospheric correction algorithm to $\rho_t(\lambda)$, for which it was developed.

Using the models outlined in Section 3, we carried out simulations of $\rho_t^{(s)}(\lambda)$ for several combinations of stratospheric and boundary-layer optical depths, τ_s and τ_b, respectively. Also, we examined several possibilities for utilizing the 1380 nm band for correction of MODIS for stratospheric aerosols. In this case, as described in Section 3, we assumed that the reflectance at 1380 nm was totally due to the stratospheric aerosol.

The computations of $\rho_t^{(s)}(\lambda)$ were carried out for λ = 443, 765, 865, and 1380 nm. In applying the atmospheric correction algorithm, it was assumed that the aerosol properties in the lower layer were completely unknown. In the case of SeaWiFS, the atmospheric correction algorithm was operated using $\rho_t^{(s)}(\lambda)$, which would be measured in the presence of stratospheric aerosols, in place of $\rho_t(\lambda)$ and the resulting error in $t\rho_w(\lambda)$ at λ = 443 nm was determined. In the case of MODIS, the correction algorithm was operated in several ways as follows. Again, the computations of $\rho_t^{(s)}(\lambda)$ were used as pseudo data.

1. The "measured" reflectances at 443, 765 and 865 are used in the algorithm as usual, i.e., no attention is paid to the fact that a stratospheric aerosol may be present [$\rho_t^{(s)}(\lambda)$ assumed to be $\rho_t(\lambda)$], and the error in the atmospheric correction at 443 nm is determined. This is identical to the case of SeaWiFS described above.

2. The stratospheric aerosol is incorporated into the algorithm by simply subtracting the reflectance at 1380 nm from those at 443, 765, and 865, i.e., $\rho_t(\lambda) = \rho_t^{(s)}(\lambda) - \rho_t^{(s)}(1380)$. These are then inserted into the correction algorithm and the error in the correction at 443 nm is determined.

3. It is assumed that the spectral variation of the optical thickness of the stratospheric aerosol is known, e.g., from measurements from the surface. The reflectance at 1380 nm (due entirely to the stratospheric aerosol) is scaled by the ratio of the stratospheric optical depth at the given λ, $\tau_s(\lambda)$, to that at (or in the case of surface measurements, near) 1380 nm, and subtracted from the measured reflectances at the other wavelengths, i.e.,

$$\rho_t(\lambda) = \rho_t^{(s)}(\lambda) - \frac{\tau_s(\lambda)}{\tau_s(1380)}\rho_t^{(s)}(1380)$$

The $\rho_t(\lambda)$ are then inserted into the correction algorithm and the error in the correction at 443 nm determined.

4. It is assumed that accurate measurements or predictions of the other optical properties of the stratospheric aerosol, the spectral scattering phase function and single scattering albedo, along with the spectral variation of the optical depth are available for the stratospheric aerosol, e.g., from inversions of $\tau_s(\lambda)$ measurements made at the surface to obtain the size distribution, from which the other optical properties are computed.[14] Only the stratospheric aerosol concentration is unknown. It is estimated based on the measurement of $\rho_t^{(s)}(1380)$. The reflectance at 1380 nm is then scaled, by the ratio of the single-scattered stratospheric aerosol reflectances at λ to that at 1380 nm, and subtracted from the reflectances in the visible and NIR, i.e.,

$$\rho_t(\lambda) = \rho_t^{(s)}(\lambda) - \frac{\omega_s(\lambda)\tau_s(\lambda)p_s(\theta_v, \phi_v; \theta_0, \phi_0; \lambda)}{\omega_s(1380)\tau_s(1380)p_s(\theta_v, \phi_v; \theta_0, \phi_0; 1380)}\rho_t^{(s)}(1380),$$

where

$$p_s(\theta_v, \phi_v; \theta_0, \phi_0; \lambda) = P_s(\theta_-, \lambda) + \Big(r(\theta_v) + r(\theta_0)\Big)P_s(\theta_+, \lambda),$$

$$\cos\theta_\pm = \pm\cos\theta_0\cos\theta_v - \sin\theta_0\sin\theta_v\cos(\phi_v - \phi_0),$$

and $r(\alpha)$ is the Fresnel reflectance of the interface for an incident angle α. The parameters $\tau_s(\lambda)$, $\omega_s(\lambda)$, and $P_s(\alpha, \lambda)$ are, respectively, the stratospheric aerosol optical thickness, single scattering albedo, and scattering phase function for a

scattering angle α. The angles θ_0 and ϕ_0 are, respectively, the zenith and azimuth angles of a vector from the point on the sea surface under examination (pixel) to the sun, and likewise, θ_v and ϕ_v are the zenith and azimuth angles of a vector from the pixel to the sensor. These are measured with respect to the *upward* normal so θ_v and θ_0 are both less than 90°. At 1380 nm, $r(\alpha)$ is set to zero since the radiation at this wavelength cannot interact with the surface. The resulting values of $\rho_t(\lambda)$ are then inserted into the correction algorithm and the error at 443 nm is determined. This procedure is based on the assumption that the stratospheric aerosol enhancement of ρ_t is all due to single scattering.

5. As in (4) it is assumed that all of the optical properties of the aerosol are known except the concentration. A one-layer multiple scattering code (with a totally absorbing lower surface to represent the troposphere) is used to determine $\tau_s(1380)$ from $\rho_t^{(s)}(1380)$. This determines all of the optical properties of the stratospheric aerosol. These properties are inserted into a one-layer multiple scattering code (with a Fresnel-reflecting sea surface as the lower boundary) to compute $\delta\rho_t^{(s)}(\lambda)$, which is subtracted from the measured reflectances $\rho_t^{(s)}(\lambda)$ to provide $\rho_t(\lambda)$. The resulting values of $\rho_t(\lambda)$ are then inserted into the correction algorithm and the error at 443 nm is determined. This procedure is based on the assumption that there is *no radiative interaction* between the stratospheric aerosol layer and the other two layers in the visible.

6. Except for the step in which $\delta\rho_t^{(s)}(\lambda)$ is removed from $\rho_t(\lambda)$, this is identical to procedure 5. Once all of the optical properties of the stratospheric aerosol are known, they are inserted into a *two-layer* multiple scattering code (as opposed to a *one-layer* code in procedure 5 above) with a Fresnel-reflecting sea surface as the lower boundary. The top layer consists of the stratospheric aerosol and the lower layer has only Rayleigh scattering. This incorporates the Rayleigh-stratospheric aerosol

interaction explicitly (albeit approximately because of the absence of the tropospheric aerosol), leaving only the Rayleigh-tropospheric aerosol and stratospheric-tropospheric aerosol interactions not addressed. After subtracting the result of this computation from $\rho_t^{(s)}(\lambda)$, the result is inserted into the standard correction algorithm in which allowance is made for the fact that ρ_r has already been removed along with the stratospheric component. This approach is possible because the properties of the Rayleigh scattering layer are completely known.

These approaches clearly require increasing amounts of knowledge concerning the optical properties of the stratospheric aerosol. Although knowledge of these properties may be good in certain instances, e.g., the El Chichon aerosol,[14] in general such will not be available.

4. Results

We begin by presenting the results obtained using these procedures for cases with the El Chichon aerosol in the stratosphere with $\tau_s = 0.05$ and 0.15, and a Maritime aerosol (relative humidity 80%) with $\tau_b = 0.15$ in the marine boundary layer. In the absence of stratospheric aerosol, the algorithm yields an almost perfect atmospheric correction. Figures 3 and 4 provide the error in the recovered value of $t\rho_w(443)$ for each of the procedures above at the scan center ($\theta_v = 0$) and the scan edge ($\theta_v \approx 45°$), as a function of the solar zenith angle. The procedure description is given on the figures with the symbols. The procedure numbers run from 0 to 6 starting at the top. The the symbols "3L," "2L," "R," "S," and "(R+S)" stand for radiances computed from a three-layer model, a two-layer model, a one-layer model with Rayleigh scattering only, a one-layer model with stratospheric aerosol scattering only, and a two-layer model with stratospheric aerosols on the top and molecular scattering in the bottom. Thus, "3L–(R+S)" refers to procedure 6. The last symbol "2L–R" provides the error that would be observed in the absence of the stratospheric aerosol. The goal in the presence of the stratospheric aerosol is that the error approach that which would be obtained were it *absent*.

Examination of similar plots for the individual cases examined reveal the following for the best correction procedure, "3L-(R+S)": (1) for a given stratospheric aerosol model, the largest values of $\Delta\rho$ occur at the scan edge with $\theta_0 = 60°$ where one would expect the largest effect of multiple scattering; however, for the cirrus cloud model, the largest error occurs for $\theta_0 = 0$; (2) for a given θ_0, the error for viewing at the scan center is usually less than the error at the scan edge; (3) with the exception of the cirrus cloud results, the errors are usually negative (too much radiance has been assigned to the atmosphere) with the aged volcanic aerosol more negative than the others, presumably due to its moderate absorption; and (4) the general patterns of the error as a function of θ_0 at the scan center and edge for a given model remain the same as τ_b and τ_s are varied, but patterns for different stratospheric models are not similar. From these observations it is clear that the results for the cirrus cloud model are significantly different from those of the other three, i.e., the cirrus results are anomalous. This difference must be due to the nature of the cirrus scattering phase function compared to the others (Figure 1), however, the precise way in which the anomalies are produced by the phase function is not understood. Thus, as might be expected, the most complex method of dealing with the stratospheric aerosol (procedure 6 in Section 4, which is applicable to MODIS) yields the best overall correction.

The results of all of the simulations can be summarized better by presenting the data shown in Figures 3 and 4 in a different manner. Instead of plotting the actual error as a function of θ_0 for the two viewing angles, we present histograms of the error as a function of the stratospheric aerosol removal algorithm (procedures 1–6) in Figures 5—8. The taller bars represent the maximum value of $|t\rho_w(\lambda)|$ for $\lambda = 443$ nm for the seven combinations. The shorter bars in the histogram represent the average of $|t\rho_w(\lambda)|$ for $\lambda = 443$ nm over the remaining six θ_0–θ_v combinations. The horizontal dashed line is the upper limit of the acceptable error, i.e., 0.002. This manner of presentation makes it very easy to compare various procedures for dealing with the stratospheric aerosol with MODIS and for estimating the error when stratospheric aerosols are ignored, e.g., with SeaWiFS.

Several observations can be made regarding the results presented in Figures 5–8. Perhaps the most evident is the fact the maximum error (long bars) for the cirrus cloud model is so much larger than that of the others. This is particularly noticeable at low values of τ_b. This error always occurs

at $\theta_0 = 0°$ at the scan edge, and its cause is not understood; however, upon application of procedure number 6, "3L–(R+S)," the cirrus cloud error becomes similar in magnitude to the rest, indicating that there is a very strong interaction between the stratospheric aerosol and the Rayleigh-scattering middle layer. It is also evident that in nearly all cases, the most complex correction procedure "3L–(R+S)" yields the best results. Simpler procedures, e.g., 4 and 5 that also require full knowledge of the optical properties of the stratospheric aerosol, provide similar results for the background and El Chichon models, but inferior results for the cirrus cloud and aged volcanic aerosol models. Unless the most complex procedure can be used, it appears that the simplest procedures 1 and 2 usually provide as good a correction. Recall that procedure number 1 is to ignore the presence of the stratospheric aerosol, e.g., as in SeaWiFS.

5. Preliminary Conclusions

As discussed above, the most complex algorithm we investigated, "3L–(R+S),"and which could be used with MODIS, is usually the best. However, it requires full knowledge of the optical properties of the stratospheric aerosol. In the case of volcanically injected stratospheric aerosol, estimates of these properties could be obtained from surface measurements, e.g., El Chichon.[14] Implementation would then require computation of "R+S" as a function of τ_a and the sun-viewing geometry. Since such aerosols are relatively stable, such an approach may be feasible. In the case of thin cirrus clouds this appears to be the only approach that is fruitful; however, with the exception of removing the large error for $\theta_0 = 0$ near the scan edge, the improvement gained by using this complex approach is minimal.

Before suggesting that the "3L–(R+S)" algorithm be implemented, it is felt that sensitivity studies regarding the accuracy with which the optical properties of the stratospheric aerosol are required should be carried out.

References

[1] H. R. Gordon and A. Y. Morel, *Remote Assessment of Ocean Color for Interpretation of Satellite Visible Imagery: A Review* (Springer-Verlag, New York, 1983), 114 pp.

[2] W. A. Hovis, D. K. Clark, F. Anderson, R. W. Austin, W. H. Wilson, E. T. Baker, D. Ball, H. R. Gordon, J. L. Mueller, S. Y. E. Sayed, B. Strum, R. C. Wrigley and C. S. Yentsch, "Nimbus 7 coastal zone color scanner: system description and initial imagery," Science **210**, 60–63 (1980).

[3] H. R. Gordon, D. K. Clark, J. L. Mueller and W. A. Hovis, "Phytoplankton pigments derived from the Nimbus–7 CZCS: initial comparisons with surface measurements," Science **210**, 63–66 (1980).

[4] S. B. Hooker, W. E. Esaias, G. C. Feldman, W. W. Gregg and C. R. McClain, *SeaWiFS Technical Report Series: Volume 1, An Overview of SeaWiFS and Ocean Color* (NASA, Greenbelt, MD, Technical Memorandum 104566, July 1992).

[5] V. V. Salomonson, W. L. Barnes, P. W. Maymon, H. E. Montgomery and H. Ostrow, "MODIS: Advanced Facility Instrument for Studies of the Earth as a System," IEEE Geosci. Rem. Sens. **27**, 145–152 (1989).

[6] H. R. Gordon and D. K. Clark, "Atmospheric effects in the remote sensing of phytoplankton pigments," Boundary-Layer Meteorology **18**, 299–313 (1980).

[7] H. R. Gordon and M. Wang, "Retrieval of water-leaving radiance and aerosol optical thickness over the oceans with SeaWiFS: A preliminary algorithm," Applied Optics **33**, 443–452 (1994).

[8] B. -C. Gao, A. F. H. Goetz and W. J. Wiscombe, "Cirrus cloud detection from airborne imaging spectrometer data using the 1.38 micron water vapor band," Geophysical Research Letters **20**, 301–304 (1993).

[9] P. Y. Deschamps, M. Herman and D. Tanre, "Modeling of the atmospheric effects and its application to the remote sensing of ocean color," Applied Optics **22**, 3751–3758 (1983).

[10] H. R. Gordon, D. K. Clark, J. W. Brown, O. B. Brown, R. H. Evans and W. W. Broenkow, "Phytoplankton pigment concentrations in the Middle Atlantic Bight: comparison between ship determinations and Coastal Zone Color Scanner estimates," Applied Optics **22**, 20–36 (1983).

[11] H. R. Gordon and M. Wang, "Influence of Oceanic Whitecaps on Atmospheric Correction of SeaWiFS," Applied Optics **33**, 7754–7763 (1994).

[12] E. P. Shettle and R. W. Fenn, *Models for the Aerosols of the Lower Atmosphere and the Effects of Humidity Variations on Their Optical Properties* (Air Force Geophysics Laboratory, Hanscomb AFB, MA 01731, AFGL–TR–79-0214, 1979).

[13] WCP–112, *A preliminary cloudless standard atmosphere for radiation computation* (World Meteorological Organization, WMO/TD–No. 24, Geneva, 1986).

[14] M. D. King, Harshvardhan and A. Arking, "A Model of the Radiative Properties of the El Chichón Stratospheric Aerosol Layer," Journal of Climate and Applied Meteorology **23**, 1121–1137 (1984).

[15] K. F. Palmer and D. Williams, "Optical constants of sulfuric acid; Application to the clouds of Venus?," Applied Oprics **14**, 208–219 (1975).

[16] Y. Takano and K. N. Liou, "Solar Radiative Transfer in Cirrus Clouds. Part I: Single-Scattering and Optical Properties of Hexagonal Ice Crystals," Jour. Atm. Sci. **46**, 224–240 (1989).

[17] P. J. Reddy, F. W. Kreiner, J. J. Deluisi and Y. Kim, "Aerosol Optical Depths Over the Atlantic Derived From Shipboard Sunphotometer Observations During the 1988 Global Change Expedition," Global Biogeochemical Cycles **4**, 225–240 (1990).

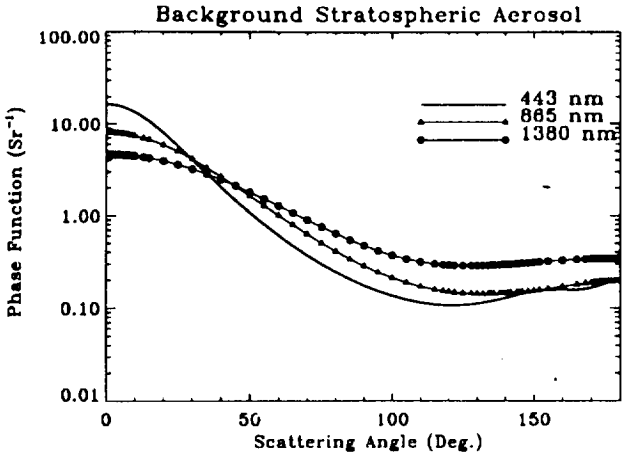

Figure 1a.

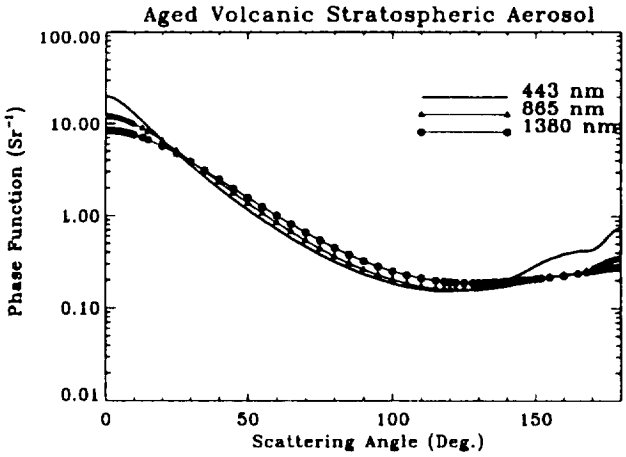

Figure 1b.

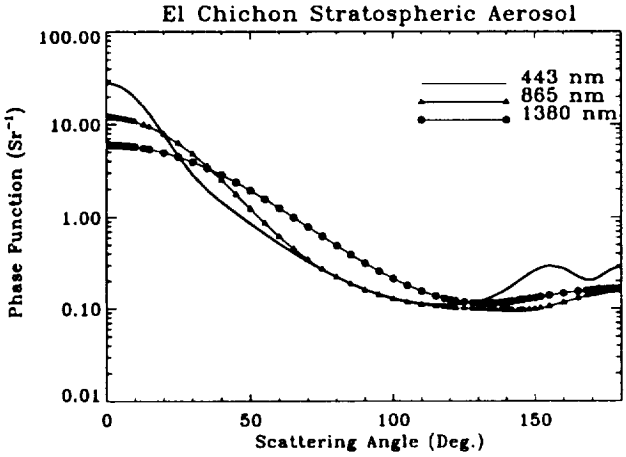

Figure 1c.

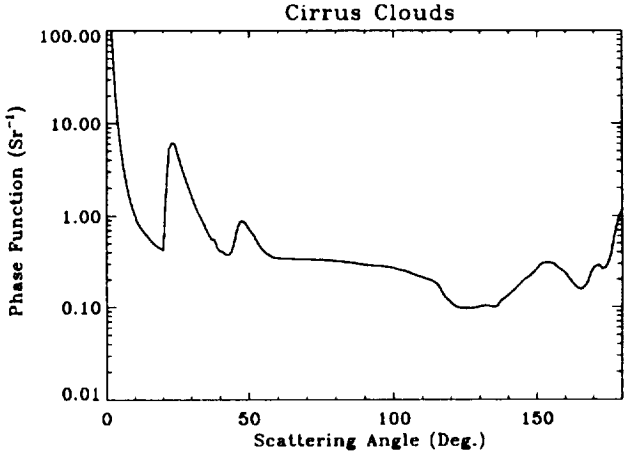

Figure 1d.

Figure 1. Phase functions for the various stratospheric aerosol models used in the study: (a) background; (b) aged volcanic; (c) El Chichon; and (d) thin cirrus clouds.

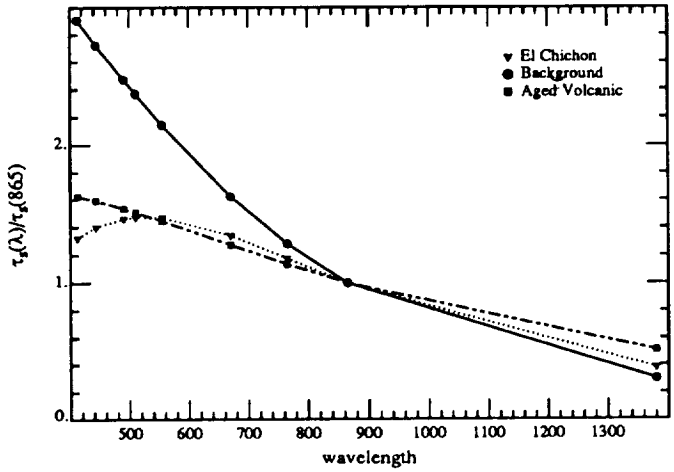

Figure 2. Spectral variation of τ_s for the various stratospheric aerosol models. The Cirrus cloud model is omitted because $\tau_s(\lambda)$ is constant.

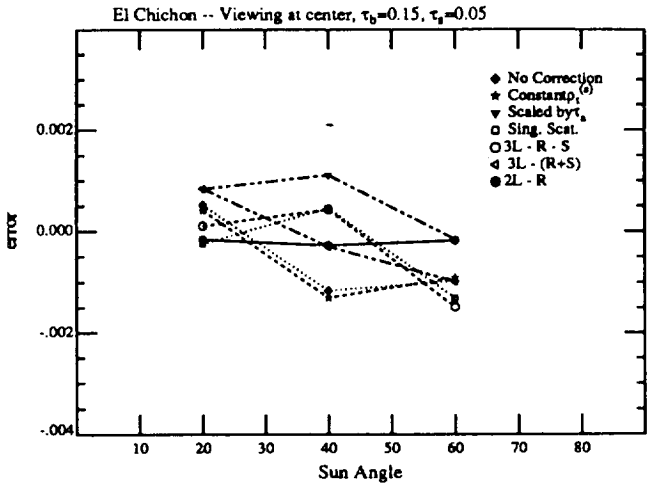

Figure 3a

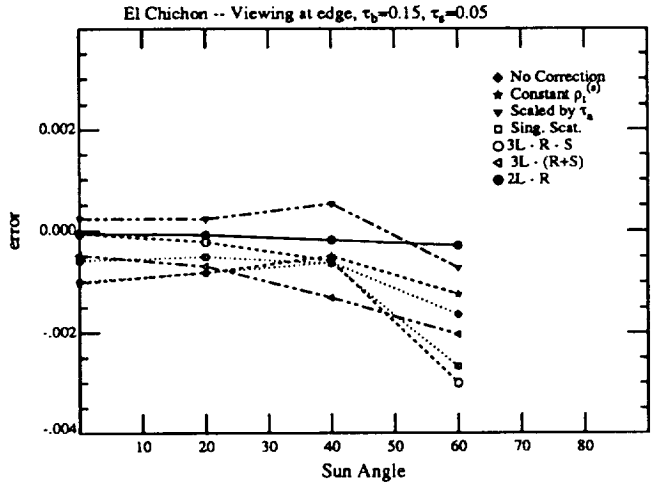

Figure 3b

Figure 3. Error in retrieved water-leaving reflectance as a function of the solar zenith angle for several methods of dealing with the El Chichon stratospheric aerosol (1–6) with $\tau_{bl} = 0.15$ and $\tau_{sl} = 0.05$: (a) scan center; (b) scan edge.

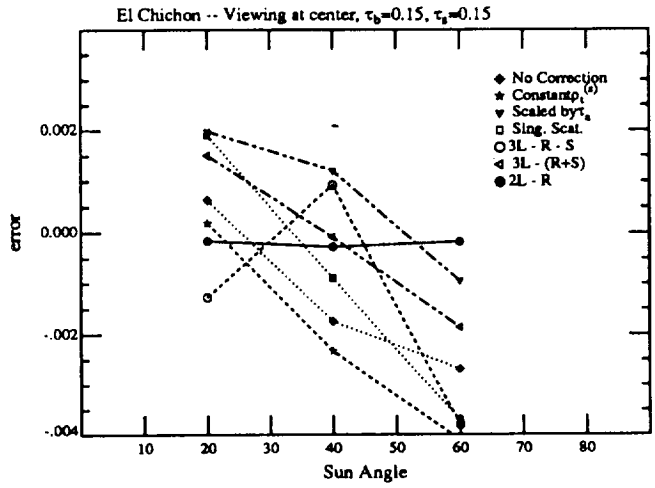

Figure 4a

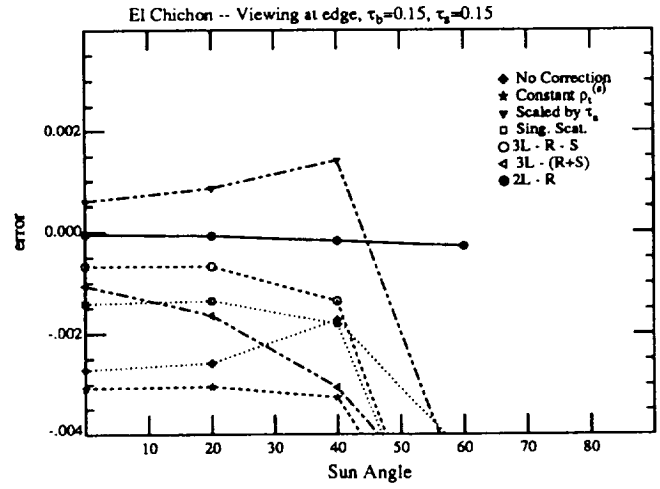

Figure 4b

Figure 4. Error in retrieved water-leaving reflectance as a function of the solar zenith angle for several methods of dealing with the El Chichon stratospheric aerosol (1–6) with $\tau_{bl} = 0.15$ and $\tau_{st} = 0.15$: (a) scan center; (b) scan edge.

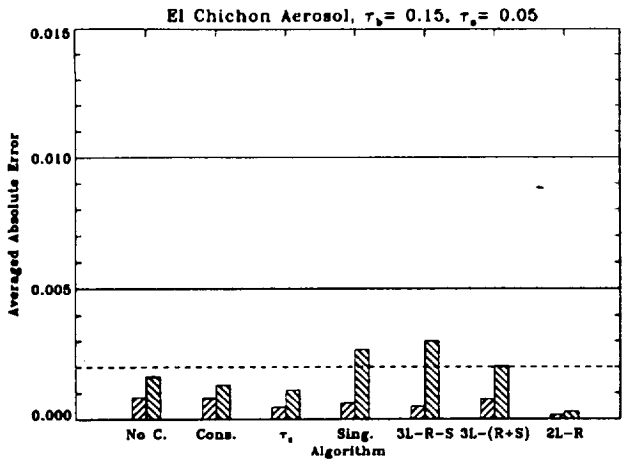

Figure 5a.

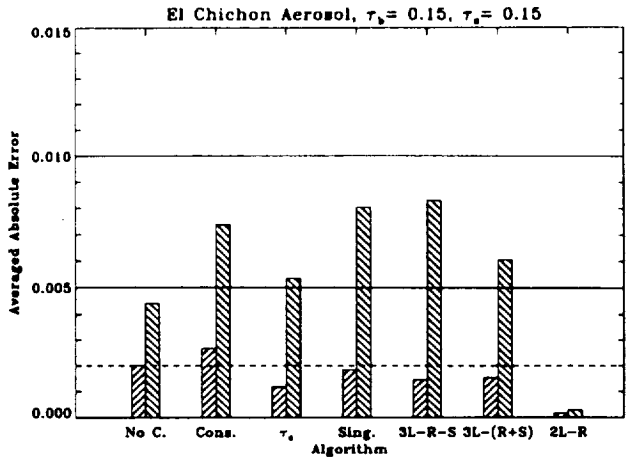

Figure 5b.

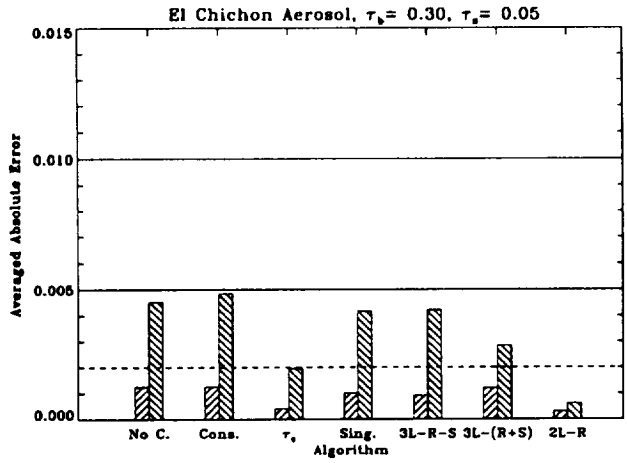

Figure 5c.

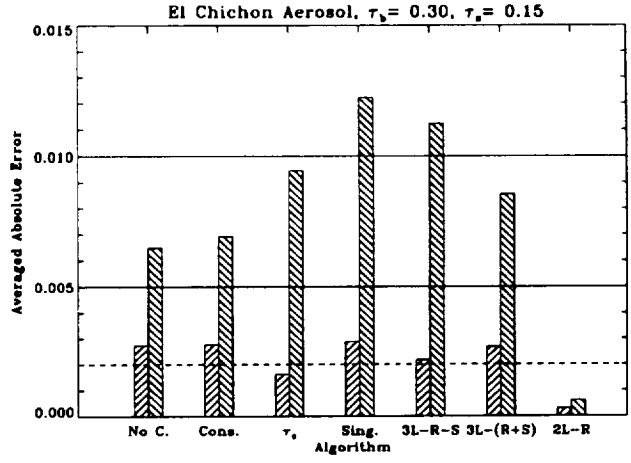

Figure 5d.

Figure 5. Histogram of the average $|\Delta t\rho_w(443)|$ (short bars) and the maximum $|\Delta t\rho_w(443)|$ (tall bars) for the El Chichon stratospheric aerosol for various combinations of τ_b and τ_s: (a) $\tau_b(865) = 0.15$, $\tau_s(865) = 0.05$; (b) $\tau_b(865) = 0.15$, $\tau_s(865) = 0.15$; (c) $\tau_b(865) = 0.30$, $\tau_s(865) = 0.05$; and (d) $\tau_b(865) = 0.30$, $\tau_s(865) = 0.15$.

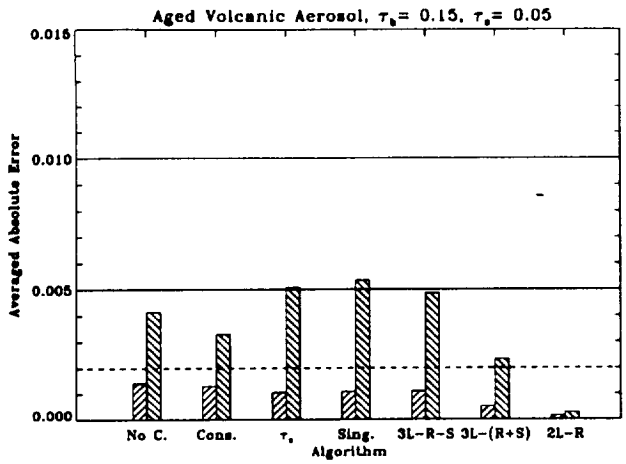

Figure 6a.

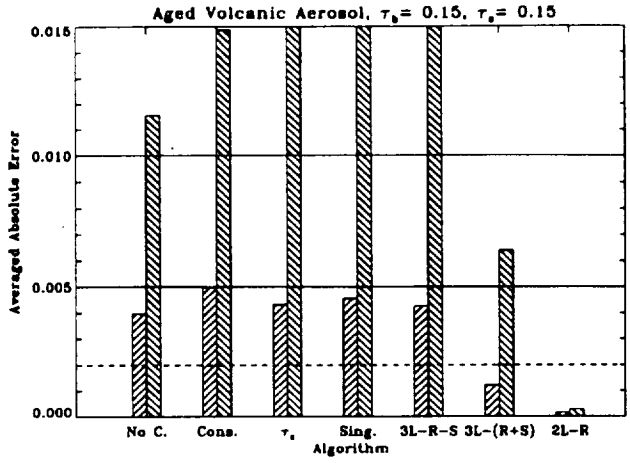

Figure 6b.

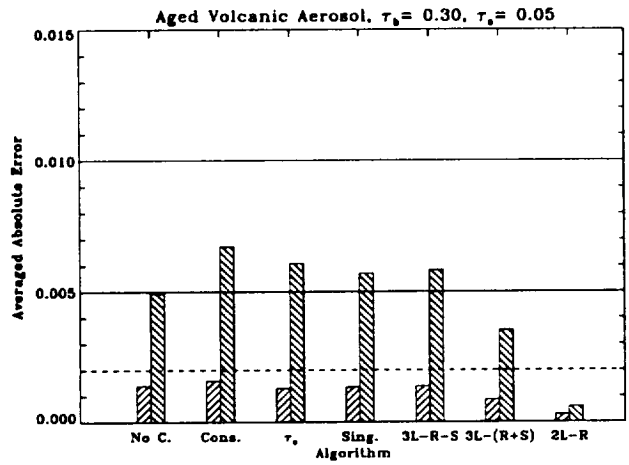

Figure 6c.

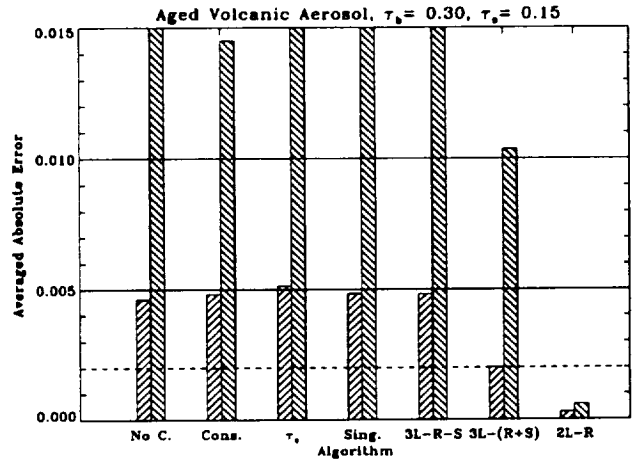

Figure 6d.

Figure 6. Histogram of the average $|\Delta t\rho_w(443)|$ (short bars) and the maximum $|\Delta t\rho_w(443)|$ (tall bars) for the aged volcanic stratospheric aerosol for various combinations of τ_b and τ_s: (a) $\tau_b(865) = 0.15$, $\tau_s(865) = 0.05$; (b) $\tau_b(865) = 0.15$, $\tau_s(865) = 0.15$; (c) $\tau_b(865) = 0.30$, $\tau_s(865) = 0.05$; and (d) $\tau_b(865) = 0.30$, $\tau_s(865) = 0.15$.

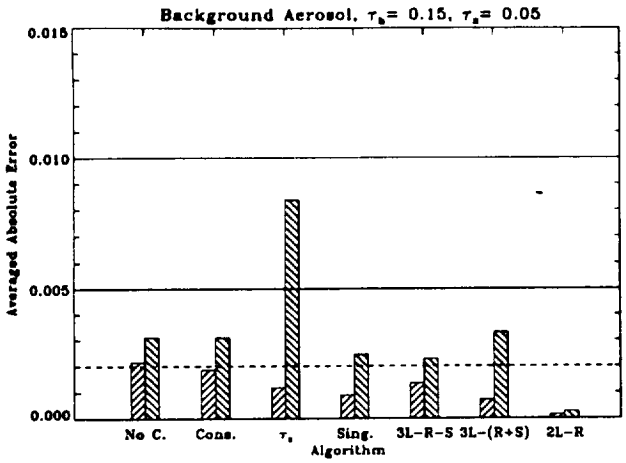

Figure 7a.

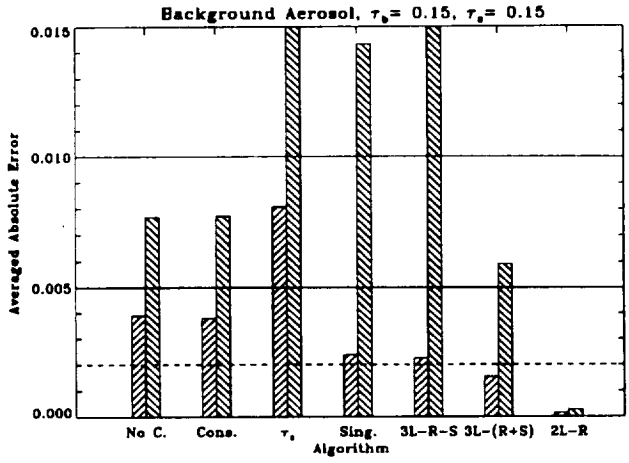

Figure 7b.

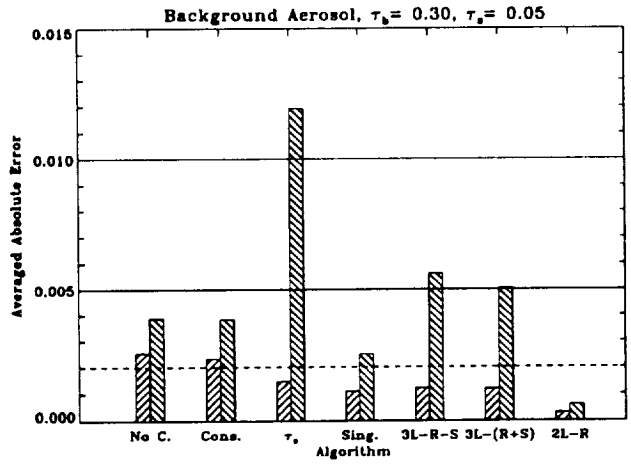

Figure 7c.

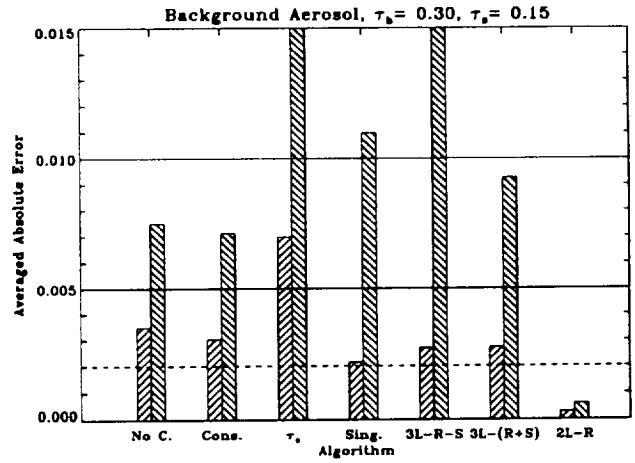

Figure 7d.

Figure 7. Histogram of the average $|\Delta t\rho_w(443)|$ (short bars) and the maximum $|\Delta t\rho_w(443)|$ (tall bars) for the background stratospheric aerosol for various combinations of τ_b and τ_s: (a) $\tau_b(865) = 0.15$, $\tau_s(865) = 0.05$; (b) $\tau_b(865) = 0.15$, $\tau_s(865) = 0.15$; (c) $\tau_b(865) = 0.30$, $\tau_s(865) = 0.05$; and (d) $\tau_b(865) = 0.30$, $\tau_s(865) = 0.15$.

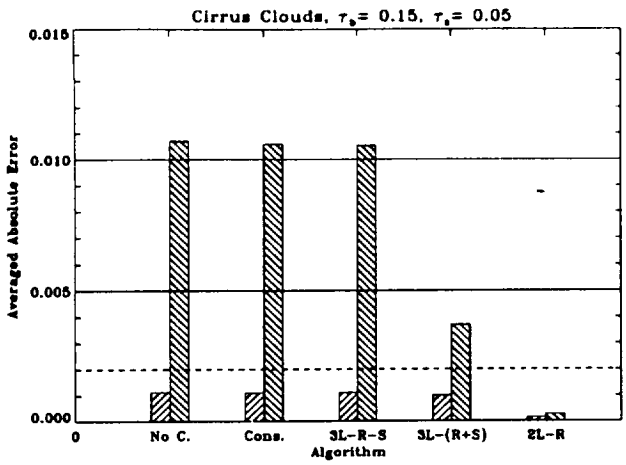

Figure 8a.

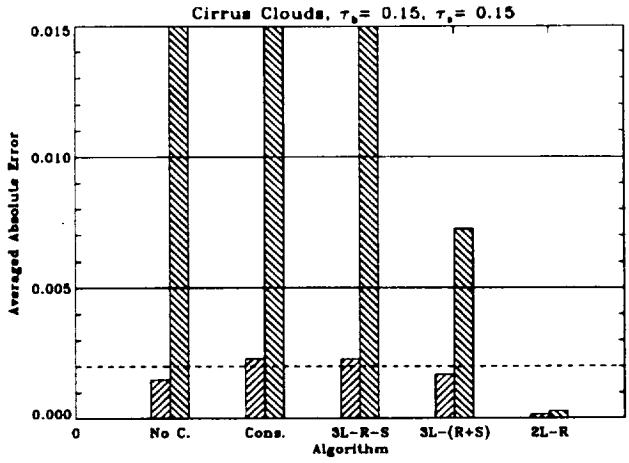

Figure 8b.

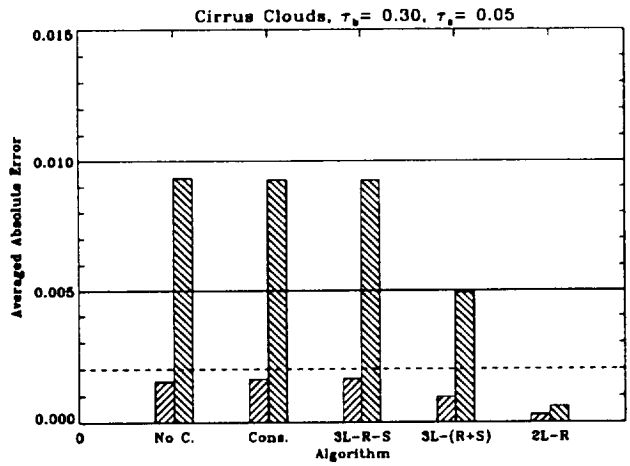

Figure 8c.

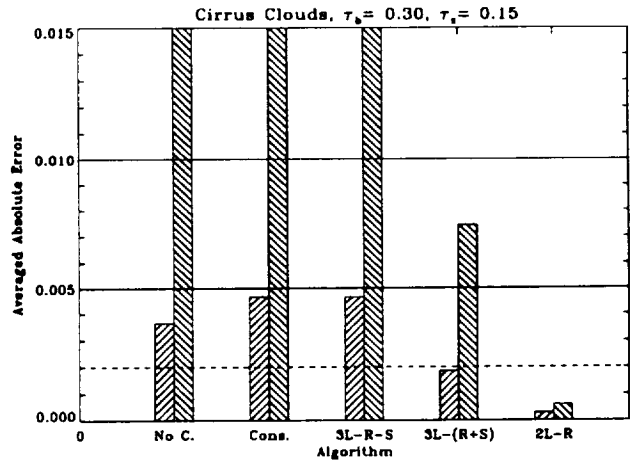

Figure 8d.

Figure 8. Histogram of the average $|\Delta t\rho_w(443)|$ (short bars) and the maximum $|\Delta t\rho_w(443)|$ (tall bars) for the cirrus clouds for various combinations of τ_b and τ_s: (a) $\tau_b(865) = 0.15$, $\tau_s(865) = 0.05$; (b) $\tau_b(865) = 0.15$, $\tau_s(865) = 0.15$; (c) $\tau_b(865) = 0.30$, $\tau_s(865) = 0.05$; and (d) $\tau_b(865) = 0.30$, $\tau_s(865) = 0.15$.

Appendix 2

Columnar Aerosol Properties Over Oceans by Combining Surface and Aircraft Measurements: Simulations

by

Howard R. Gordon and Tianming Zhang

(Accepted for publication in *Applied Optics*)

Acknowledgement

We are grateful to the National Aeronautics and Space Administration for support under Grant NAGW-273 and Contracts NAS5-31363 and NAS5-31743 and the Office of Naval Research under Grant Number N00014-89-J-1985.

Abstract

We report an algorithm that can be used to invert the radiance exiting the top and bottom of the atmosphere to yield the columnar optical properties of the atmospheric aerosol under clear sky conditions over the oceans. The method is an augmentation of a similar algorithm presented by Wang and Gordon [*Appl. Opt.*, **32**, 4598–4609 (1993)] that only utilized sky radiance, and therefore, was incapable of retrieving the aerosol phase function at the large scattering angles that are of critical importance in remote sensing oceanic and atmospheric properties with satellites. Well known aerosol models were combined with radiative transfer theory to simulate pseudodata for testing the algorithm. The tests suggest that it should be possible to retrieve the aerosol phase function and the aerosol single scattering albedo accurately over the visible spectrum at aerosol optical thicknesses as large as 2.0. The algorithm is capable of retrievals with such large optical thicknesses because all significant orders of multiple scattering are included. We believe that combining an algorithm of this type with surface-based and high altitude aircraft-based radiance measurements could be useful for studying aerosol columnar optical properties over oceans and large lakes. The retrieval method is possible over the oceans because, unlike the land surface, its albedo is low and spatially uniform.

1. Introduction

In a recent paper, Wang and Gordon[1] reported an algorithm for retrieval of the aerosol phase function, $P(\Theta)$, where Θ is the scattering angle, and the aerosol single scattering albedo, ω_0, from measurements of the aerosol optical thickness, τ_a, and the normalized sky radiance, $\rho_t(\hat{\xi}_i)$, where $\hat{\xi}_i$ is a unit vector corresponding to the i^{th} direction in which the measured radiance is propagating, over the oceans. The normalized radiance ρ corresponding to the actual radiance L (mW/cm^2 μm Sr) is defined by $\pi L/F_0 \cos\theta_0$, where θ_0 is the solar zenith angle and F_0 is the extraterrestrial solar irradiance (mW/cm^2 μm). The retrieval algorithm, an extension of earlier work by King,[2] Box and Deepak,[3,4] Nakajima et al.,[5] and Wendisch and von Hoynunegn-Huene,[6] included all significant orders of multiple scattering and, therefore, was not limited to small values of τ_a. The retrieval method is possible over the oceans because, unlike the land surface, its albedo is low and nearly spatially uniform.

The basic idea of the algorithm is to find aerosol properties that, when inserted into the radiative transfer equation (RTE), yield the measured values of $\rho_t(\hat{\xi})$. Briefly, from initial guesses for ω_0 and $P(\Theta)$, the RTE was solved using the given (measured) value of τ_a to find the predicted sky radiance. The differences $\Delta\rho(\hat{\xi}_i)$ between the predicted and measured sky radiances were then used to provide a new phase function and ω_0. This was accomplished using the single scattering approximation in the following manner. First, the scattering angle Θ_i that would be appropriate to the single scattering of incident solar radiation in the direction $\hat{\xi}_i$ is determined for each point at which the sky radiance is measured, i.e., each $\hat{\xi}_i$. Then the error in the computed sky radiance is used to estimate the error $\Delta[\omega_0 P(\Theta_i)]$ in the trial value of $\omega_0 P(\Theta_i)$ using the appropriate single scattering formulas. The value of $\omega_0 P(\Theta_i)$ is then changed by a fraction (usually 0.5) of $\Delta[\omega_0 P(\Theta_i)]$ yielding a revised value. The revised $\omega_0 P(\Theta_i)$ is then inserted into the RTE and new values of $\rho_t(\hat{\xi}_i)$ are computed. Finally, the process is repeated until the measured and computed $\rho_t(\hat{\xi}_i)$ are in agreement within the experimental error. Using simulated pseudodata, Wang and Gordon[1] found that the rms error between the measured and computed $\rho_t(\hat{\xi}_i)$'s could usually be reduced to a fraction of 1%. Clearly, there are scattering angles Θ that are unaccessible with this procedure, i.e., the maximum value of Θ is $\Theta_{max} = \pi/2 + \theta_0$, where θ_0 is the solar zenith angle. Thus, there is

no way to derive $P(\Theta)$ for $\Theta > \Theta_{max}$. For these angles, Wang and Gordon[1] simply made a guess for P, e.g., $P(\Theta) = P(\Theta_{max})$ for $\Theta > \Theta_{max}$. The guess enables derivation of ω_0 from $\omega_0 P(\Theta)$ by integration over solid angle. Through simulations it was found that excellent values of ω_0 and $P(\Theta)$, for $\Theta < \Theta_{max}$, could be retrieved using these ideas. Note that this approach provides a full multiple scattering inversion of the sky radiance; the single scattering formulas are used *only* to provide the direction (increase or decrease), and a coarse estimate of the amount, that $\omega_0 P(\Theta)$ should be changed at each step of the iteration.

One goal in developing this algorithm was to provide a means of supplying aerosol optical properties for vicarious calibration of spaceborne sensors viewing the ocean in the visible and near infrared regions of the spectrum.[7-10] However, the fact that $P(\Theta)$ cannot be determined for $\Theta > \pi/2 + \theta_0$, a range of angles of critical importance in deriving the expected radiance at the sensor, limits the utility of the method for this application. Thus, we have examined the possibility of combining surface and aircraft data to determine remotely the columnar phase function over the full angular range. In this note, we report that such a combination has the potential for providing excellent retrievals of $P(\Theta)$ and ω_0. In a later paper, we will provide a full sensitivity analysis to determine the limitations of the method.

2. Inversion algorithm

The algorithm for combining the surface and aircraft radiance distributions is similar to that developed by Wang and Gordon[1] with three differences. First, the complex initial guess procedure for $P(\Theta)$ and ω_0 they described was replaced by the assumption of a two-term Henyey-Greenstein phase function with $\omega_0 = 1$, as it was found that the initial guesses for these quantities was not critical. Second, in the case of the TOA radiances, the contribution from Rayleigh scattering does not have to propagate through the aerosol layer, so Eqs. (5), (8), and (9) of Ref. 1 were modified by removing the exponential factor. Finally, spline interpolation on $\log[\omega_0 P(\Theta)]$ was used to provide $\omega_0 P(\Theta)$ between the retrieved values, and $\omega_0 P(\Theta)$ was extrapolated to $\Theta = 0$ by fitting $\log[\omega_0 P(\Theta)]$ for the four smallest values of Θ to a quadratic function in Θ using least squares.

3. Simulated Inversions

To test the algorithm, we have used the Shettle and Fenn[11] Maritime aerosol model with a relative humidity (RH) of 99% and their Urban model with RH = 0. The Maritime model is the more demanding test, as the phase function is more strongly peaked in the forward direction and shows significant variability near the rainbow angle ($\sim 140°$). The Urban model on the other hand has strong absorption ($\omega_0 \sim 0.6$) and provides a test of the algorithm's ability to retrieve ω_0 in such cases. The radiance, exiting the top of the atmosphere (TOA) and incident on the sea surface, was computed using a two-layer successive order of scattering radiative transfer code[1] with the aerosols in the lower layer and the molecular scattering component in the upper layer. This should be a good approximation to the vertical structure of the atmosphere over the oceans in situations in which the aerosol is locally generated and confined to the marine boundary layer. The surface radiance in the solar almucantar and principal plane, and the TOA radiance in the principal plane, computed in this manner, were used as pseudodata to test the retrieval algorithm. It is important to note, that in the radiative transfer code used in the inversion iteration procedure, the assumed vertical structure of the aerosol is the same as for that used in the generation of the pseudodata, i.e., the correct vertical structure, as might be determined from lidar measurements, was used in the retrieval algorithm.

In applying the algorithm to the pseudodata, we found it was very important not to include both surface and TOA radiances with similar values of Θ_i, which we call redundant data. The reason for this is that the multiple scattering effects in redundant data sets can be significantly different. This slows down convergence of the algorithm. Therefore, the surface almucantar was used for $0 \leq \Theta_i \leq 2\theta_0$, the surface principal plane for $2\theta_0 < \Theta_i < \pi/2 + \theta_0$, and the TOA in the principal plane for $\Theta_i > \pi/2 + \theta_0$. This was similar to the surface data used in Wang and Gordon.[1] Note that no redundant data was utilized. In the tests described below, the pseudodata density used in the retrievals was as follows: (1) in the aureole region of the almucantar the pseudodata were used in 1° increments of azimuth from the sun (ϕ) from $\phi = 1°$ to 15°; (2) in the remainder of the almucantar, the pseudodata were spaced in 5°increments; (3) in the principal plane, the surface pseudodata were used in $\sim 3°$ increments in viewing angle (θ_v, the polar angle associated with $\hat{\xi}_i$)

in enough directions to fill $2\theta_0 < \Theta_i < \pi/2 + \theta_0$ (with $\theta_v < 86°$); and at the TOA in the principal plane the pseudodata were employed in $\sim 7°$ increments in viewing angle in enough directions to fill the region $\Theta_i > \pi/2 + \theta_0$. For $\theta_0 = 60°$, this sampling provided ρ_t at the surface in 63 directions and at the TOA in 7 directions.

Samples of the retrievals for the Maritime aerosol model with $\theta_0 = 60°$ are provided in Figure 1, which compares the retrieved $\omega_0 P(\Theta)$ [circles] and the true $\omega_0 P(\Theta)$ [line] as a function of Θ, and Figure 2 which provides the % error in the retrieved values of $\omega_0 P(\Theta)$. Figures 1a and 2a are for 412 nm, while Figures 1b and 2b are for 865 nm. At 865 nm the contribution to ρ_t from Rayleigh scattering is small because the Rayleigh optical thickness, τ_r, is only ~ 0.015. In contrast, at 412 nm the Rayleigh contribution is significant as $\tau_r \approx 0.32$. Two aerosol optical thicknesses (τ_a) were examined, 0.2 and 2.0, corresponding to a relatively clear and a very turbid atmosphere, respectively.

At 865 nm the algorithm retrieves $\omega_0 P(\Theta)$ and ω_0 were excellent using 60 and 120 iterations for $\tau_a = 0.2$ and 2.0, respectively. The maximum error in $\omega_0 P(\Theta)$ was $\sim 3.5\%$ near the rainbow angle and $\lesssim 1\%$ elsewhere. We computed the average (over i) of the absolute value of the relative difference between $\rho_t^{(c)}$, the radiances computed from the retrieved $\omega_0 P(\Theta)$, and the original (measured) values of ρ_t. By this measure, the error in the radiance using the retrieved $\omega_0 P(\Theta)$ was a small fraction (< 0.1) of 1%.

At 412 nm the retrieval accuracy is also excellent for the smaller τ_a, for which the error in $\omega_0 P(\Theta)$ was usually $\lesssim 1.5\%$; however, for $\tau_a = 2.0$, even with 300 iterations, the retrieval is not as good, particularly in the vicinity of the rainbow angle, where the phase function changes rapidly with Θ (maximum error in $\omega_0 P(\Theta) \lesssim 10\%$). Multiple scattering smooths the rapid variations in radiance with $\hat{\xi}_i$ that are observed near the single scattering limit, and this reduces the efficacy of the algorithm near the rainbow angle. Somewhat better retrievals were obtained through the rainbow region in this case by substituting TOA psuedodata in place of the surface principal plane pseudodata. Presumably this occurs because the TOA radiances corresponding to scattering angles from $\Theta = 120°$ to $150°$ for $\theta_0 = 60°$ are less influenced by multiple scattering than the principal

plane radiances. The retrieved values of ω_0 for the results presented in Figure 1 (both wavelengths) were all excellent, the error being $\lesssim 0.1\%$.

In the case of the Urban model, for which the phase function has no rainbow feature and is not as sharply peaked in the forward direction, the retrievals were better than those in Figures 1 and 2. Also, the value of ω_0 was retrieved with an error $< 0.1\%$.

Measurment of the radiance in the aureole region of the almucantar with $\phi = 1°$ is difficult; however, Nakajima et al.,[5] have reported aureole measurements down to $\phi = 2°$. Thus, we have performed computations similar to those described above, but with a minimum value of 2° for ϕ in the almucantar rather than 1°. For the Urban model at both 412 and 865 nm and the Maritime model at 865 nm, the results were essentially unchanged from the previous computations for both $\tau_a = 0.2$ and 2.0. However, for the Maritime model at 412 nm, the retrievals of both ω_0 and P were degraded (errors $\sim 10 - 20\%$ in P for $\Theta \gtrsim 100° - 110°$). This appears to be due to the fact that the Maritime model's phase function at 412 nm is so strongly peaked in the forward direction (the most so of all of the models used here), and suggests that in such cases the radiance probably cannot be inverted accurately to provide optical properties without having small-angle radiance data.

4. Concluding remarks

To our knowledge, the results presented here represent the first inversion of the boundary radiances emerging from an optically thick (multiply scattering) medium to obtain its basic optical properties — ω_0 and $P(\Theta)$. We believe that the results demonstrate that the retrieval method holds significant promise for combining aircraft (or satellite) and surface data to study the columnar optical properties of aerosols over oceans or over large lakes. As such, we are performing a complete sensitivity analysis to try to understand the limitations of the method. This analysis includes sensitivity to radiometric calibration errors, variations in aerosol type with altitude, the horizontal spatial variations in aerosol properties, the influence of polarization, aircraft altitude, etc. The results of this study, which is now underway, will be presented in a later paper.

References

[1] M. Wang and H. R. Gordon, "Retrieval of the Columnar Aerosol Phase Function and Single Scattering Albedo from Sky Radiance over the Ocean: Simulations," Applied Optics **32**, 4598–4609 (1993).

[2] M. D. King and B. M. Herman, "Determination of the Ground Albedo and the Index of Absorption of Atmospheric Particulates by Remote Sensing. Part I: Theory," Jour. Atmos. Sci. **36**, 163–173 (1979).

[3] M. A. Box and A. Deepak, "Retrieval of Aerosol Size Distributions by Inversion of Simulated Aureole Data in the Presence of Multiple Scattering," Applied Optics **18**, 1376–1382 (1979).

[4] M. A. Box and A. Deepak, "An Approximation to Multiple Scattering in the Earth's Atmosphere: Almucantar Radiance Formulation," Jour. Atmos. Sci. **38**, 1037–1048 (1981).

[5] T. Nakajima, M. Tanaka and T. Yamauchi, "Retrieval of the Optical Properties of Aerosols from Aureole and Extinction Data," Applied Optics **22**, 2951–2959 (1983).

[6] M. Wendisch and W. von Hoyningen-Huene, "High Speed Version of the Method of 'Successive Order of Scattering' and its Application to Remote Sensing," Beitr. Phys. Atmosph. **64**, 83–91 (1991).

[7] P. Koepke, "Vicarious Satellite Calibration in the Solar Spectral Range by Means of Calculated Radiances and its Application to Meteosat," Applied Optics **21**, 2845–2854 (1982).

[8] H. R. Gordon, J. W. Brown, O. B. Brown, R. H. Evans and D. K. Clark, "Nimbus 7 Coastal Zone Color Scanner: reduction of its radiometric sensitivity with time," Applied Optics **22**, 3929–3931 (1983).

[9] R. S. Fraser and Y. J. Kaufman, "Calibration of satellite sensors after launch," Applied Optics **25**, 1177–1185 (1986).

[10] P. N. Slater, S. F. Biggar, R. G. Holm, R. D. Jackson, Y. Mao, M. S. Moran, J. M. Palmer and B. Yuan, "Reflectance- and Radiance-Based Methods for the In-Flight Absolute Calibration of Multispectral Sensors," Remote Sensing of Environment **22**, 11–37 (1987).

[11] E. P. Shettle and R. W. Fenn, *Models for the Aerosols of the Lower Atmosphere and the Effects of Humidity Variations on Their Optical Properties* (Air Force Geophysics Laboratory, Hanscomb AFB, MA 01731, AFGL–TR–79-0214, 1979).

Figure Captions

Figure 1. Comparison between the true $\omega_0 P(\Theta)$ (solid line) and the retrieved $\omega_0 P(\Theta)$ (circles) for the Maritime aerosol model with RH = 99% and $\theta_0 = 60°$: (a) 412 nm; (b) 865 nm. Lower curves are for $\tau_a = 0.2$, upper curves for $\tau_a = 2.0$. Values for $\tau_a = 2.0$ are $\times 10$.

Figure 2. % Error in $\omega_0 P(\Theta)$ for $\tau_a = 0.2$ (dashed line) and $\tau_a = 2.0$ (solid line): (a) 412 nm; (b) 865 nm.

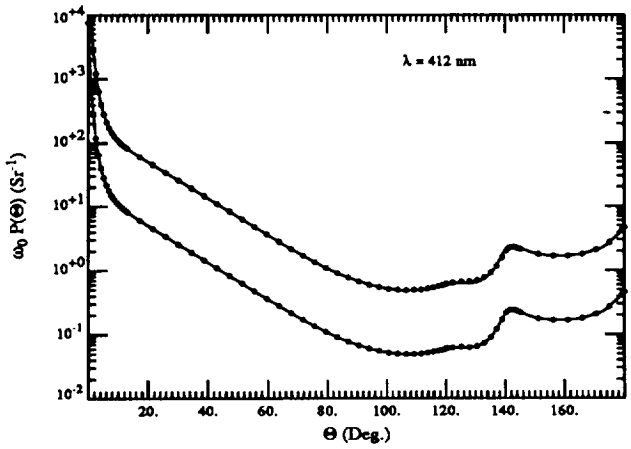

Figure 1a.

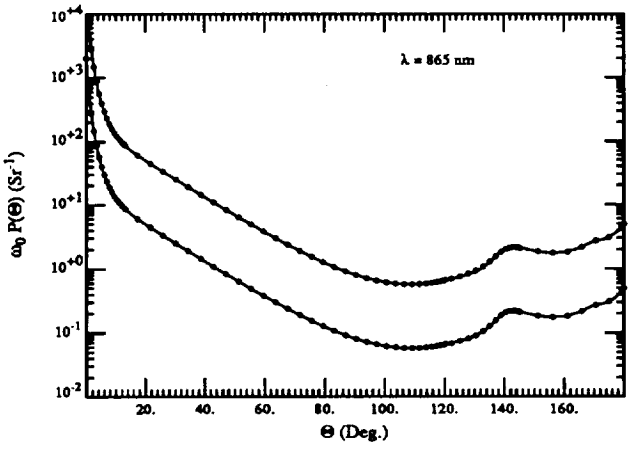

Figure 1b.

Figure 1. Comparison between the true $\omega_0 P(\Theta)$ (solid line) and the retrieved $\omega_0 P(\Theta)$ (circles) for the Maritime aerosol model with RH = 99% and $\theta_0 = 60°$: (a) 412 nm; (b) 865 nm. Lower curves are for $\tau_a = 0.2$, upper curves for $\tau_a = 2.0$. Values for $\tau_a = 2.0$ are $\times 10$.

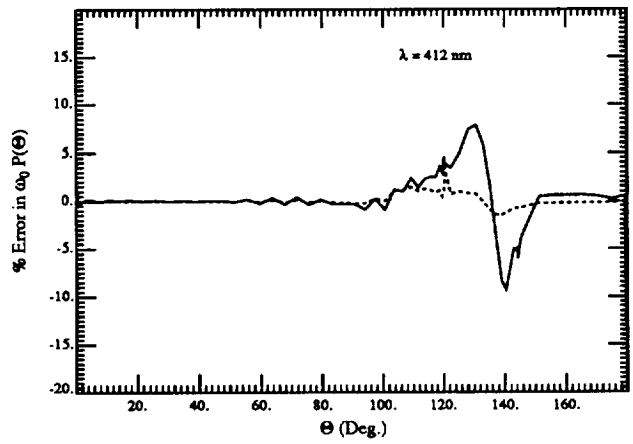

Figure 2a.

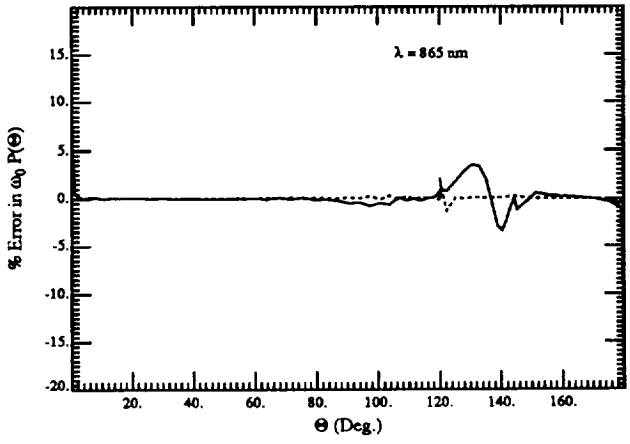

Figure 2b.

Figure 2. % Error in $\omega_0 P(\Theta)$ for $\tau_a = 0.2$ (dashed line) and $\tau_a = 2.0$ (solid line): (a) 412 nm; (b) 865 nm.

Appendix 3

Island perturbation to the sky radiance over the ocean: Simulations

by

Haoyu Yang, Howard R. Gordon, and Tianming Zhang

The authors are with the Department of Physics, University of Miami, Coral Gables, FL 33124.

(Submitted to *Applied Optics*)

Acknowledgement

We are grateful to the National Aeronautics and Space Administration for support under Grant NAGW-273 and Contracts NAS5-31363 and NAS5-31743, and the Office of Naval Research under Grant Number N00014-89-J-1985.

Abstract

We demonstrate, through Monte Carlo simulations, that significant perturbations to sky radiance measurements over the ocean can occur when measurements are carried out using radiometers located on islands. In particular, we present examples of the influence of the physical and optical thicknesses of an aerosol layer, the azimuth of observation relative to the sun, the size of the island, the location of the radiometer on the island, and the albedo of the island, on the magnitude of the perturbation for a circular island of uniform albedo. Relative errors in sky radiance of as high as 39% were found in the blue. Simulated (perturbed) sky radiances were combined with an algorithm for retrieving the aerosol phase function $P(\Theta)$, where Θ is the scattering angle, and single scattering albedo ω_0, to demonstrate how the perturbation can influence their retrieved values. It was found that the fractional error in the retrieved values of the product $\omega_0 P(\Theta)$ can be significantly greater than that in the sky radiance, because of the effects of multiple scattering. This underscores the importance of removing the island perturbation prior to employing an inversion algorithm. Fortunately, the relative sky radiance perturbation is a weak function of $P(\Theta)$, so a correction is feasible.

1. Introduction

There is a need to understand the columnar properties of aerosols over the ocean (a) for atmospheric correction[1] of ocean color sensors, e.g., the Sea-viewing wide-field-of-view sensor (SeaWiFS),[2] and (b) for aiding retrieval of aerosol properties over the ocean from similar instruments.[1,3] Wang and Gordon[4] have presented a method for retrieving the aerosol columnar phase function and single scattering albedo from measurements of the aerosol optical thickness and sky radiance over the ocean, through iteratively solving the radiative transfer equation (RTE) until the measured and predicted (based on the aerosol phase function and single scattering albedo) sky radiance agree within experimental error. Their method was an extension of earlier work by King,[5] Box and Deepak,[6,7] Nakajima et al.,[8] and Wendisch and von Hoynunegn-Huene,[9] and basically works because the surface albedo of the ocean is low and known. The ideal platform for such measurements is a ship; however, for a variety of reasons, e.g., cost and the simplicity of a stable platform, it is more convenient of locate instruments on islands. Unfortunately, even a small island will perturb the light field in its vicinity if its albedo is significantly different from that of the ocean. It is important to have an understanding of the extent of such perturbations to determine the suitability of potential station locations and, perhaps, to provide a first-order correction for the effect. In this paper we present the results of simulations aimed at providing an assessment of the possible extent of the perturbation.

We begin by describing the Monte Carlo simulation techniques we developed for this problem in the special case that the island is a circular disk. Then we operate the simulation code to provide examples of the sky radiance perturbation as a function of the size of the island, the optical thickness of the aerosol, the physical thickness of the aerosol layer, the position of the sensor on the island, and the albedo of the island. Finally, we apply the aerosol retrieval technique of Wang and Gordon[4] to simulated measurements and show how the island perturbation influences the retrieval of the phase function. In an appendix we provide an alternate Monte Carlo approach that is applicable to an island of any shape. A code based on this approach could be used to provide a first-order correction to the perturbation.

2. Computational Procedure

The distribution and propagation of light field in the atmosphere is goverened by the radiative transfer equation (RTE). There are several ways to solve the equation for a plane parallel atmosphere where the light field is invariant to translation in all directions parallel to the boundaries. However, in the presence of a perturbation that destroys this invariance (the island), the Backward Monte Carlo (BMC) method is the most straightforward. In the BMC procedure, the photon paths are simulated from the detector to the source. The procedure begins with the emission of a photon from the detector in a direction exactly opposite to the direction in which the radiance is desired. The distance the photon travels before interacting in the medium is determined from random sampling based on the beam attenuation coefficient of the medium. Upon scattering, the new direction the photon travels is generated by sampling the scattering phase function. When the photon is scattered, however, it may strike the surface of the sea or the surface of the island. In the former case the direction of the photon is determined from Fresnel's laws of reflection, while in the latter case the new direction is sampled from the bidirectional reflection distribution function (BRDF) of the island. At each interaction with the medium, the possibility that the photon will be scattered in a direction which would allow it to propagate to the sun, either directly, or by reflection from the sea surface or the island, is computed and collected.

Figure 1 describes the geometry of the RTE problem. The atmosphere is assumed to be composed of two layers, with aerosol scattering confined to the lower layer and molecular scattering to the upper layer. The lower boundary of the medium is the ocean. The island is assumed to be circular in shape (radius R) and to be a lambertian reflector. The radiometer is placed anywhere on the island. The z-axis is normal to the sea surface and is directed upward from the center of the island. The x-axis is the projection of the solar beam on the sea surface. The y-axis is determined by the right-hand-rule.

There are three paths the photon can take toward the sun at each interaction in the atmosphere: (1) the photon can be scattered in a direction toward the sun; (2) it can be scattered toward the sea surface and Fresnel-reflected toward the sun; or (3) it can be scattered toward the island and be diffusely reflected by the island in a direction toward the sun. In each case the Monte Carlo

estimator is related to the probability that the photon will exit the atmosphere toward the sun. At the n^{th} interaction for a given photon, the contribution to the radiance from the first path, L_1 is simply

$$L_1 = \omega_0^n P(\Theta_1) T(\text{interaction} \rightarrow \text{sun}) \tag{1}$$

where ω_0 and $P(\Theta)$ are the single scattering albedo and scattering phase function of the atmosphere (for a scattering angle Θ) at the interaction point, Θ_1 is the angle between the direction of propagation of the photon from the previous interaction point and a vector from the present interaction point to the sun, and $T(\text{interaction} \rightarrow \text{sun})$ is the atmospheric transmittance of the atmosphere from the interaction point to the top of the atmosphere in the direction of the sun. Likewise, the contribution to the radiance from path 2, L_2, is

$$L_2 = \omega_0^n P(\Theta_2) T(\text{interaction} \rightarrow \text{surface} \rightarrow \text{sun}) R_f, \tag{2}$$

where Θ_2 is the angle between the direction of propagation of the photon from the previous interaction point and a vector from the present interaction to the sea surface in such a direction that, if followed by a photon, it would be Fresnel-reflected in a direction toward the sun. $T(\text{interaction} \rightarrow \text{surface} \rightarrow \text{sun})$ is the transmittance of the atmosphere from the present interaction point to the sea surface and then from the sea surface to the top of the atmosphere in a direction toward the sun. R_f is the Fresnel reflectivity of the air-sea interface. R_f is set to zero if the path — interaction $\rightarrow$ surface — intersects the island, i.e., $L_2 = 0$ if the island prevents specular reflection from the surface in the direction of the sun.

The contribution from the third process — scattering toward the island followed by diffuse reflection from the island toward the sun — is more complex. This is because at each interaction the contribution, L_3, to the radiance is an integral over all possible paths that the photon can take toward the island and then be scattered by the island toward the sun. It is given by

$$L_3 = \omega_0^n \int P(\hat{\xi}'' \rightarrow \hat{\xi}') P_I(\hat{\xi}' \rightarrow \hat{\xi}_0) T(\hat{\xi}') T(\hat{\xi}_0)\, d\Omega(\hat{\xi}'),$$

where $\hat{\xi}''$ is a unit vector from collision $n-1$ to collision n, $\hat{\xi}'$ is a unit vector from collision n to a point on the island (Figure 1), and $\hat{\xi}_0$ is a unit vector from a point on the island in a direction

toward the sun, $T(\hat{\xi}')$ is the atmospheric transmittance from collision n to the island in the direction $\hat{\xi}'$, and $T(\hat{\xi}_0)$ is the atmospheric transmittance from the island to the sun. $d\Omega(\hat{\xi}')$ is a differential in solid angle around the direction $\hat{\xi}'$, and $P_I(\hat{\xi}' \rightarrow \hat{\xi}_0)$ is the probability that radiance propagating in the direction $\hat{\xi}'$ will be scattered by the island in the direction $\hat{\xi}_0$. Since the island is lambertian,

$$P_I(\hat{\xi}' \rightarrow \hat{\xi}_0) = \frac{A}{2\pi} \cos\theta_0,$$

where A is the albedo of the island and θ_0 is the solar zenith angle. Thus,

$$L_3 = \frac{A}{2\pi} \cos\theta_0 T(\hat{\xi}_0) \omega_0^n \int P(\hat{\xi}'' \rightarrow \hat{\xi}') T(\hat{\xi}')\, d\Omega(\hat{\xi}'). \tag{3}$$

Note that this is actually a double integral and that it must be evaluated at each collision. Thus, the key to including the island effects in the radiative transfer process is the evaluation of Eq. (3) at each collision. A simple possibility for evaluating the integral is to replace it by a Monte Carlo estimate, i.e., if $\hat{\xi}'$ is chosen from a uniform distribution of directions within Ω', the solid angle subtended by the island at the collision point, then

$$\lim_{N\rightarrow\infty} \frac{1}{N} \sum_{i=1}^{N} P(\hat{\xi}'' \rightarrow \hat{\xi}_i') T(\hat{\xi}_i') = \int P(\hat{\xi}'' \rightarrow \hat{\xi}') T(\hat{\xi}')\, d\Omega(\hat{\xi}'), \tag{4}$$

where the index i refers to one of the N individual samples of $\hat{\xi}'$. However, we still need to compute the solid angle Ω' (Figure 1) in order to normalize the uniform probability density used to compute $\hat{\xi}'$. This is also a double integral. Fortunately, it can be determined directly as a sum of elliptic integrals when the island is circular in shape; however, in the general case the evaluation of Ω' cannot be carried out analytically.

It is possible to avoid evaluation of Ω' by replacing $d\Omega(\hat{\xi}')$ by $|\hat{\xi}' \bullet \hat{n}'| dA(\hat{\xi}')/r'^2$, where dA is the island area subtended by the solid angle $d\Omega(\hat{\xi}')$, r' is the distance from the interaction point to dA, i.e., $\sqrt{(x-x')^2 + (y-y')^2 + z^2}$, and $\hat{n}'$ is the unit normal to the island surface at the position of dA. Now, the point $(x', y', 0)$ on the island is chosen from a uniform distribution in area, and the estimator becomes

$$\lim_{N\rightarrow\infty} \frac{1}{N} \sum_{i=1}^{N} \frac{|\hat{\xi}' \bullet \hat{n}'|}{r'^2} P(\hat{\xi}'' \rightarrow \hat{\xi}_i') T(\hat{\xi}_i') = \int P(\hat{\xi}'' \rightarrow \hat{\xi}') T(\hat{\xi}')\, d\Omega(\hat{\xi}'). \tag{5}$$

Thus, the price of avoiding the computation of Ω' is the introduction of a singularity in this portion of the estimator for L_3. Clearly, photons that interact with the atmosphere close to the island will make a large contribution to L_3, which will increase the variance of the estimate. The obvious method of coping with the singularity is to use Eq. (4) for photons close to the island, and Eq. (5) elsewhere. In our Monte Carlo code, satisfactory results are obtained if Eq. (5) is used whenever the interaction point (x, y, z) is at a distance greater than $0.1R$ from any point on the island. Evaluation of the integrals in Eqs. (4) or (5) requires splitting the photon into N components (each with weight $1/N$) at each interaction; however, we found that such splitting did not improve the accuracy of the results appreciably, so the integral in question was evaluated at each interaction with $N = 1$.

3. Atmospheric Models

In our simulations we assume that the atmosphere consists of two homogeneous layers with the aerosols in the lower layer, and the molecular scattering (Rayleigh scattering) in the upper layer. The physical thickness of the lower layer, h is taken to be 1 or 2 km. The optical characteristics of the aerosol were generated from the models provided by Shettle and Fenn.[10] In particular, we used the model size distributions and refractive indices for their Tropospheric model at a relative humidity (RH) of 80% (which we indicate by T80) and the Gordon and Wang[1] Coastal model, which is based on a combination of Shettle and Fenn's Tropospheric and Oceanic models with RH = 80% (designated as C80) to generate the scattering phase functions corresponding to a wavelength of 443 nm. These are provided in Figure 2. For all of our computations the single scattering albedo of the aerosol was taken to be unity.

4. Assessment of the Impact of the Island on sky radiance

In this section we present the results of simulations in which we vary the values of the significant parameters: R — the radius of the island; h — the physical thickness of the aerosol; τ_a — the aerosol optical thickness; ϕ — the azimuth of the viewing direction relative to the sun (solar azimuth is at $\phi = 0$); the position of the sensor on the island; and the aerosol phase function. Unless otherwise

stated, the Rayleigh optical thickness, τ_r, is taken to be 0.25 (wavelength $\sim$ 437 nm), C80 is used as the aerosol model to generate the aerosol phase function, and the albedo (A) of the island is unity.

Since our computations carried out using the Monte Carlo methods and have an inherent statistical error, it is important to understand the accuracy with which they are performed. To effect this, we have carried out one simulation in which 10^7 photons were ejected from the source at $\phi = 90°$ with $\tau_r = \tau_a = 0.25$ and $h = 2$ km. Both the solar zenith angle, θ_0, and the viewing angle, θ_v, were 60°, i.e., viewing was in the almucantar of the sun. The resulting $L_t = L_1 + L_2 + L_3$ was tabulated for each 10^4 photons. The average of L_t, normalized to the extraterrestrial solar irradiance (F_0), was 0.052075 for the 10^7 photons. In this manner, we have 10^3 independent simulations. For each of the 10^3 independent simulations the number of occurrences of L_t were binned in increments of 0.0005, e.g., the number of occurrences of L_t in ranges 0.0500 to 0.0505, 0.0505 to 0.0510, etc. were recorded. Figure 3 provides the resulting histogram of the number of occurrences. For this case, it is seen that the standard deviation of the distribution is $\sim$ 0.0016, or the statistical error in L_t when 10^4 photons are released from the detector is $\sim$ 3%. In most of our simulations, between 10^6 and 10^7 photons are processed, so the relative error in the this case would be $\sim$ 0.3 to 0.1%. In the light of Figure 3, the statistical error in the magnitude of L_t is expected to be well below the perturbation in the magnitude of L_t caused by the presence of the island (see Figure 4b in particular where the perturbation in L_t was $\sim$ 25% for this case). Had we employed Eq. (5) at all of the interactions, rather than using Eq. (4) when the interaction was close to the island, the principal difference between the resulting histogram and Figure 3 is the occasional occurrence of a large value of L_t, e.g., $L_t \approx 0.094$ was obtained once in 1000 simulations. In the absence of the island, our BMC code reproduces the radiances computed with a successive order of scattering code[11,12] within 0.1–0.2%. Also, L_t approaches that for a plane parallel atmosphere bounded by a lambertian surface of infinite extent as R becomes large.

The influence of the variation of τ_a and h on the radiance L, normalized to F_0, in the almucantar of the sun ($\theta_v = \theta_0$) with $\theta_0 = 60°$, is presented in Figures 4a, 4b, and 4c corresponding to $\phi = 0$, 90, and 180°, respectively. In this figure the sensor is located at the center of the island, and

symmetry dictates that the additional radiance caused by the presence of the island (L_3) is the same for all viewing directions (this is satisfied in our computations); however, the contribution from specular reflection by the sea surface (L_2) will depend on the viewing angle by virtue of the island's blocking of a portion of the sea surface. Thus, the perturbation caused by the island will have a weak dependence on the viewing azimuth. The computations clearly demonstrate the effect of an increasing radiance measured as the size of the island is increased. As expected, the perturbation is most significant in viewing directions for which the radiance in the absence of the island is small, i.e., directions far from the solar aureole. The perturbation is seen to increase very slowly with τ_a, e.g., for $h = 2$ km and $\phi = 90°$, the relative error in the sky radiance, $\Delta L_t / L_t$, only increases from 18% to 29% as τ_a increases from 0.1 to 0.5. Decreasing the thickness of the aerosol layer, but keeping τ_a fixed, is seen to increase the perturbation, as this increases the probability that an aerosol-scattered photon will interact with the island. Thus, we see that even for a relatively small island, e.g., $R \sim 1$ km, the perturbation of the radiance can reach nearly 10% in some of the examples provided here.

One obvious method of reducing the perturbation is to move the sensor to the edge of the island such that $\phi = 0$ corresponds to the sensor viewing the sun in line with the center of the island. In this manner, measurements at $\phi \geq 90°$ would be carried out looking over open water. Note that in this case the symmetry is broken and the radiance added by the presence of the island (L_3) is no longer independent of ϕ. Figures 5a, 5b, and 5c compare the resulting perturbations computed for $h = 1$ km when this strategy is employed. For $\phi = 180°$ (Figure 5c), there is a significant decrease (as much as 90%) in the island perturbation, while for $\phi = 90°$ (Figure 5b) the decrease is considerably less, i.e., $\sim 50 - 70\%$. For $\phi = 10°$ (Figure 5a) there is essentially no change in the perturbation, and this implies there is a net gain in the accuracy of the measured sky radiance by moving the sensor from the center to the edge of the island.

Figure 6 provides an example of the change in the perturbation when the island albedo is reduced from 1.0 to 0.5. In the example shown, for $R \lesssim 2$ km the perturbation is reduced by $\sim 1/2$, suggesting that for small islands photons usually interact once with the island. In contrast,

for $R = 8$ km the perturbation is reduced to $\sim$ 40% of its original value indicating multiple interactions with the island.

In Figure 7 we provide an example of the influence of the shape of the aerosol phase function on the perturbation of the light field. The figure compares the magnitude of the perturbations when the aerosol phase functions are computed using the C80 and T80 aerosol models (Figure 2), and shows that $\Delta L_t / L_t$ is a weak function of the aerosol phase function. This suggests that a correction for the island perturbation may be possible with only a coarse estimate of the aerosol phase function.

5. Impact on retrieval of aerosol optical properties

In this section, we provide examples of the influence of the island perturbation on the retrieval of aerosol optical properties. For this, we apply the method described by Wang and Gordon[4] for retrieving the columnar aerosol phase function and single scattering albedo from measurements of τ_a and the sky radiance L_t in the solar almucantar and the principal plane. Pseudodata was generated for an island with $R = 5$ km, $A = 1$, and $\theta_0 = 60°$, with the sensor located at the center and at the edge of the island. The aerosol optical properties were taken from the C80 aerosol model (with $\omega_0 = 1$), and the physical and optical thicknesses of the aerosol layer were, respectively, 1 km and 0.25. Figure 8 provides the fractional error in L_t in the solar almucantar induced by the island for both sensor positions. Note the significant improvement obtained for $\phi \gtrsim 90°$ by moving the sensor from the center to the edge of the island. Figure 9 shows the excellent retrieval of the phase function for $\Theta \lesssim 145°$ in the absence of the island. Note that for $\Theta \gtrsim 145°$ the values of $\omega_0 P$ are (exponentially) extrapolated to 180°using the last five points for $\Theta > 120°$. This extrapolation is used to complete the phase function for the iterative retrieval procedure and for estimating the value of ω_0. In this simulation, the retrieved value of ω_0 was 0.984 compared to the correct value of unity. In Figure 10 we show retrievals obtained with the sensor on the island. The strong perturbation by the island manifests in values of $\omega_0 P(\Theta)$ that are too large. In fact, the fractional error in $\omega_0 P(\Theta)$ can be as much as a factor of two for some values of Θ when the sensor is at the center of the island. This causes the retrieved values of ω_0 to even be > 1 (1.04 and 1.12

using the island edge and center pseudodata, respectively). Note that the placing of the sensor at the edge does not completely solve the perturbation problem. There is still significant error for $40° \lesssim \Theta \lesssim 80°$. It should be possible to remove much of this error by using the retrieved phase function to correct L_t for the island's perturbation.

6. Concluding remarks

In this paper we have demonstrated through simulations that significant perturbations to the sky radiance over the ocean can occur when measurements of L_t are carried out using radiometers located on islands. In particular we showed how the physical and optical thicknesses of the aerosol, the azimuth of observation relative to the sun, the size of the island, the location of the radiometer on the island, and the albedo of the island, influence the magnitude of the perturbation, which can reach as much as $\sim 40\%$ or more of the unperturbed radiance. We then combined the simulated (perturbed) sky radiance with an algorithm for retrieving the aerosol phase function and single scattering albedo to demonstrate how the perturbation can influence the retrieved values of $\omega_0 P(\Theta)$. It is interesting to note that the fractional error in the retrieved $\omega_0 P(\Theta)$ can be significantly greater than that in L_t (compare Figure for $\phi \gtrsim 90°$ and Figure 20 for $\Theta \gtrsim 60°$). This effect is due to multiple scattering, and underscores the importance of the removal of the island's perturbation prior to employing an inversion algorithm. Fortunately, the perturbation $\Delta L_t / L_t$ is a weak function of the aerosol phase function, so a correction (perhaps even an iterative procedure with the inversion algorithm) is feasible. In the following appendix we provide a modified Monte Carlo computational procedure with which one can assess the influence of an island of arbitrary shape and position-dependent albedo on L_t. Such a code could be used to effect a correction for the island perturbation.

Appendix: An alternate computational procedure for an island of arbitrary shape

One difficulty with our Monte Carlo approach described in Section 2 is the necessity of computing Ω' (Figure 1) when the photon is close to the island. This computation is tractable only when the island has a simple shape, e.g., a circular disk. An alternate procedure is required for an

island of arbitrary shape. Here, we present a simple modification of the procedure presented in the text.

As described in Section 2, there are three contributions to the Monte Carlo estimator (L_1, L_2, and L_3). In the revised approach, the procedures for L_1 and L_2 are unchanged, but L_3 is computed using a completely different approach. Rather than estimating the L_3 contribution at each interaction (Section 2), the estimate is made only when the photon actually strikes the island. When this occurs, the estimate of L_3 (assuming as before that the island is a lambertian reflector) is

$$L_3 = \frac{\omega_0^n A \cos\theta_0}{2\pi} T(\hat{\xi}_0),$$

where n is the number of collisions made by the photon before striking the island. This completely avoids the computation of Ω'. At each interaction one need only compute L_1 and then determine if the photon could specularly reflect from the surface toward the sun (to determine if L_2 makes a contribution). Finally, between any two collisions one must determine if the island intersects the path, in which case L_3 is given by the above equation. Clearly, an arbitrarily shaped island represents little additional difficulty. Also, a spatially dependent island albedo is straightforward to implement.

We have implemented this procedure for a circular island. Figure 11 provides the resulting statistics for the same simulation as presented in Figure 3, which used the procedure described in Section 2. Comparison of the two figures shows that the alternate technique for dealing with the island's contribution to L_t is as effective as our earlier, and more complex, approach.

References

[1] H. R. Gordon and M. Wang, "Retrieval of water-leaving radiance and aerosol optical thickness over the oceans with SeaWiFS: A preliminary algorithm," Applied Optics **33**, 443–452 (1994).

[2] S. B. Hooker, W. E. Esaias, G. C. Feldman, W. W. Gregg and C. R. McClain, *SeaWiFS Technical Report Series: Volume 1, An Overview of SeaWiFS and Ocean Color* (NASA, Greenbelt, MD, Technical Memorandum 104566, July 1992).

[3] M. Wang and H. R. Gordon, "Estimating aerosol optical properties over the oceans with MISR: Some preliminary studies," Applied Optics **33**, 4042–4057 (1994).

[4] M. Wang and H. R. Gordon, "Retrieval of the Columnar Aerosol Phase Function and Single Scattering Albedo from Sky Radiance over the Ocean: Simulations," Applied Optics **32**, 4598–4609 (1993).

[5] M. D. King and B. M. Herman, "Determination of the Ground Albedo and the Index of Absorption of Atmospheric Particulates by Remote Sensing. Part I: Theory," Jour. Atmos. Sci. **36**, 163–173 (1979).

[6] M. A. Box and A. Deepak, "Retrieval of Aerosol Size Distributions by Inversion of Simulated Aureole Data in the Presence of Multiple Scattering," Applied Optics **18**, 1376–1382 (1979).

[7] M. A. Box and A. Deepak, "An Approximation to Multiple Scattering in the Earth's Atmosphere: Almucantar Radiance Formulation," Jour. Atmos. Sci. **38**, 1037–1048 (1981).

[8] T. Nakajima, M. Tanaka and T. Yamauchi, "Retrieval of the Optical Properties of Aerosols from Aureole and Extinction Data," Applied Optics **22**, 2951–2959 (1983).

[9] M. Wendisch and W. von Hoyningen-Huene, "High Speed Version of the Method of 'Successive Order of Scattering' and its Application to Remote Sensing," Beitr. Phys. Atmosph. **64**, 83–91 (1991).

[10] E. P. Shettle and R. W. Fenn, *Models for the Aerosols of the Lower Atmosphere and the Effects of Humidity Variations on Their Optical Properties* (Air Force Geophysics Laboratory, Hanscomb AFB, MA 01731, AFGL–TR–79-0214, 1979).

[11] H. R. Gordon and M. Wang, "Surface Roughness Considerations for Atmospheric Correction of Ocean Color Sensors. 1: The Rayleigh Scattering Component," Applied Optics **31**, 4247–4260 (1992).

[12] H. R. Gordon and M. Wang, "Surface Roughness Considerations for Atmospheric Correction of Ocean Color Sensors. 2: Error in the Retrieved Water-leaving Radiance," Applied Optics **31**, 4261–4267 (1992).

Figure Captions

Figure 1. Schematic for computing the island's contribution to the sky radiance.

Figure 2. Aerosol scattering phase functions used in the simulations.

Figure 3. Histogram of the number of occurrences of given values of L_t in intervals of 0.0005×10^{-2} for 1000 simulations of 10^4 photons each. The dotted line represents the estimate of the mean value of L_t for the 10^7 photons.

Figure 4. Computed value of L_t as a function of R for C80, $\theta_v = \theta_0 = 60°$, $\tau_a = 0.1$, 0.25, and 0.5, and $h = 1$ and 2 km with the radiometer located at the center of the island: (a) $\phi = 10°$; (b) $\phi = 90°$; (c) $\phi = 180°$.

Figure 5. Comparison between the computed values of L_t as a function of R with the radiometer at the center and the edge of the island for C80, $\theta_v = \theta_0 = 60°$, $\tau_a = 0.1$, 0.25, and 0.5, and $h = 1$ km: (a) $\phi = 10°$; (b) $\phi = 90°$; (c) $\phi = 180°$.

Figure 6. Comparison between the computed values of L_t as a function of R with the island's albedo $A = 0.5$ and 1.0, the radiometer at the center of the island, phase function C80, $\theta_v = \theta_0 = 60°$, $\tau_a = 0.1$, 0.25, and 0.5, and $h = 1$ km.

Figure 7. Comparison between the computed values of L_t as a function of R for phase functions C80 and T80, with the radiometer at the center of the island, $\theta_v = \theta_0 = 60°$, $\tau_a = 0.1$, 0.25, and 0.5, and $h = 1$ km.

Figure 8. Relative error in L_t in the almucantar of the sun ($\theta_0 = 60°$) as a function of the azimuth angle for a radiometer located at the center and edge of the island. For these curves, $\tau_r = 0.25$, $\tau_a = 0.25$, $h = 1$ km, and $R = 5$ km.

Figure 9. Comparison between the retrieved and the true values of $\omega_0 P(\Theta)$ employing simulated sky radiance pseudodata in the absence of the island. $\tau_r = 0.25$, $\tau_a = 0.25$, $h = 1$ km, and $R = 5$ km.

Figure 10. Comparison between the retrieved and the true values of $\omega_0 P(\Theta)$ employing simulated sky radiance pseudodata obtained at the center and the edge of the island. $\tau_r = 0.25$, $\tau_a = 0.25$, $h = 1$ km, and $R = 5$ km.

Figure 11. Histogram of the number of occurrences of given values of L_t in intervals of 0.0005 $\times 10^{-2}$ for 1000 simulations of 10^4 photons each, utilizing the method described in the Appendix for computing the contribution L_3. The dotted line represents the estimate of the mean value of L_t for the 10^7 photons.

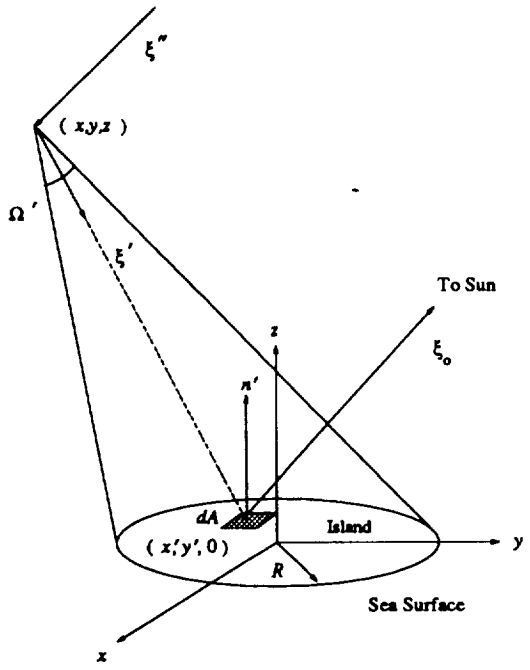

Figure 1. Schematic for computing the island's contribution to the sky radiance.

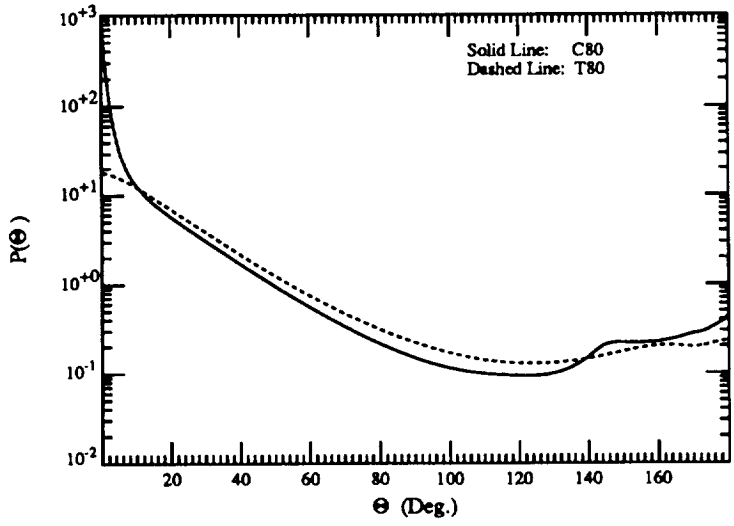

Figure 2. Aerosol scattering phase functions used in the simulations.

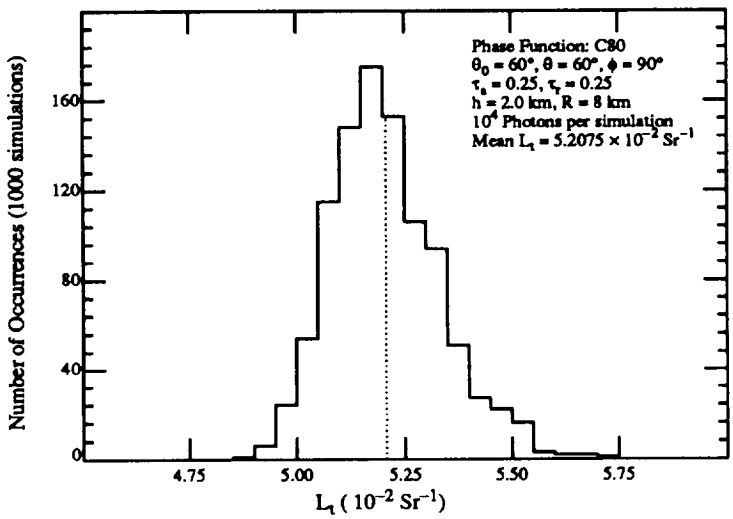

Figure 3. Histogram of the number of occurrences of given values of L_t in intervals of 0.0005×10^{-2} for 1000 simulations of 10^4 photons each. The dotted line represents the estimate of the mean value of L_t for the 10^7 photons.

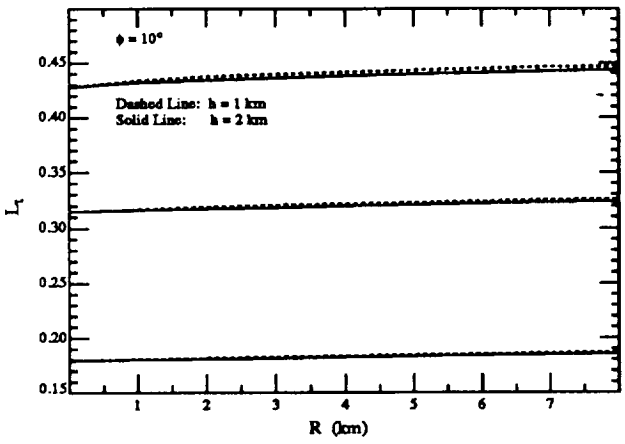

Figure 4a.

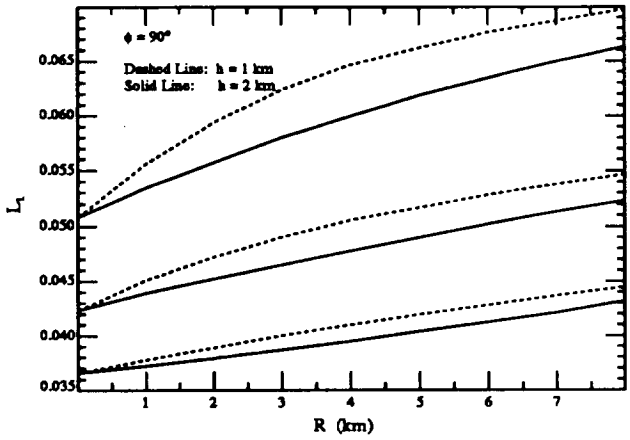

Figure 4b.

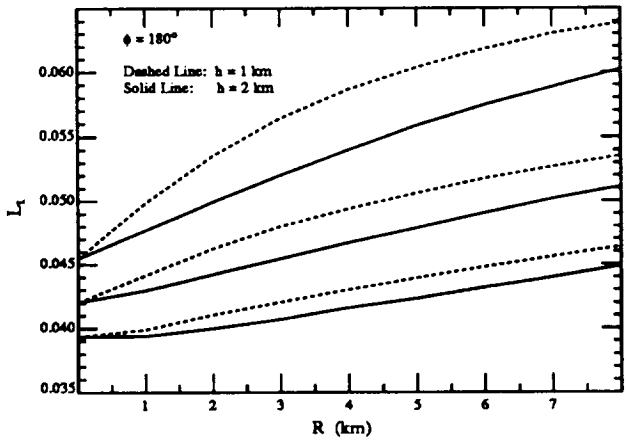

Figure 4c.

Figure 4. Computed value of L_t as a function of R for C80, $\theta_v = \theta_0 = 60°$, $\tau_a = 0.1$, 0.25, and 0.5, and $h = 1$ and 2 km with the radiometer located at the center of the island: (a) $\phi = 10°$; (b) $\phi = 90°$; (c) $\phi = 180°$.

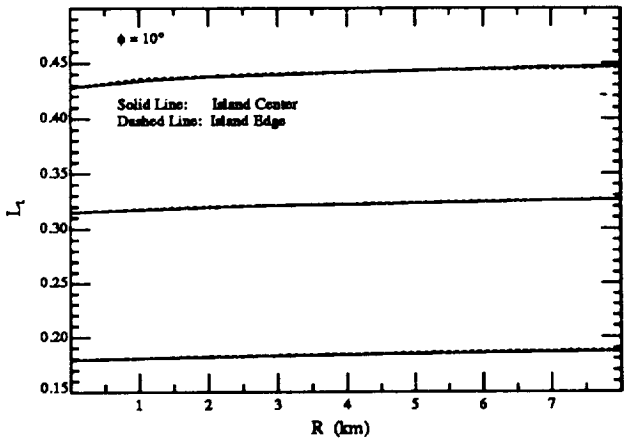

Figure 5a.

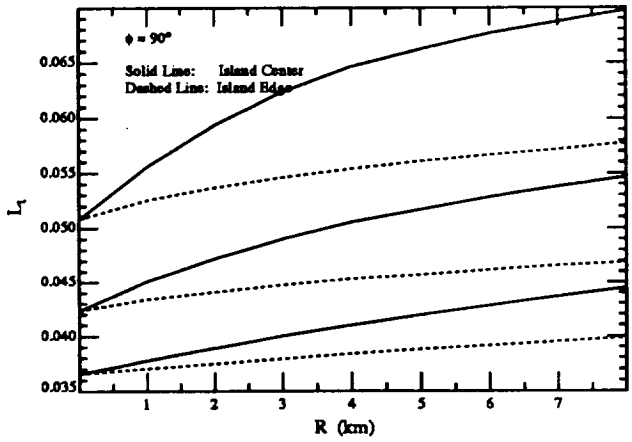

Figure 5b.

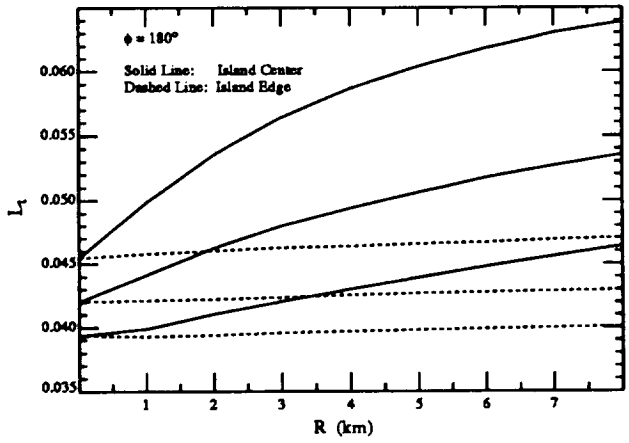

Figure 5c.

Figure 5. Comparison between the computed values of L_t as a function of R with the radiometer at the center and the edge of the island for C80, $\theta_v = \theta_0 = 60°$, $\tau_a = 0.1$, 0.25, and 0.5, and $h = 1$ km: (a) $\phi = 10°$; (b) $\phi = 90°$; (c) $\phi = 180°$.

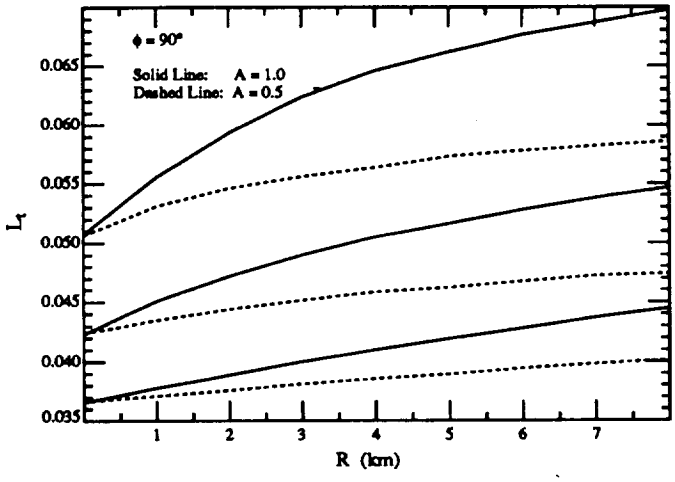

Figure 6. Comparison between the computed values of L_t as a function of R with the island's albedo $A = 0.5$ and 1.0, the radiometer at the center of the island, phase function C80, $\theta_v = \theta_0 = 60°$, $\tau_a = 0.1$, 0.25, and 0.5, and $h = 1$ km.

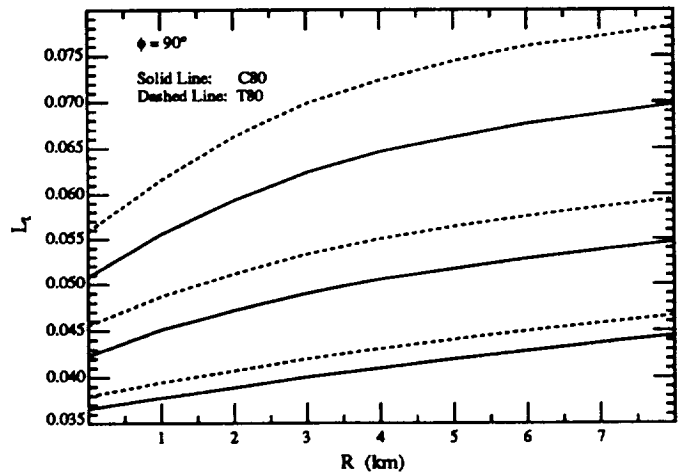

Figure 7. Comparison between the computed values of L_t as a function of R for phase functions C80 and T80, with the radiometer at the center of the island, $\theta_v = \theta_0 = 60°$, $\tau_a = 0.1$, 0.25, and 0.5, and $h = 1$ km.

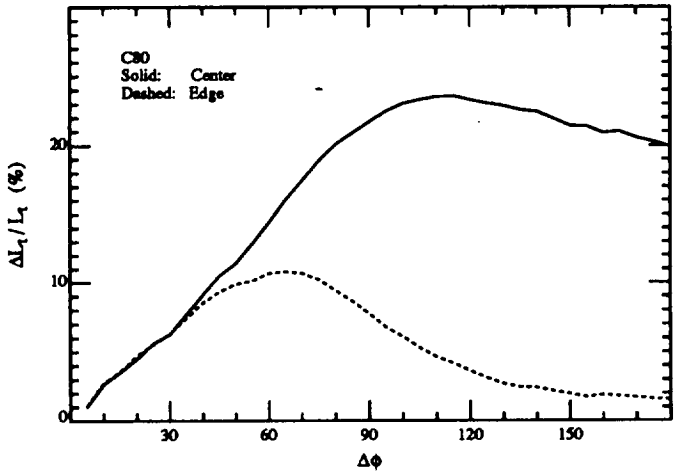

Figure 8. Relative error in L_t in the almucantar of the sun ($\theta_0 = 60°$) as a function of the azimuth angle for a radiometer located at the center and edge of the island. For these curves, $\tau_r = 0.25$, $\tau_a = 0.25$, $h = 1$ km, and $R = 5$ km.

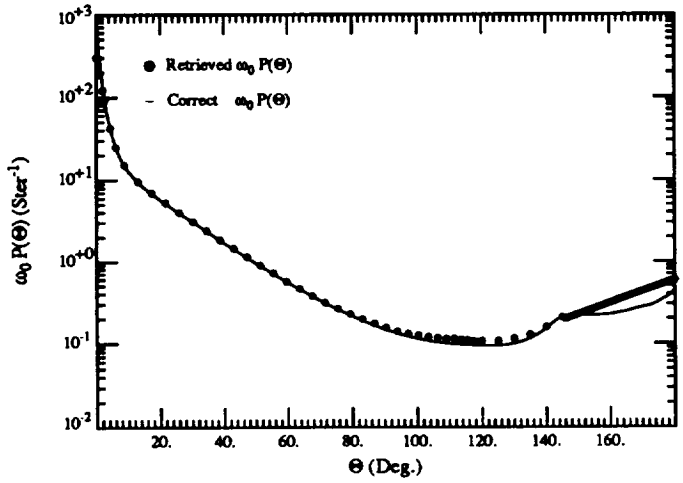

Figure 9. Comparison between the retrieved and the true values of $\omega_0 P(\Theta)$ employing simulated sky radiance pseudodata in the absence of the island. $\tau_r = 0.25$, $\tau_a = 0.25$, $h = 1$ km, and $R = 5$ km.

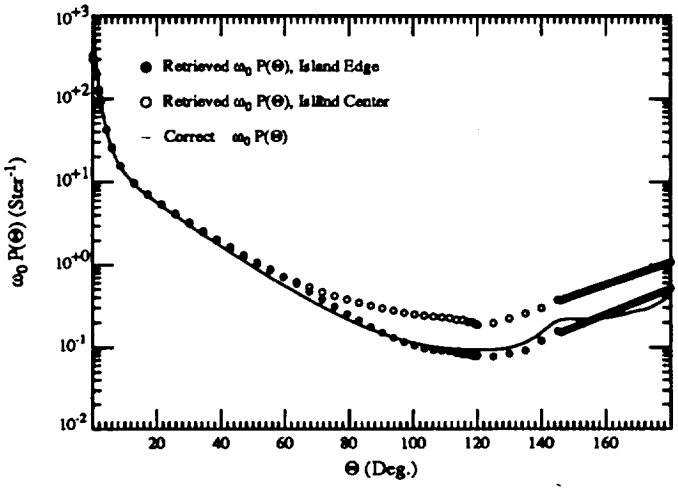

Figure 10. Comparison between the retrieved and the true values of $\omega_0 P(\Theta)$ employing simulated sky radiance pseudodata obtained at the center and the edge of the island. $\tau_r = 0.25$, $\tau_a = 0.25$, $h = 1$ km, and $R = 5$ km.

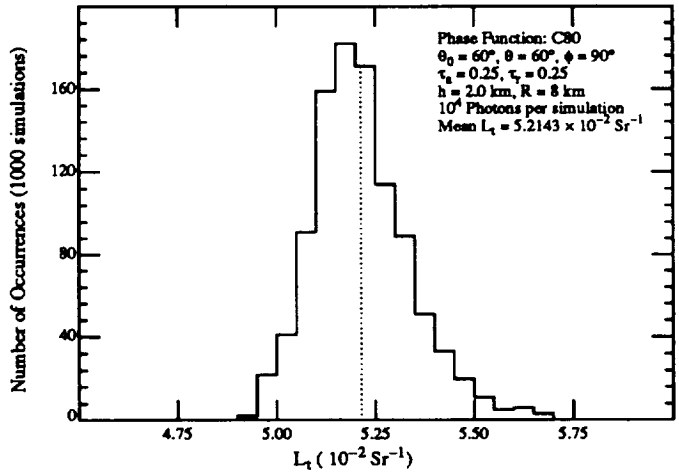

Figure 11. Histogram of the number of occurences of given values of L_t in intervals of 0.0005×10^{-2} for 1000 simulations of 10^4 photons each, utilizing the method described in the Appendix for computing the contribution L_3. The dotted line represents the estimate of the mean value of L_t for the 10^7 photons.

Appendix 4

Remote sensing of ocean color: a methodology for dealing with broad spectral bands and significant out-of-band response

by

Howard R. Gordon

Department of Physics

University of Miami

Coral Gables, FL 33124

(Submitted for publication in *Applied Optics*)

Acknowledgment

The author wishes to thank K. Ding and F. He for helping with some of the computations, and the National Aeronautics and Space Administration for support under Grant NAGW-273 and Contracts NAS5-31363 and NAS5-31743.

Abstract

A methodology for delineating the influence of finite spectral band widths and significant out-of-band response of sensors for remote sensing of ocean color is developed and applied to the Sea-viewing Wide-Field-of-view Sensor (SeaWiFS). The basis of the method is the application of the sensor's spectral response functions to the individual components of the top-of-the-atmosphere (TOA) radiance rather than the TOA radiance itself. For engineering purposes, this approach allows one to assess easily (and quantitatively) the potential of a particular sensor design for meeting the system — sensor plus algorithms — performance requirements.

In the case of SeaWiFS, two significant conclusions are reached. First, it is found that the out-of-band effects on the water-leaving radiance component of the top of the atmosphere radiance are of the order of a few percent compared to a sensor with narrow spectral response. This implies that verification that the SeaWiFS system — sensor plus algorithms — meets the goal of providing the water-leaving radiance in the blue in clear ocean water to within 5% will require measurements of the water-leaving radiance over the entire visible spectrum as opposed to just narrow-band (10–20 nm) measurements in the blue. Second, it is it is found that the atmospheric correction of SeaWiFS can be degraded by the influence of water vapor absorption in the shoulders of the atmospheric correction bands in the near infrared. This absorption causes an apparent spectral variation of the aerosol component between these two bands that will be uncharacteristic of the actual aerosol present, leading to an error in correction. This effect is dependent on the water vapor content of the atmosphere. At typical water vapor concentrations the error is larger for aerosols with a weak spectral variation in reflectance than for those displaying a strong spectral variation. If the water vapor content is known, a simple procedure is provided to remove the degradation of the atmospheric correction. Uncertainty in the water vapor content will limit the accuracy of the SeaWiFS correction algorithm.

1. Introduction

In developing algorithms for ocean remote sensing data acquired by earth-orbiting satellites in the visible, where the spectrum of the radiance scattered by the ocean-atmosphere system in the atmospheric transmission windows is a relatively smooth function of wavelength, it is usually assumed that the spectral response of the instrument is a Dirac delta function, i.e., the necessary radiative transfer (RT) computations for a given spectral band are carried out at a single wavelength. In this paper a methodology is developed for adapting such computations to sensors with nominal spectral bandwidths $\sim$ 20–40 nm, and with significant out-of-band response. As a working example, we apply the analysis to the Sea-viewing Wide-Field-of-view Sensor (SeaWiFS)[1] scheduled for launch in 1995. The radiometric specifications of SeaWiFS are presented in the Appendix.

We begin by reviewing the decomposition of the measured atmosphere-leaving radiance into components resulting from Rayleigh scattering, aerosol scattering, and radiance backscattered out of the ocean. Then the process of combining the top of the atmosphere (TOA) radiance with the spectral response of the sensor is discussed and applied to the individual components of the TOA radiance using simulations that include the absorption of atmospheric Ozone but ignore the influence of other absorbing gases such as H_2O and O_2. The influence of absorption by these gases is then considered in the next section. Finally, the overall influence of the spectral band width and out-of-band response on atmospheric correction is discussed along with techniques for minimizing the effects in the case of SeaWiFS.

2. Decomposition of the measured radiance

Consider a spherical coordinate system at the sea surface with the z-axis toward the zenith and the x-y plane on the sea surface. A vector directed toward the sun has polar and azimuth angles θ_0 and ϕ_0, respectively, and a vector directed toward the sensor has polar and azimuth angles θ_v and ϕ_v, respectively. The radiance exiting the top of the atmosphere (TOA) in a direction specified by (θ_v, ϕ_v), $L_t(\lambda)$, at any wavelength λ is given by[2]

$$L_t(\lambda) = L_r(\lambda) + L_a(\lambda) + L_{ra}(\lambda) + tL_w(\lambda), \tag{1}$$

where L_r is the reflectance resulting from multiple scattering by air molecules (Rayleigh scattering) in the absence of aerosols, L_a is the reflectance resulting from multiple scattering by aerosols in the absence of the air, L_{ra} is the interaction term between molecular and aerosol scattering,[3] and L_w is the water-leaving reflectance. The term L_{ra} accounts for the interaction between Rayleigh and aerosol scattering, e.g., photons first scattered by the air then scattered by aerosols, or photons first scattered by aerosols then air, etc. This term is zero in the single scattering case, in which photons are only scattered once, and it can be ignored as long as the amount of multiple scattering is small, i.e., at small Rayleigh and aerosol optical thicknesses. The contribution from specular reflection of the solar beam from the sea surface (sun glitter) is ignored because the scan plane of most color sensors can be tilted to avoid the glitter pattern. In this equation, t is the diffuse transmittance of the atmosphere. It is approximated by

$$t(\theta_v, \lambda) = \exp\Big[-\left(\frac{\tau_r(\lambda)}{2} + \tau_{Oz}(\lambda)\right)\left(\frac{1}{\mu_v}\right)\Big] t_a(\theta_v, \lambda), \tag{2}$$

where

$$t_a(\theta_v, \lambda) = \exp\Big[-\frac{[1 - \omega_a(\lambda) F_a(\mu_v, \lambda)]\tau_a(\lambda)}{\mu_v}\Big], \tag{3}$$

$\mu_v = \cos\theta_v$, τ_r, τ_{Oz}, and τ_a are, respectively, the Rayleigh, Ozone, and aerosol optical thicknesses, and ω_a is the aerosol single scattering albedo. $F_a(\mu_v, \lambda)$ is related to the scattering phase function of the aerosol and is given by

$$F_a(\mu_v, \lambda) = \frac{1}{4\pi} \int_0^1 P_a(\alpha, \lambda)\, d\mu\, d\phi,$$

where $P_a(\alpha, \lambda)$ is the aerosol phase function at λ (normalized to 4π) for a scattering angle α, and

$$\cos\alpha = \mu\mu_v + \sqrt{(1 - \mu^2)(1 - \mu_v^2)}\cos\phi.$$

If θ_v is $\lesssim 60°$ the factor $[1 - \omega_a(\lambda) F_a(\mu_v, \lambda)]$ is usually $\ll 1$, so t_a depends only weakly on the aerosol optical thickness and is usually taken to be unity.

The retrieval of $L_w(\lambda)$ from $L_t(\lambda)$ is called atmospheric correction. To effect this, $L_r(\lambda) + L_a(\lambda) + L_{ra}(\lambda)$ must be estimated. The initial development of the atmospheric correction algorithm for the Coastal Zone Color Scanner[4,5] (CZCS), the proof-of-concept ocean color instrument, was based on the assumption of single scattering, wherein $L_{ra}(\lambda) = 0$ and

$$L_r(\lambda) = L_r^{ss}(\lambda) = F_0'(\lambda)\omega_r(\lambda)\tau_r(\lambda)p_r(\theta_v, \theta_0, \lambda)/4\pi\cos\theta_v. \tag{4}$$

where

$$p_r(\theta_v, \theta_0, \lambda) = P_r(\theta_-, \lambda) + \Big(r(\theta_v) + r(\theta_0)\Big) P_r(\theta_+, \lambda),$$

$$\cos\theta_\pm = \pm\cos\theta_0\cos\theta_v - \sin\theta_0\sin\theta_v\cos(\phi_v - \phi_0),$$

$\omega_r = 1$, P_r is the Rayleigh scattering phase function, and $r(\alpha)$ is the Fresnel reflectance of the air-sea interface for an incident angle α. $F_0'(\lambda)$ is the instantaneous extraterrestrial solar irradiance $F_0(\lambda)$ reduced by two trips through the Ozone layer, i.e.,

$$F_0'(\lambda) = F_0(\lambda)T_{Oz}(\lambda) = F_0(\lambda)\exp\Big[-\tau_{Oz}(\lambda)M\Big] \tag{5}$$

where $T_{Oz}(\lambda)$ is the two-way transmittance of the Ozone layer, $\tau_{Oz}(\lambda)$ is the Ozone optical thickness, and M is the two-way air mass:

$$M = \left(\frac{1}{\cos\theta_v} + \frac{1}{\cos\theta_0}\right).$$

The aerosol radiance in the single scattering approximation, $L_a^{ss}(\lambda)$, is given by a similar expression with the subscript "r" replaced by "a" for aerosol ($\omega_a \leq 1$). Typically the single scattering approximation leads to an error of $\lesssim 5\%$ in $L_r(\lambda)$.[6] In contrast, the error in $L_a + L_{ra}$ estimated by single scattering is of the order of 30–90%, depending on the aerosol model and geometry;[2] however, $L_a + L_{ra}$ is approximately $\propto L_a^{ss}$, i.e.,

$$L_a(\lambda) + L_{ra}(\lambda) = C(\theta_v, \phi_v, \theta_0, \phi_0, L_a^{ss}(\lambda), \lambda)\, L_a^{ss}(\lambda), \tag{6}$$

where $C(\theta_v, \phi_v, \theta_0, \phi_0, L_a^{ss}(\lambda), \lambda)$ depends only weakly on $L_a^{ss}(\lambda)$ and λ. For example, for the simulations presented in Figures 1 and 2 of Ref. 2 for $\theta_0 = 60°$, $\phi_0 = 0$, $\theta_v \approx 45°$, and $\phi_v = 90°$, the quantity $C(\theta_v, \phi_v, \theta_0, \phi_0, L_a^{ss}(\lambda), \lambda)$ shows a near-linear dependence on $L_a^{ss}(\lambda)$, and varies from ~ 1.79 at 865 nm to ~ 1.88 at 443 nm for the Maritime aerosol model with a relative humidity of 98% (M98), while for the Tropospheric model with a relative humidity of 70% (T70), the corresponding variation was from ~ 1.33 to ~ 1.26. In contrast, the values of $L_a^{ss}(443)/L_a^{ss}(865)$ ranged from 1.9 for M98 to 4.2 for T70. Thus, the spectral variation of $L_a^{ss}(\lambda)$ far exceeds that of $C(\theta_v, \phi_v, \theta_0, \phi_0, L_a^{ss}(\lambda), \lambda)$. Note, however, that the spectral variation in $L_a^{ss}(\lambda)$ is still small compared to $L_r^{ss}(\lambda)$: $L_r^{ss}(443)/L_r^{ss}(865) \approx 28$.

In the proposed SeaWiFS atmospheric correction algorithm,[2] all of the effects of multiple scattering are included, e.g., L_r is computed using a multiple scattering code (including polarization).

However, for the purposes of including the effects of the sensor's spectral response, it is legitimate to utilize the single scattering approximation, i.e., $L_r(\lambda) = L_r^{ss}(\lambda)$ and

$$L_a(\lambda) + L_{ra}(\lambda) = C(\theta_v, \phi_v, \theta_0, \phi_0) L_a^{ss}(\lambda), \tag{7}$$

since the L_r^{ss} and L_a^{ss} terms contain nearly all of the *spectral* variation of L_r and $L_a + L_{ra}$, respectively. Note, we will now assume an $L_a^{ss}(\lambda)$- and wavelength-independent $C(\theta_v, \phi_v, \theta_0, \phi_0, L_a^{ss}(\lambda), \lambda)$, i.e., the aerosol *multiple* scattering effects are assumed to be independent of $L_a^{ss}(\lambda)$ and wavelength.

3. Band averaging

We now compute the expected radiance at the sensor, given the spectral response $S_i(\lambda)$ of the i^{th} spectral band. $S_i(\lambda)$ provides the output current (or voltage) from the detector for a unit radiance of wavelength λ, e.g., $\int S_i(\lambda)\, d\lambda$ would be the output current for a *spectrally flat* source of radiance of magnitude 1 mW/cm^2μm Sr. We define the "band" radiance for the i^{th} spectral band when viewing a source of radiance $L(\lambda)$ to be

$$\langle L(\lambda) \rangle_{S_i} \equiv \frac{\int L(\lambda) S_i(\lambda)\, d\lambda}{\int S_i(\lambda)\, d\lambda} \tag{8}$$

The output current (or voltage) will then be $\propto \langle L(\lambda) \rangle_{S_i}$.

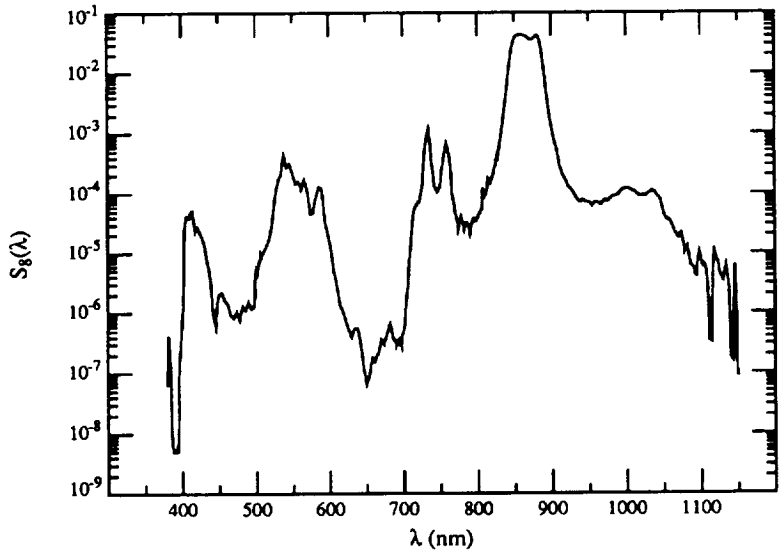

Figure 1. Spectral response of SeaWiFS band 8, normalized such that $\int S_8(\lambda)\, d\lambda = 1$. Data are taken from Barnes et al.[7]

In the case of SeaWiFS, some bands have significant out-of-band response. An example is shown in Figure 1 which provides S_8 for Band 8, nominally 845–885 nm. Note the significant response from $\sim$ 520–580 nm and near 750 nm. In fact, when viewing a source for which $L(\lambda) \propto \lambda^{-4} F_0(\lambda)$, e.g., L_r^{**}, approximately 9% of the signal in Band 8 derives from $\lambda < 600$ nm. In contrast, only about 0.7% of the signal derives from $\lambda < 600$ nm for a spectrally flat source.

3.A. Band-averaged L_r

In the notation of Eq. (8),

$$\langle L_r(\lambda)\rangle_{S_i} = \langle \tau_r(\lambda) F_0'(\lambda)\rangle_{S_i} G(\theta_0, \theta_v, \phi_v),$$

where $G(\theta_0, \theta_v, \phi_v)$ is a purely geometrical factor. If we ignored the presence of the Ozone layer, $F_0' = F_0$, and we could write

$$\langle \tau_r(\lambda) F_0(\lambda)\rangle_{S_i} = \langle \tau_r(\lambda)\rangle_{F_0 S_i} \langle F_0(\lambda)\rangle_{S_i},$$

where

$$\langle \tau_r(\lambda)\rangle_{F_0 S_i} \equiv \frac{\int \tau_r(\lambda) F_0(\lambda) S_i(\lambda)\, d\lambda}{\int F_0(\lambda) S_i(\lambda)\, d\lambda}. \tag{9}$$

This is very convenient because it separates τ_r and F_0 and allows us to carry out the computation of $I_r \equiv L_r / F_0$ for Band i by using $\langle \tau_r(\lambda)\rangle_{F_0 S_i}$ for the Rayleigh optical thickness. Multiplication of I_r by $\langle F_0(\lambda)\rangle_{S_i}$ then yields the desired $\langle L_r(\lambda)\rangle_{S_i}$. To include the effect of Ozone, we hypothesize that since $\tau_{Oz} M \ll 1$,

$$\langle \tau_r(\lambda) F_0'(\lambda)\rangle_{S_i} \approx \langle \tau_r(\lambda)\rangle_{F_0 S_i} \langle F_0(\lambda)\rangle_{S_i} \exp\left[-\langle \tau_{Oz}(\lambda)\rangle_{F_0 S_i} M\right]. \tag{10}$$

We tested this hypothesis by utilizing the predicted $S_i(\lambda)$ for the SeaWiFS bands.[7] To effect the test, $\tau_r(\lambda)$ was taken from Travis and Hansen:[8]

$$\tau_r = 0.008569\lambda^{-4}\left(1 + 0.0113\lambda^{-2} + 0.00013\lambda^{-4}\right), \tag{11}$$

where λ is in μm. Following André and Morel[9] the Ozone absorption coefficient $k_{Oz}(\lambda)$ was taken from Nicolet.[10] The value of τ_{Oz} is related to k_{Oz} by

$$\tau_{Oz}(\lambda) = k_{Oz}(\lambda)\frac{DU}{1000},$$

where DU is the Ozone concentration in mAtm-cm (Dobson Units). $F_0(\lambda)$ was taken from Neckel and Labs.[11] Table 1 provides a comparison between the right- and left-hand sides of Eq. (10) for an Ozone concentration of 350 DU. The large % difference for Band 8 is due to the significant out-

Table 1: % difference between the right (R) and left (L) sides of Eq. (10) for $M = 3$ for the SeaWiFS bands.

Band	100%(L-R)/L
1	−0.008
2	−0.010
3	−0.055
4	+0.106
5	−0.168
6	−0.010
7	−0.031
8	−0.499

of-band response between 500 and 600 nm; however, for $\theta_0 = 60°$ and nadir viewing ($M = 3$), this error translates to an error in $\langle L_r(\lambda)\rangle_{S_8}$ of $\sim 1/3$ to $2/3$ the quantization increment of the SeaWiFS on-board 10-bit digitizer (depending on the amplifier gain setting), i.e., less than 1 digital count

Table 2: Quantities needed to compute $\langle L_r(\lambda)\rangle_{S_i}$ and $L_r(\lambda_i)$ for the SeaWiFS bands.

Band (i)	$\langle\tau_r(\lambda)\rangle_{F_0S_i}$	$\tau_r(\lambda_i)$	$\langle F_0(\lambda)\rangle_{S_i}$ mW/cm$^2\mu$m sr	$F_0(\lambda_i)$ mW/cm$^2\mu$m sr	$\langle k_{Oz}(\lambda)\rangle_{F_0S_i}$ (×1000)	$k_{Oz}(\lambda_i)$ (×1000)
1	0.3132	0.3185	170.79	180.80	1.03	0.81
2	0.2336	0.2361	189.45	194.95	4.00	3.75
3	0.1547	0.1560	193.66	198.85	25.36	22.27
4	0.1330	0.1324	188.35	193.65	42.00	42.50
5	0.0947	0.0938	185.33	190.25	93.38	90.38
6	0.0446	0.0436	153.41	153.50	46.85	45.92
7	0.0256	0.0255	122.24	122.40	8.37	7.42
8	0.0169	0.0155	98.82	97.10	4.85	3.71

(DC) from the sensor. Thus, we will employ the approximation in Eq. (10) to treat the influence of Ozone absorption on all three terms in Eq. (1). Specifically, whenever τ_{Oz} occurs, the spectral averages will be computed assuming $\tau_{Oz} = 0$, and τ_{Oz} will be reintroduced into the final result

by replacing it with $\langle \tau_{Oz}(\lambda) \rangle_{F_0 S_i}$. The fact that the approximation is sufficiently accurate for computing $\langle L_r(\lambda) \rangle_{S_i}$ insures that it will be for the terms in Eq. (1) with weaker spectral variation, e.g., $L_a(\lambda)$. The values of $\langle \tau_r(\lambda) \rangle_{F_0 S_i}$, $\langle F_0(\lambda) \rangle_{S_i}$, and $\langle k_{Oz}(\lambda) \rangle_{F_0 S_i}$ for the SeaWiFS bands are provided in Table 2. Note that the ($\times$1000) notation for $\langle k_{Oz}(\lambda) \rangle_{F_0 S_i}$ means that the entries in the table have been multiplied by 1000, i.e., $\langle k_{Oz}(\lambda) \rangle_{F_0 S_i} = 1.03 \times 10^{-3}$ for Band 1. Table 2 also provides $\tau_r(\lambda_i)$, $F_0(\lambda_i)$, and $k_{Oz}(\lambda_i)$, where henceforth λ_i with $i = 1$ to 8 refers to the nominal wavelength of the band center of SeaWiFS Band i.

To assess the efficacy of the above techniques for determining $\langle L_r(\lambda) \rangle_{S_i}$ in the multiple scattering regime, we have computed multiple scattering values for this quantity for $\theta_0 = 60°$ and nadir viewing in two ways. First, $I_r(\lambda)$ was computed as a function of λ using $\tau_r(\lambda)$ and a multiple scattering (scalar) RT code. From this,

$$L_r(\lambda) = I_r(\lambda) F_0(\lambda) \exp[-\tau_{Oz}(\lambda) M]$$

was formed and the average, $\langle L_r(\lambda) \rangle_{S_i}$, over the SeaWiFS bands was computed directly. To effect this for fine increments in λ, $I_r(\lambda)$ was linearly interpolated from log-transformed values of $I_r(\lambda_i)$ and λ_i computed at 10 wavelengths, the nominal SeaWiFS band centers plus 380 and 1150 nm. This average is taken as the "correct" answer for the average. Second, the same RT code was

Table 3: % difference between the estimated (E) and correct (C) values of $\langle L_r(\lambda) \rangle_{S_i}$ as described in the text.

Band	100%(E-C)/C
1	+0.15
2	+0.12
3	+0.02
4	−0.01
5	−0.09
6	−0.01
7	−0.09
8	−0.05

operated with $\tau_r(\lambda_i)$ replaced by $\langle \tau_r(\lambda) \rangle_{F_0 S_i}$ to compute I_r for the i^{th} band, $I_r(i)$. Then, $\langle L_r(\lambda) \rangle_{S_i}$ was estimated from

$$\langle L_r(\lambda) \rangle_{S_i} = I_r(i) \langle F_0(\lambda) \rangle_{S_i} \exp[-\langle \tau_{Oz}(\lambda) \rangle_{F_0 S_i} M]. \quad (12)$$

This is similar to the method employing single scattering with $I_r(i)$ replacing $\langle \tau_r(\lambda) \rangle_{F_0 S_i} G(\theta_0, \theta_v, \phi_v)$. The resulting $\langle L_r(\lambda) \rangle_{S_i}$ is the "estimated" band-averaged $L_r(\lambda)$. Table 3 provides the % difference between the estimated and correct values of $\langle L_r(\lambda) \rangle_{S_i}$, for $\theta_0 = 60°$, nadir viewing, and an Ozone concentration of 350 DU. It is clear that Eq. (12) is capable of estimating the radiance to very high accuracy. In fact, in this example, the error is less than 1 DC for all of the SeaWiFS bands. Also, the excellent performance of the estimator attests to the viability of the treatment of the Ozone absorption.

3.B. Band-averaged $L_a + L_{ra}$

From Eq. (7), we see that the band-averaged aerosol component can be found by considering $L_a^{ss}(\lambda)$. At the core of both the CZCS and SeaWiFS atmospheric correction algorithms is the spectral variation of the normalized single-scattered aerosol radiance, i.e., $I_a^{ss}(\lambda) \equiv L_a^{ss}(\lambda)/F_0(\lambda)$. Two single wavelengths λ and λ_0 are used to define the atmospheric correction parameters $\varepsilon(\lambda, \lambda_0)$ given by

$$\varepsilon(\lambda, \lambda_0) = \frac{I_a^{ss}(\lambda)}{I_a^{ss}(\lambda_0)}. \tag{13}$$

Thus,

$$L_a^{ss}(\lambda) = F_0(\lambda) \varepsilon(\lambda, \lambda_0) I_a^{ss}(\lambda_0), \tag{14}$$

and

$$\langle L_a^{ss}(\lambda) \rangle_{S_i} = \langle F_0(\lambda) \rangle_{S_i} \langle \varepsilon(\lambda, \lambda_0) \rangle_{F_0 S_i} I_a^{ss}(\lambda_0). \tag{15}$$

Note that λ_0 is an arbitrary (single) wavelength; here we take it to be to be 865 nm, the nominal band center of SeaWiFS Band 8. Also, we have set $\tau_{Oz} = 0$. Ozone can be included as stated earlier by replacing $\langle F_0(\lambda) \rangle_{S_i}$ by $\langle F_0(\lambda) \rangle_{S_i} \exp[-\langle \tau_{Oz}(\lambda) \rangle_{F_0 S_i} M]$ in the final result. To proceed further, we need $\varepsilon(\lambda, \lambda_0)$, which can be computed using Eq. (4) with the subscript "r" replaced by "a" for aerosol. Wang and Gordon[12] have shown that for the aerosol models proposed by Shettle and Fenn[13] for LOWTRAN-6,[14] and used in Ref. 2, $\varepsilon(\lambda, \lambda_0)$ can be approximated by

$$\varepsilon(\lambda, \lambda_0) \approx \exp[c(\lambda_0 - \lambda)] \tag{16}$$

with $\lambda < \lambda_0$. The limits on c over the range 412 to 865 nm for the models that they[12] used were $0 \lesssim c \lesssim 1.9 \times 10^{-3}$ nm^{-1}. This equation is sufficiently accurate to examine the out-of-band effects on the aerosol component. Table 4 provides $\langle \varepsilon(\lambda, 865) \rangle_{F_0 S_i}$ and $\varepsilon(\lambda_i, 865)$, where λ_i is the

nominal center wavelength of Band i, and their % difference for $c = 2 \times 10^{-3}$ nm^{-1}. We note that,

Table 4: $\langle \varepsilon(\lambda, 865) \rangle_{F_0 S_i}$, $\varepsilon(\lambda_i, 865)$, and their % difference for $c = 2 \times 10^{-3}$ nm^{-1}.

Band	$\langle \varepsilon(\lambda, 865) \rangle_{F_0 S_i}$	$\varepsilon(\lambda_i, 865)$	% Diff.
1	2.4645	2.4744	−0.40
2	2.3192	2.3257	−0.28
3	2.1113	2.1170	−0.27
4	2.0350	2.0340	+0.05
5	1.8584	1.8590	+0.03
6	1.4842	1.4770	+0.49
7	1.2202	1.2214	−0.10
8	1.0131	1.0000	+1.31

with the exception of Band 8, the effect of the out-of-band response is $\lesssim 0.5\%$ of the nominal $\varepsilon(\lambda_i, 865)$. Thus, with the exception of Band 8, $\langle \varepsilon(\lambda, 865) \rangle_{F_0 S_i}$ should follow Eq. (16) nearly as well as $\varepsilon(\lambda_i, 865)$, i.e., the spectral variations of $\langle \varepsilon(\lambda, 865) \rangle_{F_0 S_i}$, $i = 1$ to 7, and $\varepsilon(\lambda_i, 865)$ will be nearly identical. This conclusion will be modified by the presence of gaseous absorption (Section 4B).

3.C. Band-averaged tL_w

The water-leaving radiance varies strongly with the pigment concentration, C, defined to be the sum of the concentrations of chlorophyll a and phaeophytin a. For band averaging purposes, we use the model proposed by Gordon et al.[15] This model yields the normalized water-leaving radiance, $[L_w(\lambda)]_N$ defined according to[16]

$$L_w(\lambda) = t(\theta_0, \lambda) \cos\theta_0 \, [L_w(\lambda)]_N,$$

as a function of C. It agrees well with the measurements of Clark[17] for $\lambda \lesssim 600$ nm. Disagreement in the red is thought to be due to the effects of instrument self shading.[18] It is convenient here to switch from radiance L to reflectance ρ defined to be $\pi L / F_0 \cos\theta_0$. The normalized water-leaving reflectance is then

$$[\rho_w(\lambda)]_N = \frac{\pi [L_w(\lambda)]_N}{F_0(\lambda)}.$$

Combining these two equations yields the desired

$$t(\theta_v, \lambda) L_w(\lambda) = \frac{\cos\theta_0}{\pi} t(\theta_v, \lambda) t(\theta_0, \lambda) F_0(\lambda) [\rho_w(\lambda)]_N,$$

and to assess band averaging, we need to compute $\langle t(\theta_v, \lambda) L_w(\lambda) \rangle_{S_i}$. We have carried out this computation for two pigment concentrations, $C = 0.03$ and 1.0 mg/m^3. The $[\rho_w(\lambda)]_N$ spectra used in the computation are provided in Figure 2. The reflectances presented for $\lambda > 700$ nm

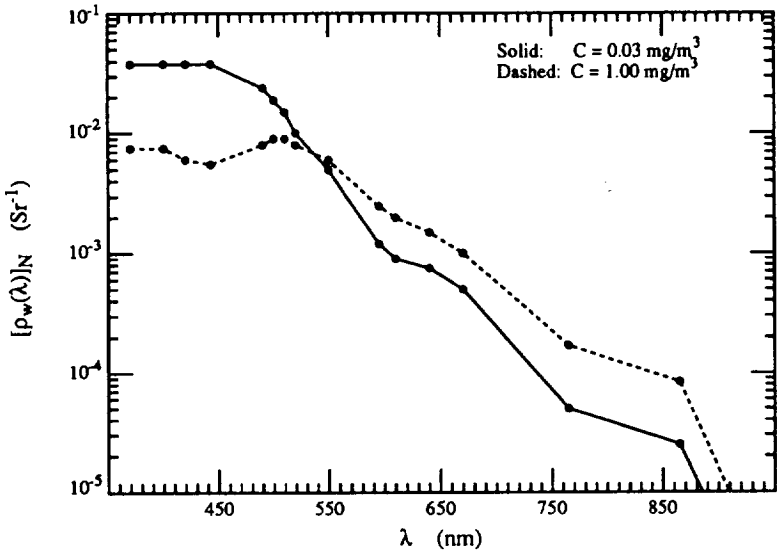

Figure 2. $[\rho_w(\lambda)]_N$ for $C = 0.03$ and 1.0 mg/m^3. Model computations were carried out at the points indicated by dots and interpolated to other wavelengths.

are estimated based on the absorption coefficient of water and the expected backscattering of phytoplankton. Measurements of L_w or the ocean backscattering properties have never been carried out at these wavelengths. Noting that $[\rho_w(\lambda)]_N$ varies by three orders of magnitude over the spectral range of interest (compared to a factor of ~ 33 for L_r), we expect that the out-of-band effects on tL_w for the red and NIR bands will be very severe. To calculate the required integrals, log-linear interpolation was used to estimate $[\rho_w(\lambda)]_N$, i.e., straight lines connecting the points on Figure 2. The reflectance was arbitrarily taken to be 10^{-10} Sr^{-1} at $\lambda = 1150$ nm. The band averaging yields

$$\langle t(\theta_v, \lambda) L_w(\lambda) \rangle_{S_i} = \frac{\cos\theta_0}{\pi} \langle F_0(\lambda) \rangle_{S_i} \langle t(\theta_v, \lambda) t(\theta_0, \lambda) [\rho_w(\lambda)]_N \rangle_{F_0 S_i}$$

We computed $\langle t(\theta_v,\lambda)t(\theta_0,\lambda)[\rho_w(\lambda)]_N\rangle_{F_0S_i}$ for $C = 0.03$ and 1.0 mg/m^3, and $M = 2$. The value $M = 2$, its minimum, was chosen to provide the strongest variation of tL_w with λ. This average is compared with $t(\theta_v,\lambda_i)t(\theta_0,\lambda_i)[\rho_w(\lambda_i)]_N$ in Table 5. The differences between X_i and Y_i are

Table 5: Comparison between the quantities

$X_i \equiv \langle t(\theta_v,\lambda)t(\theta_0,\lambda)[\rho_w(\lambda)]_N\rangle_{F_0S_i}$

and $Y_i \equiv t(\theta_v,\lambda_i)t(\theta_0,\lambda_i)[\rho_w(\lambda_i)]_N$ for

$C = 0.03$ and 1.0 mg/m^3, and $M = 2$.

The notation "2.77−2" etc., stands for 2.77×10^{-2}.

Band	$C = 0.03$ mg/m^3				$C = 1.0$ mg/m^3			
i	X_i	Y_i	% Diff.	DC Diff.	X_i	Y_i	% Diff.	DC Diff.
1	2.77−2	2.76−2	+3.6−1	+0.4	4.73−3	4.77−3	−8.7−1	−0.13
2	2.90−2	2.99−2	−3.2−0	−4.4	4.54−3	4.34−3	+4.6−0	+0.82
3	1.91−2	2.02−2	−5.4−0	−6.7	6.86−3	6.74−3	+1.7−0	+0.72
4	1.25−2	1.28−2	−1.7−0	−1.5	7.36−3	7.65−3	−3.8−0	−2.00
5	3.87−3	3.65−3	+6.1−0	+1.8	4.61−3	4.65−3	−1.0−0	−0.39
6	7.65−4	4.64−4	+6.5+1	+3.6	9.60−4	9.28−4	+3.4−0	+0.37
7	7.15−5	4.84−5	+4.7+1	+0.3	1.81−4	1.65−4	+1.0+1	+0.22
8	1.03−4	2.45−5	+3.2+2	+1.2	1.34−4	8.25−5	+6.3+1	+0.76

explained by the spectral shapes of $S_i(\lambda)$ and $L_w(\lambda)$. If S_i has a weak out-of-band maximum to the long-wave side of the band center maximum, X_i will be $< Y_i$ if $L_w(\lambda)$ decreases strongly with increasing wavelength, and vice versa if $L_w(\lambda)$ increases with λ. Bands 2 and 3 are examples of this behavior, for which a shift in the sign of $X_i - Y_i$ occurs between $C = 0.03$ and 1.0 mg/m^3. In contrast, Band 4 has secondary maxima on both sides of the band center (at $\sim$ 440 nm and 600 nm) and $X_i < Y_i$ at both concentrations. As expected, the long-wave bands show significant differences between X_i and Y_i with $X_i > Y_i$ due to light leakage from the blue and green (Figure 1). However, the difference is $\lesssim$ 1 DC in the NIR atmospheric correction bands, and it would appear that it is reasonable to assume that $X_i = 0$ in these bands. Noting that the goal of SeaWiFS is to retrieve $\langle L_w(\lambda)\rangle_{S_i}$ in Band 2 in clear water ($C \approx 0.03$ mg/m^3) with an error of $\leq 5\%$, Table 5 underscores the importance of measuring, or at least estimating, the full spectrum of L_w for the validation of satellite-retrieved $\langle L_w(\lambda)\rangle_{S_i}$.

In the spirit of our method for dealing with Ozone absorption, i.e., Eq. (10), we have tried to approximate $\langle t(\theta_v,\lambda)t(\theta_0,\lambda)[\rho_w(\lambda)]_N\rangle_{F_0S_i}$ by

$$\langle t(\theta_v,\lambda)t(\theta_0,\lambda)[\rho_w(\lambda)]_N\rangle_{F_0S_i} \approx t(\theta_v,i)t(\theta_0,i)\langle[\rho_w(\lambda)]_N\rangle_{F_0S_i}, \tag{17}$$

where

$$t(\theta,i) = \exp\left[-\left(\frac{\langle\tau_r(\lambda)\rangle_{F_0S_i}}{2} + \langle\tau_{Oz}(\lambda)\rangle_{F_0S_i}\right)\frac{1}{\cos\theta}\right]. \tag{18}$$

The % difference between the left- and right-hand-sides of Eq. (17) for $C = 0.03$ mg/m^3 and $M = 3$ is provided in Table 6. Clearly, the approximation is sufficiently accurate to estimate

Table 6: % difference between the right (R) and left (L) sides of Eq. (17) for $M = 3$ for the SeaWiFS bands.

Band	100%(R-L)/R
1	− 0.01
2	+ 0.01
3	+ 0.11
4	+ 0.18
5	+ 0.76
6	+ 2.62
7	+ 7.48
8	+25.28

$\langle t(\theta_v,\lambda)L_w(\lambda)\rangle_{S_i}$ in the visible bands.

4. Gas Absorption

With the exception of Ozone, to this point we have ignored the absorption of atmospheric gases, i.e., H_2O and O_2. In the case of SeaWiFS, only Band 7 (745–785 nm) was forced to encompass a gas absorption band, the O_2 A band ($\sim$ 759 – 770 nm), to provide an adequate signal-to-noise ratio. The other SeaWiFS bands have been placed in absorption-free atmospheric windows. However, even for spectral bands in the atmospheric windows, the effect of absorption may be important in the case of significant out-of-band response. For example, Figure 3 provides the spectral response of SeaWiFS Band 8 along with the H_2O-O_2 surface-to-zenith atmospheric transmittance (on a linear scale) from LOWTRAN.[14,19] Clearly, the H_2O absorption near 730, 850, and 890 nm, and the O_2

C-2

absorption near 760 nm will have some influence on the radiance measured in this spectral band. Also, the absence of gas absorption features for $\lambda \lesssim 570$ nm suggests that, other than Ozone, gas absorption below this wavelength can be ignored.

4.A. Influence on L_r

Within the framework we have developed for band averaging, the correct way of accurately including gas absorption would be to carry out detailed line-by-line radiative transfer computations through the absorption bands, e.g., in the case of the Rayleigh scattering component the "correct" value of $\langle L_r(\lambda)\rangle_{S_i}$ in Table 3 should be computed using an RT program that includes line-by-line, or at least narrow-band, absorption such as LOWTRAN. Unfortunately, LOWTRAN provides only

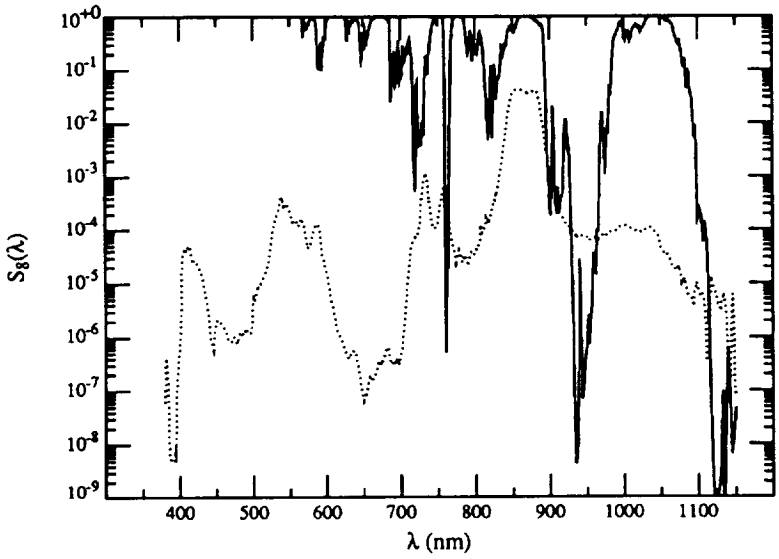

Figure 3. SeaWiFS Band 8 spectral response (dotted line) and atmospheric transmittance of H_2O and O_2 (solid line) for the LOWTRAN Tropical atmosphere (most water vapor). H_2O and O_2 transmittance is on a linear scale such that $10^{-1} \Rightarrow$ a transmittance of 0.9, $10^{-2} \Rightarrow$ a transmittance of 0.8, etc.

an approximate treatment of multiple scattering, and has no provision for a specularly reflecting lower boundary. However, since we expect the effect of gas absorption arising from the out-of band response to be small, highly accurate radiances are not really required for assessing the influence of

gas absorption. Thus, we will try to make a first-order estimate using LOWTRAN. To effect this, we computed $I_r = L_r/F_0$ for an aerosol-free atmosphere with a totally absorbing lower boundary (albedo = 0) for $\theta_0 = 60°$ and $\theta_v = 0$ ($M = 3$) using LOWTRAN. Ozone was removed under the assumption that it resides in a nonscattering layer at the TOA with the concentration that was used in the LOWTRAN calculations. This provided $I_r^{abs}(\lambda)$, the normalized Rayleigh component in the presence of absorption. Our multiple scattering code was then used in the same configuration to provide I_r at a select number of wavelengths (SeaWiFS band centers along with 380 and 1150 nm). These were interpolated as described in Section 3A to provide $N_r(\lambda)$, the normalized Rayleigh component in the absence of absorption. If LOWTRAN treated multiple scattering properly, $N_r(\lambda)$ and $I_r^{abs}(\lambda)$ would be identical in the atmospheric windows. This was forced by multiplying $I_r^{abs}(\lambda)$ by

$$1.015\, T_{Oz}^{-1} \left[1 - a(1050 - \lambda)^2\right]^{-1} ,$$

where $a = 1.5 \times 10^{-7}$ nm^{-2} and λ is in nm, to yield $A_r(\lambda)$, the Rayleigh component in the presence of absorption, and including a corrected treatment of multiple scattering. Thus, the principal difference between $N_r(\lambda)$ and $A_r(\lambda)$ is the absorption bands. Figure 4 provides this difference (%) showing the influence of the absorption bands for the LOWTRAN Subarctic winter atmosphere (the

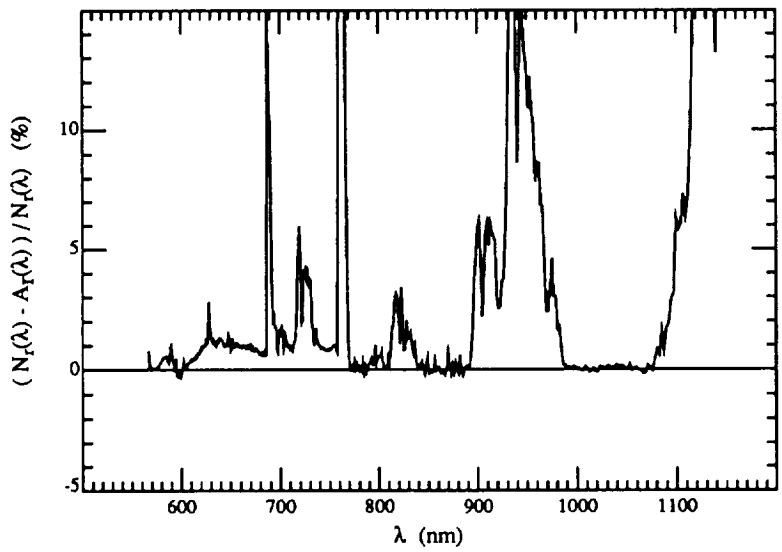

Figure 4. Difference between $N_r(\lambda)$ and $A_r(\lambda)$ as a function of λ for the LOWTRAN Subarctic winter atmosphere (least water vapor) and $M = 3$ as described in the text.

smallest LOWTRAN water vapor concentration). The influence of the gas absorption bands on the band-averaged radiances is provided by the difference between $\langle N_r(\lambda)F_0(\lambda)\rangle_{S_i}$ and $\langle A_r(\lambda)F_0(\lambda)\rangle_{S_i}$. This is presented in Table 7 as a % difference and a DC difference for Bands 6–8. For Bands 1–5, this difference is $\lesssim$ 0.02 DC because the principal out-of-band maxima for these are in the blue and green. In the preparation of Table 7, the O_2 A absorption band has been removed from the Band 7 computation of $\langle A_r(\lambda)F_0(\lambda)\rangle_{S_i}$, since Ding and Gordon[20] have provided a method of accounting for this in-band absorption feature. However, it has been included in the computations for all other bands. We note that with the exception of Band 6, the error in using $\langle N_r(\lambda)F_0(\lambda)\rangle_{S_i}$,

Table 7: $\langle N_r(\lambda)F_0(\lambda)\rangle_{S_i} - \langle A_r(\lambda)F_0(\lambda)\rangle_{S_i}$ in % and in DC (in parenthesis) for $\theta_0 = 60°$ and nadir viewing.

LOWTRAN model	H_2O g/cm^2	Band 6	Band 7	Band 8
Tropical	3.322	1.23 (1.58)	0.64 (0.52)	0.82 (0.50)
Midlatitude summer	2.356	0.86 (1.10)	0.47 (0.38)	0.55 (0.34)
Midlatitude winter	0.686	0.86 (1.10)	0.39 (0.32)	0.46 (0.28)
Subarctic summer	1.653	1.20 (1.53)	0.69 (0.56)	0.84 (0.51)
Subarctic winter	0.328	0.94 (1.20)	0.39 (0.32)	0.28 (0.17)
U.S. Standard	1.125	1.07 (1.37)	0.51 (0.42)	0.58 (0.35)

i.e., in ignoring gas absorption, is usually $\lesssim$ 0.5 DC and is therefore undetectable with SeaWiFS. In Band 6 the error is usually $\sim$ 1 DC, but can reach $\sim$ 1.5 DC. This is principally due to the O_2 B absorption band which overlaps the long-wave shoulder of Band 6 (O_2 B band head is at $\sim$ 686 nm). Similar computations have been carried out for $\theta_0 = 0$ and 40°. These results of these for the U.S Standard atmosphere are presented in Table 8. These results suggest that the error imposed

Table 8: $\langle N_r(\lambda)F_0(\lambda)\rangle_{S_i} - \langle A_r(\lambda)F_0(\lambda)\rangle_{S_i}$ in % and in DC (in parenthesis) for the U.S. Standard atmosphere with nadir viewing.

θ_0	Band 6	Band 7	Band 8
0°	0.61 (1.22)	0.29 (0.38)	0.35 (0.34)
40°	0.61 (0.99)	0.27 (0.28)	0.28 (0.21)
60°	1.07 (1.37)	0.51 (0.42)	0.58 (0.35)

by ignoring the gas absorption (other than O_3) can be adequately corrected by subtracting $\sim$ 1.20, 0.36, and 0.30 DC from $\langle N_r(\lambda)F_0(\lambda)\rangle_{S_i}$ for Bands 6, 7, and 8, respectively.

4.B. Influence on $L_a + L_{ra}$

For the aerosol component ($L_a + L_{ra}$), we can obtain an upper limit to the gas absorption effect by assuming that the aerosol is confined in a layer near the surface and that the absorption is manifest in the two-way gas transmittance along the propagation path, i.e.,

$$L_a + L_{ra} \longrightarrow (L_a + L_{ra})T_g(\lambda, M),$$

where $T_g(\lambda, M)$ is the two-way transmittance of the atmosphere in the absence of Rayleigh scattering, aerosol scattering, and Ozone absorption. M is the two-way air mass. Equivalently, from Section 3B,

$$\langle \varepsilon(\lambda, \lambda_0)\rangle_{F_0S_i} \longrightarrow \langle T_g(\lambda, M)\varepsilon(\lambda, \lambda_0)\rangle_{F_0S_i} \approx \langle T_g(\lambda, M)\exp[c(\lambda_0 - \lambda)]\rangle_{F_0S_i}.$$

Table 9 compares $\langle \varepsilon(\lambda, 865)\rangle_{F_0S_i}$ with gas absorption with $\varepsilon(\lambda_i, 865)$ for $c = 0$ and 2×10^{-3} nm^{-1} in the LOWTRAN Tropical atmosphere with $M = 3$. Comparison with Table 4 (similar to

Table 9: Comparison between $\langle \varepsilon(\lambda, 865)\rangle_{F_0S_i}$ with gas absorption and $\varepsilon(\lambda_i, 865)$ for the LOWTRAN Tropical atmosphere with $M = 3$.

Band	c (nm^{-1})			
i	0		2×10^{-3}	
	$\langle \varepsilon(\lambda, 865)\rangle_{F_0S_i}$	$\varepsilon(\lambda_i, 865)$	$\langle \varepsilon(\lambda, 865)\rangle_{F_0S_i}$	$\varepsilon(\lambda_i, 865)$
1	1.0000	1.0000	2.4645	2.4744
2	1.0000	1.0000	2.3192	2.3257
3	0.9997	1.0000	2.1109	2.1170
4	0.9999	1.0000	2.0349	2.0340
5	0.9972	1.0000	1.8549	1.8589
6	0.9842	1.0000	1.4608	1.4770
7	0.9802	1.0000	1.1973	1.2214
8	0.9606	1.0000	0.9728	1.0000

Table 9 but without gas absorption and, therefore, independent of M) shows that the addition of gas absorption changes the character of $\langle \varepsilon(\lambda, 865)\rangle_{F_0S_i}$ in the red and the NIR, i.e., instead of

$\langle \varepsilon(\lambda, 865) \rangle_{F_0 S_i}$ being $\sim 1.3\%$ greater than unity for $c = 2 \times 10^{-3}$ nm^{-1}, gas absorption causes it to become $\sim 3\%$ less than unity. Such a variation will have a significant impact on atmospheric correction.

4.C . Influence on L_w

The assessment of gas absorption on $t(\lambda)L_w(\lambda)$ is particularly simple in the case of SeaWiFS. For Bands 1–5 there is essentially no effect, since they have small response for $\lambda \gtrsim 600$ nm, and for Bands 6–8 the effects is also negligible since most of their strong out-of-band response (and the source of most of their out-of-band radiance) is in regions of little gas absorption. Thus, gas absorption can be ignored for this term.

5. Atmospheric Correction

To effect atmospheric correction, i.e., to extract $\langle tL_w(\lambda) \rangle_{S_i}$, we need to compute

$$\langle tL_w(\lambda) \rangle_{S_i} = \langle L_t(\lambda) \rangle_{S_i} - \langle L_r(\lambda) \rangle_{S_i} - \langle L_a(\lambda) + L_{ra}(\lambda) \rangle_{S_i}.$$

We have already described the computation of $\langle L_r(\lambda) \rangle_{S_i}$, and $\langle L_t(\lambda) \rangle_{S_i}$ is the measured radiance, so the problem is to estimate $\langle L_a(\lambda) + L_{ra}(\lambda) \rangle_{S_i}$. We first examine estimation of this quantity in the approximation that $C\left(\theta_v, \phi_v, \theta_0, \phi_0, L_a^{ss}(\lambda), \lambda\right)$ is independent of $L_a^{ss}(\lambda)$ and λ. This is in essence the single scattering approximation, and much of the analysis can be carried out analytically. It will enable a quantitative estimate of the seriousness of the out-of-band response perturbation on atmospheric correction. Then we follow with a technique for including the out-of-band effects in the full multiple scattering algorithm.

5.A. $C\left(\theta_v, \phi_v, \theta_0, \phi_0, L_a^{ss}(\lambda), \lambda\right)$ independent of $L_a^{ss}(\lambda)$ and λ

Utilizing Eq. (7), and referring to Section 3B on the band-averaged $L_a(\lambda) + L_{ra}(\lambda)$, we see that in this approximation,

$$\langle L_a(\lambda) + L_{ra}(\lambda) \rangle_{S_i} = \frac{\langle F_0(\lambda) \rangle_{S_i}}{\langle F_0(\lambda) \rangle_{S_8}} \varepsilon(i, 8) \langle L_a(\lambda) + L_{ra}(\lambda) \rangle_{S_8},$$

where $\varepsilon(i,8)$ is given by

$$\varepsilon(i,8) \equiv \frac{\langle \varepsilon(\lambda,865)\rangle_{F_0 S_i}}{\langle \varepsilon(\lambda,865)\rangle_{F_0 S_8}}.$$

For the open ocean, $\langle tL_w(\lambda)\rangle_{S_i} \approx 0$, for $i = 7$ and 8 (Table 5), so $\varepsilon(7,8)$ and $\varepsilon(8,8)$ can be estimated at each pixel. The key to the correction algorithm is to be able to extrapolate $\varepsilon(7,8)$ to $\varepsilon(i,8)$. A logical way of addressing this is to assume, by analogy to Eq. (16), that

$$\varepsilon(i,8) = \exp[c'(865 - \lambda_i)], \tag{19}$$

where c' is determined from the SeaWiFS-measured value of $\varepsilon(7,8)$ with $\varepsilon(8,8) = 1$. However, since there is considerable out-of-band contamination in the NIR on $\langle \varepsilon(\lambda,865)\rangle_{F_0 S_8}$, $\varepsilon(i,8)$ will not follow Eq. (19) as well as $\varepsilon(\lambda_i,865)$ follows Eq. (16), and the extrapolation will be inaccurate. Consider the problem of estimating the band-averaged water-leaving radiance in SeaWiFS Band 2 (443 nm) for a case in which $\varepsilon(\lambda_i,865)$ follows Eq. (16) exactly. For the specific examples in Table 9, we can compute both the exact and the extrapolated values of $\varepsilon(i,8)$. These are provided in Table 10. If

Table 10: Comparison between the exact and extrapolated values of $\varepsilon(i,8)$ for the LOWTRAN Tropical atmosphere with $M = 3$.

Band	c (nm^{-1})			
i	0		2×10^{-3}	
	Exact	Extrapolated	Exact	Extrapolated
1	1.041	1.096	2.533	2.562
2	1.041	1.089	2.384	2.402
3	1.041	1.079	2.170	2.179
4	1.041	1.074	2.092	2.090
5	1.038	1.064	1.907	1.904
6	1.025	1.040	1.502	1.500
7	1.020	1.020	1.231	1.231
8	1.000	1.000	1.000	1.000

we used the extrapolated values of $\varepsilon(2,8)$ given in Table 10, the extrapolated values would be in error by ~ 1 and 5% for $c = 2\times10^{-3}$ and $c = 0$ nm^{-1}, respectively. Are these serious errors? Noting that an error in $\langle L_a(\lambda) + L_{ra}(\lambda)\rangle_{S_i}$ will lead to an identical error in $\langle t(\theta_v,\lambda)L_w(\lambda)\rangle_{S_i}$, it is easy to show that an error $\Delta\varepsilon(i,8)$ in $\varepsilon(i,8)$ will result in an error $\Delta\langle t(\theta_v,\lambda)L_w(\lambda)\rangle_{S_i}$ in $\langle t(\theta_v,\lambda)L_w(\lambda)\rangle_{S_i}$ given by

$$\frac{\Delta\varepsilon(i,8)}{\varepsilon(i,8)} = \frac{\Delta\langle t(\theta_v,\lambda)L_w(\lambda)\rangle_{S_i}}{\langle L_a(\lambda) + L_{ra}(\lambda)\rangle_{S_i}} = \frac{\langle t(\theta_v,\lambda)\Delta L_w(\lambda)\rangle_{S_i}}{\langle L_w(\lambda)\rangle_{S_i}} \frac{\langle L_w(\lambda)\rangle_{S_i}}{\langle L_a(\lambda) + L_{ra}(\lambda)\rangle_{S_i}}.$$

To achieve a desired fractional error in $\langle L_w(\lambda)\rangle_{S_i} \leq p$,

$$\frac{\Delta\varepsilon(i,8)}{\varepsilon(i,8)} \leq t(\theta_v,i)\frac{\langle L_w(\lambda)\rangle_{S_i}}{\langle L_a(\lambda)+L_{ra}(\lambda)\rangle_{S_i}}\,p,$$

where $t(\theta_v,i)$ is given by Eq. (18). We can estimate the effect of $\Delta\varepsilon(i,8)$ by using the simulations presented in Ref. 2, in which the reflectance ρ, defined to be $\pi L/F_0\cos\theta_0$, was used in place of the

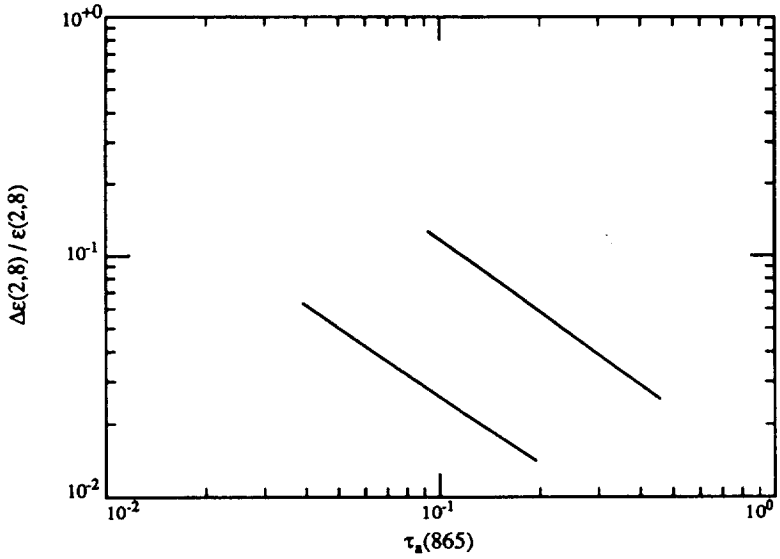

Figure 5. Maximum value of $\Delta\varepsilon(2,8)/\varepsilon(2,8)$ as a function of τ_a required to provide maintain an error in the water-leaving radiance in Band 2 of less than 5% as described in the text. The lower curve is for the T70 aerosol model and the upper curve for M98.

radiance. We note that

$$\langle\rho(\lambda)\rangle_{F_0S_i} = \frac{\pi\langle L(\lambda)\rangle_{S_i}}{\langle F_0(\lambda)\rangle_{S_i}\cos\theta_0},$$

so

$$\frac{\Delta\varepsilon(i,8)}{\varepsilon(i,8)} \leq t(\theta_v,i)\frac{\langle\rho_w(\lambda)\rangle_{F_0S_i}}{\langle\rho_a(\lambda)+\rho_{ra}(\lambda)\rangle_{F_0S_i}}\,p = t(\theta_v,i)t(\theta_0,i)\frac{\langle[\rho_w(\lambda)]_N\rangle_{F_0S_i}}{\langle\rho_a(\lambda)+\rho_{ra}(\lambda)\rangle_{F_0S_i}}\,p.$$

Now, for clear water, e.g., the Sargasso Sea in summer, $\langle[\rho_w(\lambda)]_N\rangle_{F_0S_2} \approx 0.038$, and for the simulations in Ref. 2, $\theta_0 = 60°$ and $\theta_v = 45°$, so $M = 3.41$. Eq. (2) gives $t(\theta_v,2)t(\theta_0,2) \approx 0.66$. Then, for a 5% error ($p = 0.05$) in Band 2,

$$\frac{\Delta\varepsilon(2,8)}{\varepsilon(2,8)} \leq \frac{0.00125}{\langle\rho_a(\lambda)+\rho_{ra}(\lambda)\rangle_{S_2}}.$$

Gordon and Wang's[2] Figure 2 can be used to provide $\langle \rho_a(\lambda) + \rho_{ra}(\lambda) \rangle_{S_2}$, since band averaging of this has little effect in the short-wave bands. This quantity can be related to the aerosol optical thickness, $\tau_a(\lambda)$, at 865 nm. [Note, one also needs to know that $\tau_a(443)/\tau_a(865) = 1.089$ and 2.558 for the M98 and T70 models, respectively.] The result of this exercise is presented in Figure 5. For a given $\tau_a(865)$, the required $\Delta\varepsilon(2,8)/\varepsilon(2,8)$ must be four times smaller for the T70 model compared to the M98, the two extreme models in Ref. 2. The T70 model has $c \approx 1.8 \times 10^{-3}$ nm^{-1}, so $\Delta\varepsilon(2,8)/\varepsilon(2,8) \approx +0.01$ (Table 10) and retrieving $\langle L_w(\lambda) \rangle_{S_2}$ with an error $< 5\%$ would be impossible for $\tau_a(865) \gtrsim 0.3$ (Figure 5). In contrast, the M98 model has $c \approx 0$ so $\Delta\varepsilon(2,8)/\varepsilon(2,8) \approx +0.05$, and insuring a $< 5\%$ error in $\langle L_w(\lambda) \rangle_{S_2}$ would require $\tau_a(865) \lesssim 0.2$.

It is possible to overcome these limitations on the aerosol optical thickness by recognizing that the error in the extrapolated value of $\varepsilon(2,8)$ is entirely due to the difference between $\varepsilon(\lambda_i, 865)$ and $\langle \varepsilon(\lambda, 865) \rangle_{F_0 S_i}$ for $i = 7$ and 8 (Table 9), i.e., the out-of-band response in Bands 7 and 8. That is, if we know the approximate value of c, e.g., c', it should be possible to assess the out-of-band influence on $\varepsilon(7,8)$, the basis for the extrapolation procedure. Unfortunately, the error in extrapolation shows a significant dependence on the water vapor content of the atmosphere. This is demonstrated in Table 11 which provides the error $\Delta\varepsilon(2,8)/\varepsilon(2,8)$ for $c = 0$, $M = 3$ and the six LOWTRAN atmospheric models. Since the water vapor concentration will generally be

Table 11: Error (%) in the extrapolated value of $\varepsilon(2,8)$ for $c = 0$ and $M = 3$ as a function of the water vapor concentration (w) in the LOWTRAN atmospheric models.

LOWTRAN model	w g/cm^2	$\Delta\varepsilon(2,8)/\varepsilon(2,8)$
Tropical	3.332	4.60
Midlatitude summer	2.356	3.83
Midlatitude winter	0.686	2.02
Subarctic summer	1.653	3.16
Subarctic winter	0.328	1.43
U.S. Standard	1.125	2.59

unknown, we also need to understand the influence of choosing an incorrect concentration on which to improve the extrapolation.

It is relatively simple to define a procedure for improving the extrapolation of $\varepsilon(7,8)$ to $\varepsilon(i,8)$. Let

$$f_i(c,M,w) \equiv \frac{\langle \varepsilon(\lambda,865)\rangle_{F_0 S_i}}{\varepsilon(\lambda_i,865)},$$

where w is the total columnar water vapor concentration, and for a given viewing geometry and model, c is defined by Eq. (16). Then, $\varepsilon(i,8)$ is given by

$$\varepsilon(i,8) = \frac{f_i(c,M,w)}{f_8(c,M,w)}\varepsilon(\lambda_i,865). \tag{20}$$

Assuming that the functions $f_i(c,M,w)$ are known, $\varepsilon(i,8)$ can be estimated in the following manner: (1) the initial value of $\varepsilon(7,8)$, i.e., uncorrected for out-of-band effects on $\langle L_a + L_{ra}\rangle_{F_0 S_i}$, is used in Eq. (19) to estimate c'; (2) this value of c' is used in the place of c to estimate $f_i(c,M,w)$; (3) $f_i(c',M,w)$ and the initial value of $\varepsilon(7,8)$ are used in Eq. (20) to estimate $\varepsilon(\lambda_7,865)$, which in turn is used in Eq. (16) to provide a better estimate of c; (4) this estimate of c is used in Eq. (16) to obtain $\varepsilon(\lambda_i,865)$; and (5) Eq. (20) is used to obtain the final estimate of $\varepsilon(i,8)$. After step (4), new values of $f_i(c,M,w)$ could be deduced using the improved estimate of c, if necessary.

To operate this procedure, we need the functions $f_i(c,M,w)$. Through multiple least-squares analysis, we have found that they can be reasonably well represented by the equation

$$\begin{aligned} f_i(c,M,w) = {} & (a_{01} + a_{02}M) + (a_{03} + a_{04}M)c \\ & + \left[(a_{11} + a_{12}M) + (a_{13} + a_{14}M)c\right]w \\ & + \left[(a_{21} + a_{22}M) + (a_{23} + a_{24}M)c\right]w^2, \end{aligned} \tag{21}$$

where the coefficients a_{nm} for SeaWiFS Bands 6, 7, and 8, are provided in Table 12. Figure 6 compares the fitted and the true values of $f_i(c,M,w)$ for SeaWiFS Band 8, and suggests that given M and the aerosol model (c), $f_8(c,M,w)$ can be estimated with an error of $\lesssim 0.1-0.2\%$. The fits to Eq. (21) for SeaWiFS Bands 6 and 7 are much better than that in Figure 6, and for SeaWiFS Bands 1–5 we can assume $f_i(c,M,w) = 1$ (Table 9).

We have examined the efficacy of this procedure by considering the case $M = 3$, and a LOWTRAN Tropical atmosphere. First we assumed that the water vapor concentration is known ($w = 3.322$ g/cm^2), and then examined the effect of an error in w. Thus, initially only the value of c was unknown. The above procedure provided $\varepsilon(2,8) = 1.045$ compared to the correct value of 1.041, a +0.4% error. If the water vapor concentration were also unknown, the error would be

larger. For a concentration 1.318 g/cm^2 (midway between the lowest and highest LOWTRAN concentrations) the procedure yielded $\varepsilon(2,8) = 1.063$ or an error of $\sim +2\%$. Note that even without an accurate value of w, the procedure reduced the error in $\varepsilon(2,8)$ by more than a factor of 2,

Table 12: Coefficients a_{nm} in Eq. (21) for SeaWiFS bands 6, 7, and 8, for c in nm^{-1} and w in gm/cm^2. Notation ± 2 stands for $10^{\pm 2}$, etc.

Coefficient	a_{nm}		
	Band 6	Band 7	Band 8
a_{01}	+9.986 −1	+9.983 −1	+9.958 −1
a_{02}	−7.046 −4	−8.214 −4	−1.561 −3
a_{03}	+2.459 +0	−4.094 −1	+6.442 +0
a_{04}	+2.545 −3	+3.732 −2	−1.894 −2
a_{11}	−1.644 −3	−3.537 −3	−6.337 −3
a_{12}	−1.188 −3	−1.303 −3	−2.679 −3
a_{13}	−1.015 −2	+1.767 −1	−1.037 −2
a_{14}	−8.021 −3	+8.578 −3	−3.583 −2
a_{21}	+1.378 −4	+3.686 −4	+6.157 −4
a_{22}	+1.079 −4	+1.534 −4	+3.080 −4
a_{23}	+1.233 −3	−2.471 −2	−2.428 −3
a_{24}	+4.105 −4	−2.145 −3	+3.628 −3

i.e., from 1.096 to 1.063 compared to the correct 1.041. This would extend the $\tau_a(865)$ limit for a 5% error in $\langle [\rho_w(\lambda)]_N \rangle_{F_0 S_2}$ from ~ 0.3 to ~ 0.5 (Figure 4). However, it is clear that because of the significant out-of-band responses of SeaWiFS Bands 7 and 8, the variation of the water vapor content of the atmosphere limits the accuracy of atmospheric correction at larger values of $\tau_a(865)$.

The procedure outlined in this section can be directly incorporated into the simple correction algorithm described by Wang and Gordon[12] that ignored multiple scattering.

5.B. Inclusion of multiple scattering

Switching from radiance (L) to reflectance (ρ), in the presence of multiple scattering $\rho_a^{ss}(\lambda)$ is replaced by

$$\rho_a(\lambda) + \rho_{ra}(\lambda) = C\Big(\theta_v, \phi_v, \theta_0, \phi_0, \rho_a^{ss}(\lambda), \lambda\Big)\, \rho_a^{ss}(\lambda) \tag{22}$$

where C is a weak function of $\rho_a^{**}(\lambda)$ and λ. In the band-averaged case, we must deal with $\langle \rho_a(\lambda) + \rho_{ra}(\lambda) \rangle_{F_0 S_i}$. Because of the weak dependence of C on $\rho_a^{**}(\lambda)$ and λ, we can ignore the out-of-band effects on C and approximate $\langle \rho_a(\lambda) + \rho_{ra}(\lambda) \rangle_{F_0 S_i}$ by

$$\begin{aligned} \langle \rho_a(\lambda) + \rho_{ra}(\lambda) \rangle_{F_0 S_i} &= C\Big(\theta_v, \phi_v, \theta_0, \phi_0, \rho_a^{**}(\lambda_i), \lambda_i\Big) \langle \rho_a^{**}(\lambda) \rangle_{F_0 S_i} \\ &= C\Big(\theta_v, \phi_v, \theta_0, \phi_0, \rho_a^{**}(\lambda_i), \lambda_i\Big) \left[\frac{\langle \varepsilon(\lambda, 865) \rangle_{F_0 S_i}}{\varepsilon(\lambda_i, 865)} \rho_a^{**}(\lambda_i) \right], \\ &= C\Big(\theta_v, \phi_v, \theta_0, \phi_0, \rho_a^{**}(\lambda_i), \lambda_i\Big) f_i(c, M, w) \rho_a^{**}(\lambda_i), \end{aligned} \tag{23}$$

i.e., in the band-averaged case $\rho_a^{**}(\lambda)$ outside of the argument of C in Eq. (22) is replaced by $f_i(c, M, w)\rho_a^{**}(\lambda_i)$, in Eq. (23). Since the influence of multiple scattering on the algorithm is

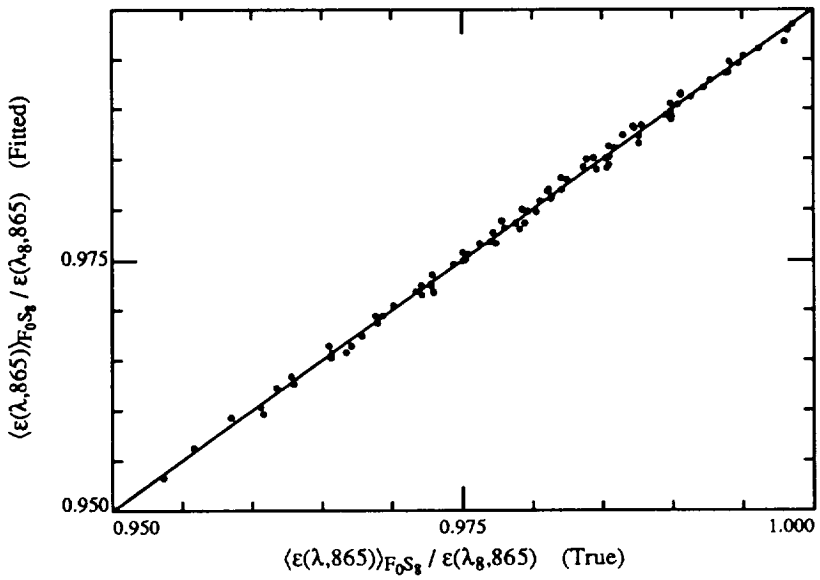

Figure 6. Comparison between the true values of $\langle \varepsilon(\lambda, 865) \rangle_{F_0 S_g} / \varepsilon(\lambda_g, 865)$ with those computed using Eq. (21) and Table 12.

contained in the dependence of C on $\rho_a^{**}(\lambda)$ and λ, retaining the dependence of C on $\rho_a^{**}(\lambda_i)$ and λ_i in Eq. (23) will retain the multiple scattering effects in the algorithm. For a given aerosol model (known c), $f_i(c, M, w)$ can be estimated given the water vapor content and the viewing geometry using Eq. (21). In the Gordon and Wang[2] multiple scattering algorithm, $\rho_a(\lambda_i) + \rho_{ra}(\lambda_i)$ determined from $\rho_t(\lambda_i) - \rho_r(\lambda_i)$ for $i = 7$ and 8 is used in Eq. (22) to estimate $\rho_a^{**}(\lambda_i)$, which in turn is used to estimate $\rho_a(\lambda_i) + \rho_{ra}(\lambda_i)$ for $i = 1$ to 6. When the out-of-band response is included, $\langle \rho_a(\lambda) + \rho_{ra}(\lambda) \rangle_{F_0 S_i}$ for $i = 7$ and 8 is used in Eq. (23) to estimate $\rho_a^{**}(\lambda_i)$, which is used

in a similar manner to estimate $\langle \rho_a(\lambda) + \rho_{ra}(\lambda) \rangle_{F_0 S_i}$ for $i = 1$ to 6. This approach for including the out-of-band effects is satisfying because the implementation strategy for utilizing Eq. (22) — lookup tables relating $\rho_a(\lambda_i) + \rho_{ra}(\lambda_i)$ to $\rho_a^{**}(\lambda_i)$ for all sun-viewing geometries and nominal band centers i based on solutions to the radiative transfer equation — can be applied to Eq. (23) using the *same* lookup tables. One need only recognize that when $\langle \rho_a(\lambda) + \rho_{ra}(\lambda) \rangle_{F_0 S_i}$ is entered on the left-hand-side of Eq. (23), the result is $f_i(c, M, w)\rho_a^{**}(\lambda_i)$ rather than just $\rho_a^{**}(\lambda_i)$. We envisage implementation of this out-of-band response modification to the multiple scattering atmospheric correction algorithm will be based on a lookup table relating the parameter c in Eq. (16) to the sun-viewing geometry for each model.

6. Concluding remarks

A methodology for delineating the influence of finite spectral band widths and significant out-of-band response on ocean color imagery was described and applied to SeaWiFS. The basis of the method is the application of the sensor's spectral response functions to the individual components of the TOA radiance. The importance of the examination of the individual components is that it provides an avenue for estimating the impact on the entire ocean color system — sensor plus algorithms.

As might be expected, the most significant effects of finite band widths and out-of-band response occurs for components with a very strong spectral variation, e.g., $L_r(\lambda)$ and $L_w(\lambda)$. In the case of SeaWiFS Band 8 (865 nm), it is shown that the significant out-of-band response in the blue requires that an optical thickness of 0.0169 $[\langle \tau_r(\lambda) \rangle_{F_0 S_8}]$ rather than 0.0155 $[\tau_r(865)]$ be used to predict $\langle L_r(\lambda) \rangle_{S_8}$. In fact, as much as 9% of $\langle L_r(\lambda) \rangle_{S_8}$ is due to $L_r(\lambda)$ for $\lambda < 600$ nm. For the water-leaving radiance, the error in replacing $\langle L_w(\lambda) \rangle_{S_i}$ by its narrow-band counterpart, $L_w(\lambda_i)$, is of the order of a few percent in the blue-green bands. This implies that verification that the SeaWiFS system — sensor plus algorithms — meets the goal of providing the water-leaving radiance in the blue in clear ocean water to within 5% will require measurements of $L_w(\lambda)$ through out the visible rather than just in a narrow (10–20 nm) spectral band around λ_2. In the NIR, a large fraction (Table 5) of $\langle L_w(\lambda) \rangle_{S_i}$ is the result of the out-of-band response of the sensor; however, $\langle L_w(\lambda) \rangle_{S_i}$ is still usually $\lesssim 1$ DC, so these bands can still be used for atmospheric correction.

Gaseous absorption (other than Ozone) is mostly confined to the red and NIR spectral regions (Figures 3 and 4). Thus, we expect its influence to be strongest for $\lambda \gtrsim 600$ nm, and strongest for the components of $L_t(\lambda)$ that have a weak spectral dependence. In fact, there is little or no influence of gaseous absorption on $\langle L_w(\lambda)\rangle_{S_i}$, and for $\langle L_r(\lambda)\rangle_{S_i}$ the influence is only ≈ 1 DC for Band 6 and < 1 DC for Bands 7 and 8. In contrast, gaseous absorption is important for the aerosol component. It can cause a significant reduction (a few percent) in the aerosol component in Bands 6, 7, and 8.

By assuming that the aerosols reside in a thin layer near the surface (the marine boundary layer), it is found that atmospheric correction of SeaWiFS can be degraded by the influence of water vapor absorption in the shoulders of Bands 7 and 8. This causes an apparent spectral variation of $L_a + L_{ra}$ between these two bands that would be uncharacteristic of the aerosol present, leading to an error in atmospheric correction. This effect is dependent on the water vapor content of the atmosphere. At typical water vapor concentrations, the error is larger for aerosols with weak spectral variation in reflectance than for those displaying a strong spectral variation. If the content is known, a simple procedure can be used to reduce the degradation of the atmospheric correction in both single- and multiple-scattering approaches. Uncertainty in the water vapor content will limit the accuracy of the SeaWiFS correction algorithm.

Appendix

The nominal radiometric characteristics of SeaWiFS[1] are presented in Table 13. In the table, λ represents the spectral pass band of each of the instrument's spectral bands. The detailed spectral response functions that were used in the text for each band are presented in Barnes et al.[7] L_{Sat} is the saturation radiance at the lower ocean-viewing sensitivity. There are three other radiometric sensitivities: two for stability monitoring by viewing sun light reflected from an internal diffuser

Table 13: Nominal SeaWiFS instrument parameters.

Band	λ nm	L_{Sat} mW/cm^2 μm Sr
1	402–422	13.63
2	433–453	13.25
3	480–500	10.50
4	500–520	9.08
5	545–565	7.44
6	660–680	4.20
7	745–785	3.00
8	845–885	2.13

(short-term) or from the moon (long-term); and one for ocean viewing at large solar zenith angles. The saturation radiance for the second (higher) ocean-viewing sensitivity is $\sim L_{Sat}/2$, i.e., it has twice the radiometric sensitivity of the lower. The radiance data are 10-bit digitized on-board the space craft, so 1 digital count (DC) of radiance is approximately $L_{Sat}/1024$. When DC's are mentioned in the text, unless otherwise noted, the reference is to those corresponding to the *lower* ocean-viewing sensitivity (Table 13). Signal-to-noise ratios are generally of the order of 500 for input radiances at $\sim \frac{1}{2}$ to $\frac{3}{4}$ of L_{Sat}, so the sensor noise will be of the order of 1 DC for all bands.

References

[1] S. B. Hooker, W. E. Esaias, G. C. Feldman, W. W. Gregg and C. R. McClain, *SeaWiFS Technical Report Series: Volume 1, An Overview of SeaWiFS and Ocean Color* (NASA, Greenbelt, MD, Technical Memorandum 104566, July 1992).

[2] H. R. Gordon and M. Wang, "Retrieval of water-leaving radiance and aerosol optical thickness over the oceans with SeaWiFS: A preliminary algorithm," Applied Optics **33**, 443–452 (1994).

[3] P. Y. Deschamps, M. Herman and D. Tanre, "Modeling of the atmospheric effects and its application to the remote sensing of ocean color," Applied Optics **22**, 3751–3758 (1983).

[4] H. R. Gordon, D. K. Clark, J. L. Mueller and W. A. Hovis, "Phytoplankton pigments derived from the Nimbus–7 CZCS: initial comparisons with surface measurements," Science **210**, 63–66 (1980).

[5] H. R. Gordon, D. K. Clark, J. W. Brown, O. B. Brown, R. H. Evans and W. W. Broenkow, "Phytoplankton pigment concentrations in the Middle Atlantic Bight: comparison between ship determinations and Coastal Zone Color Scanner estimates," Applied Optics **22**, 20–36 (1983).

[6] H. R. Gordon, J. W. Brown and R. H. Evans, "Exact Rayleigh Scattering Calculations for use with the Nimbus-7 Coastal Zone Color Scanner," Applied Optics **27**, 862–871 (1988).

[7] R. A. Barnes, A. W. Holmes, W. L. Barnes, W. E. Esaias, C. R. McClain and T. Svitek, *SeaWiFS Technical Report Series: Volume 23, SeaWiFS Prelaunch Radiometric Calibration and Spectral Characterization* (NASA, Greenbelt, MD, Technical Memorandum 104566, October 1994).

[8] J. E. Hansen and L. D. Travis, "Light Scattering in Planetary Atmospheres," Space Science Reviews **16**, 527–610 (1974).

[9] J. -M. André and A. Morel, "Simulated Effects of Barometric Pressure and Ozone Content Upon the Estimate of Marine Phytoplankton From Space," Jour. Geophys. Res. **94C**, 1029–1037 (1989).

[10] M. Nicolet, "The solar spectral irradiance and its action in the atmospheric photodissociation processes," Planet. Space Sci. **29**, 951–974 (1981).

[11] H. Neckel and D. Labs, "The Solar Radiation Between 3300 and 12500 Å," Solar Physics **90**, 205–258 (1984).

[12] M. Wang and H. R. Gordon, "A Simple, Moderately Accurate, Atmospheric Correction Algorithm for SeaWiFS," Remote Sensing of Environment **50**, 321–239 (1994).

[13] E. P. Shettle and R. W. Fenn, *Models for the Aerosols of the Lower Atmosphere and the Effects of Humidity Variations on Their Optical Properties* (Air Force Geophysics Laboratory, Hanscomb AFB, MA 01731, AFGL–TR–79-0214, 1979).

[14] F. X. Kenizys, E. P. Shettle, W. O. Gallery, J.H.Chetwynd, L. W. Abreu, J. E. A. Selby, S. A. Clough and R. W. Fenn, *Atmospheric Transmittance/Radiance: The LOWTRAN 6 Model* (Air Force Geophysics Laboratory, Hanscomb AFB, MA 01731, AFGL–TR–83–0187, 1983) NTIS AD A137796.

[15] H. R. Gordon, O. B. Brown, R. H. Evans, J. W. Brown, R. C. Smith, K. S. Baker and D. K. Clark, "A Semi-Analytic Radiance Model of Ocean Color," Jour. Geophys. Res. **93D**, 10909–10924 (1988).

[16] H. R. Gordon and D. K. Clark, "Clear water radiances for atmospheric correction of coastal zone color scanner imagery," Applied Optics **20**, 4175–4180 (1981).

[17] D. K. Clark, "Phytoplankton Algorithms for the Nimbus-7 CZCS," in *Oceanography from Space*, edited by J. R. F. Gower (Plenum Press, New York, NY, 1981) p. 227–238.

[18] H. R. Gordon and K. Ding, "Self-Shading of In-Water Optical Instruments," Limnology and Oceanography **37**, 491–500 (1992).

[19] F. X. Kneizys, E. P. Shettle, L. W. Abreu, J. H. Chetwynd, G. P. Anderson, W. O. Gallery, J. E. A. Selby and S. A. Clough, *Users Guide to LOWTRAN 7* (Air Force Geophysics Laboratory, AFGL-TR-88-0177, 1988).

[20] K. Ding and H. R. Gordon, "Analysis of the influence of O_2 *A* band absorption on atmospheric correction of ocean color imagery," Applied Optics **34**, 2068–2080 (1995).